Environmental Coupling in a Quantum Dot as a Resource for Quantum Optics and Spin Control

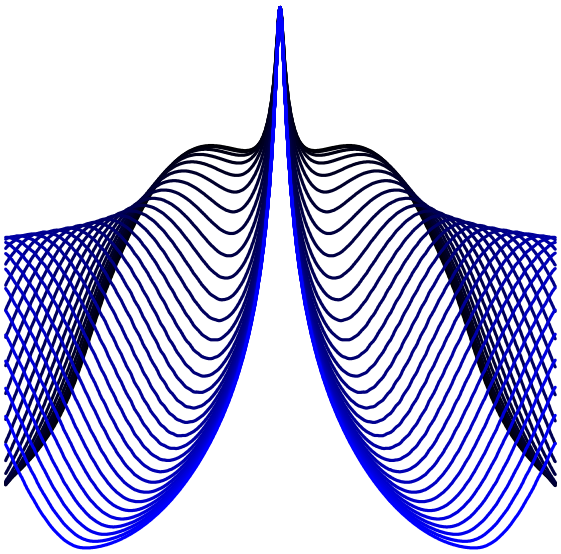

Jack Hansom

Department of Physics

University of Cambridge

This dissertation is submitted for the degree of

Doctor of Philosophy

Churchill College

June 2015

Declaration

This dissertation is the result of my own work and includes nothing which is the outcome of work done in collaboration except where specifically indicated in the text.

It is not substantially the same as any that I have submitted, or, is being concurrently submitted for a degree or diploma or other qualification at the University of Cambridge or any other University or similar institution except as declared in the Preface and specified in the text. I further state that no substantial part of my dissertation has already been submitted, or, is being concurrently submitted for any such degree, diploma or other qualification at the University of Cambridge or any other University of similar institution except as declared in the Preface and specified in the text.

This dissertation does not exceed the word limit of 60000 words.

Jack Hansom
June 2015

This thesis is dedicated to my parents.

Acknowledgements

A bit more than four years ago, I was first shown around the lab. Clemens showed me his most recent exciton Rabi oscillations, Tina tried to explain the Jahn-Teller effect (which mostly went over my head), and Josh showed me images of bow-tie antennae. I was impressed with their enthusiasm in showing yet another prospective student around their respective setups. I knew from then on that this group would provide an enjoyable and cooperative environment for my PhD.

First, I'd like to thank Mete Atatüre for taking me on, and for his continued guidance and support. His enthusiasm and excitement are an essential part of what makes the group both dynamic and fun. His occasional lectures on the art of milk frothing also provide a useful distraction.

I've been fortunate to work with an extremely talented bunch of people within the QD team, which has made for an enjoyable and intellectually challenging environment. Following the theme of the thesis, this environment has been a tremendous resource in terms of technical expertise and enlightening discussions, and all the members of the QD team deserve acknowledgement: Alex, Carsten, Claire, Clemens, Lukas, Megan, Paul and Rob. I would also like to thank Jake Taylor, whose insightful comments and suggestions have contributed greatly to the outcome of this thesis.

The group has grown quite a bit since I first joined, and every new arrival has brought with them new insight and energy to the group. As well as contributing to the atmosphere of collaborative enthusiasm in the group, I'd like to thank the rest of the AMOP-MESS team for helpful discussions and technical assistance from which this thesis has benefited significantly: Ben, Carmen, Christian, David-Dominik, Dhiren, Helena, Jan, Josh, Lina, Tina, and Yury.

I would like to thank the administrative staff, and particularly Pam, whose efficiency and organisation will never cease to amaze.

My writing is sometimes in need of a good deconvolution, and I'm grateful to Rob, Claire, Mete and my father for proof-reading my thesis and giving me their suggestions and corrections.

I would also like to thank Prof. Jonathan Finley and Dr. Andrew Ferguson who agreed to examine this thesis and provided many insightful questions and comments during the viva.

Beyond the physics, I will always have fond memories of going to conferences and other outings with the group: from teaching kids and (not-so-) grown-ups about soap computers at the Green Man festival to hiking among the redwoods of California.
Finally, I would like to thank my friends and family for their love and support. In particular, I'd like to thank LeAnn for her continued support throughout my PhD, even with an ocean between us.

Abstract

A single spin confined to a semiconductor quantum dot is a system of significant interest for quantum information science, as a potential optically-addressable qubit. In many respects, a quantum dot behaves like a single atom with high quality single photon emission. By controlling the light-matter coupling in such a system, it is possible to generate highly non-classical states of light and coherently control a single spin confined to the quantum dot.

A departure from the ideal atomic picture appears once we consider the mesoscopic environment with which the quantum dot interacts. Charge fluctuations in the surroundings of the quantum dot affect the photon emission frequency leading to inhomogeneous broadening. Further broadening of the emission is caused by coupling to phonon modes of the host semiconductor material. Finally, coupling between the spin of a confined electron and a large bath of nuclear spins residing in the quantum dot leads to fast dephasing of the electron spin. All of these effects are typically considered detrimental to the potential use of quantum dots for quantum technologies. In this thesis, we develop the environmental coupling of a negatively charged quantum dot as a resource for quantum optics and spin control.

First, the phonon-assisted fluorescence is shown to be a useful independent channel for feedback stabilisation of the quantum dot emission frequency, without requiring a measurement of the indistinguishable zero-phonon line. With stabilisation, the corresponding frequency broadening is drastically improved, and the sub-Hz frequency fluctuations are no longer resolved.

Next, we show low-power resonance fluorescence emission spectra of the negatively charged trion transition. In the low power regime of resonance fluorescence, the excited state is not populated and most of the emission is coherent. In addition to elastic Rayleigh scattering, we observe coherent Raman sidebands, linked to an effective magnetic field created by the hyperfine interaction, the Overhauser field. This fluctuating effective field lifts the electron spin degeneracy in the absence of a magnetic field, and dictates the optical selection rules of the trion system. These spectra therefore allow for a measurement of the time-averaged distributions of in-plane and out-of-plane Overhauser field components.

In the final part of the thesis, we use this hyperfine-generated Λ-scheme to optically create electron spin superpositions through two-colour excitation and coherent population trapping. We then show that rapid shifts in the relative phase of the lasers lead to initialisation of the electron spin into a rotated dark state.

Table of contents

Chapter 1

Introduction

In this introduction, we aim to clarify the terms used in the title of the thesis. First the system under study, consisting of self-assembled semiconductor quantum dots (QD), is introduced. We then briefly recap the state of the art of QD research against the background of quantum information science. Finally, we introduce the environment mentioned in the title, and its problematic aspects in terms of QD-based quantum optics and spin control.

1.1 Quantum Dots as Artificial Atoms

1.1.1 Quantum Dot Growth

Progress in the field of quantum information science with QDs has been made possible by the developments in heteroepitaxial growth techniques. The QDs studied here were grown by molecular beam epitaxy (MBE) in the Stranski-Krastanov (SK) growth mode [1]. MBE allows for layer-by-layer crystal growth of high-quality semiconductor materials controlled on the monolayer scale allowing abrupt changes in materials. Complex layered heterostructures can be grown in this way, which has been crucial to the development of high-quality optically-active QDs. For our samples, InAs is grown on top of a GaAs substrate. These two materials have similar crystal structure but a lattice constant mismatch of $\approx 7\%$. At first, the InAs layer adapts to the substrate lattice and strain accumulates. After a critical layer thickness, the strain relaxes and islands of InAs form spontaneously.
The random nature of the SK growth process means that QDs are formed at random locations and have randomly distributed sizes and morphologies. This isn't critical for the single-QD studies discussed in this thesis as we can afford to spend some time looking for the right QD. However, this is a major challenge for scaling QD-based technologies and has motivated research into the deterministic positioning of optically-active QDs [2].

By carefully choosing appropriate growth conditions, islands of dimensions comparable to the exciton Bohr radius in the bulk material can be grown. The InAs direct band gap (0.43 eV) is much smaller than that of GaAs (1.52 eV), which leads to a creation of a confining potential for electrons and holes within the QD. This 3 dimensional confinement leads to a discrete energy spectrum of excitons confined to the QD.
The exact energy spectrum depends on the QD size and composition. This can be tuned by varying the growth parameters, or alloying induced by post-growth annealing. Specifically, the height of the dot can be tuned through partial capping of the QD layer with GaAs and subsequent annealing. The typical QDs grown in this fashion are lens shaped with a diameter of order 10 nm and a height of around 3 nm, and the confinement is therefore strongest in the z-direction. This technique blue-shifts the energy spectrum to ≈ 1.3 eV such that common Si detectors can be used to study these QDs.

1.1.2 From Confined Exciton to Light

We have established that charge carriers, i.e. conduction band electrons and valence band holes, can be trapped by the confining potential created by the QD. Light emission is then linked to the recombination of excitons, bound electron-hole pairs, confined to the QD. This process is schematically depicted in Fig. 1.1. Light emission from the QD can be induced by optical creation of excitons within the host matrix, with above bandgap excitation. The excitons rapidly decay to the lowest available energy state, i.e. into the QD. The subsequent recombination on a timescale of hundreds of ps leads to the emission of a photon. The entire process is called photoluminescence. An example spectrum obtained via this process is shown in panel B of Fig. 1.1. Discrete peaks can be seen in the spectrum, confirming the atom-like nature of the QD. The peaks which are not labeled are linked to emission from other QDs within the collected area. For the three most intense peaks, generated by the same QD, each peak is associated to a different charge complex within the QD. In addition to electron-hole pairs, single charges can be trapped by the QD during the above-band excitation of the sample, and these will occupy the ground state of the QD. The charge state of the QD therefore fluctuates in time, and three peaks are observed in a time-averaged measurement. The labels indicate the charge of the ground state, X^0 being a neutral exciton (electron-hole pair), and X^- being a charged trion (two electron singlet and one hole). Coulomb interactions will lead to different energies for exciton, trion, and biexciton states, leading to different emission wavelengths.

GaAs and InAs have similar band structures, and both have a direct band-gap between a p-type valence band and an s-type conduction band. The latter has $S = 1/2$ and therefore two-fold degeneracy. In the presence of spin-orbit coupling, the valence band is composed of

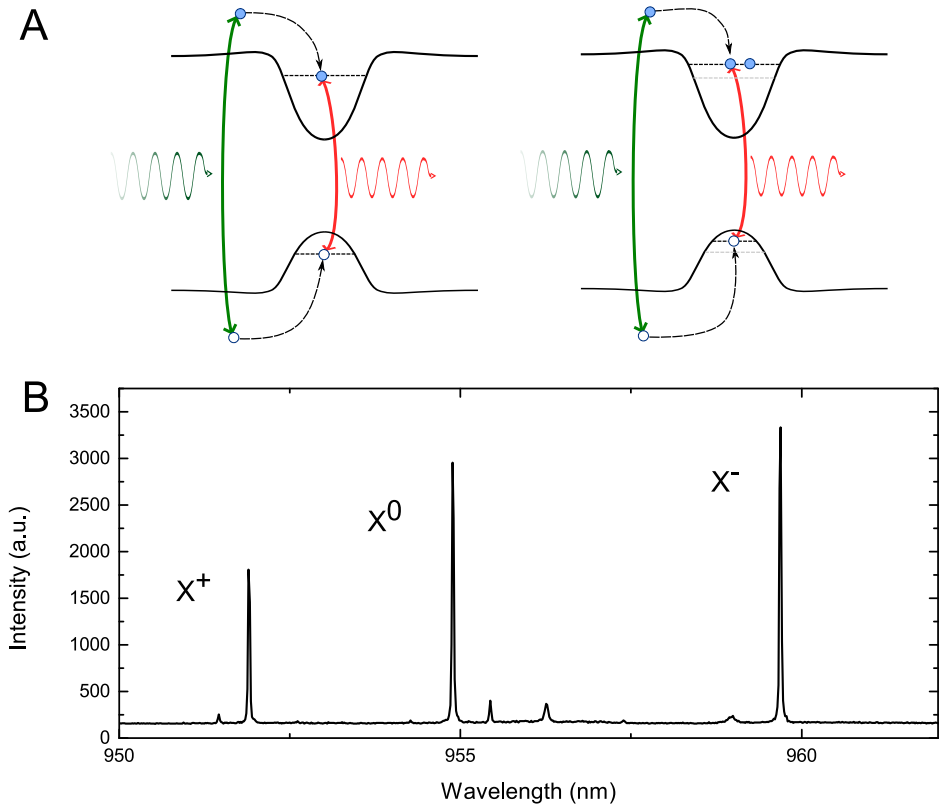

Fig. 1.1 **A.** Schematic diagram depicting photoluminescence from a QD. The filled circles represent conduction band electrons and the hollow circles depict valence band holes. The green arrow represents optical above bandgap excitation, and the red arrow represents exciton recombination along with the emission of a photon. **B.** Example photoluminescence measurement. The labels represent the charge complexes linked to each emission peak.

six $[J||J_z]$ states. Spin-orbit coupling leads a large splitting (0.41 eV in InAs) between the $[1/2||\pm 1/2]$ doublet and the $[3/2||\pm 3/2, \pm 1/2]$ quadruplet. This doublet is referred to as the split-off band. The degeneracy of the quadruplet is further lifted at $k \neq 0$ in bulk due to the influence of other bands (described by the Luttinger Hamiltonian [3]), forming two bands with $\pm 3/2$ and $\pm 1/2$ angular momentum projection at the Γ-point. These are called heavy and light hole bands respectively, due to their differing curvatures in dispersion. In self-assembled QDs, the degeneracy between these two bands at $k = 0$ is lifted by strain, leading to a large energy splitting of tens of meV between the heavy and light hole bands [4]. The heavy-hole band then constitutes the single-particle hole ground state. A combination of heavy-hole and s-type electron has total angular momentum $J = \pm 1, \pm 2$. As photons are spin 1 particles, only the first type of exciton recombination is allowed by an electric-dipole transition. Hence the $J = \pm 1$ excitons are called bright and the $J = \pm 2$ dark.

In the case of the neutral exciton, additional complexity arises from the lowered symmetry of the QD due to the growth process. The anisotropic electron-hole exchange interaction admixes the bright exciton states, giving two orthogonal linearly polarised transitions [4]. This is often called the X-Y splitting ($\approx 10\ \mu$eV) for this reason.

1.1.3 Sample Structure and External Tuning Parameters

Electric field Tuning

Several problems arise from what we have discussed so far. Firstly, self-assembled QD emission energies are tied to their size and morphology which is randomly distributed from dot-to-dot. Secondly, the data shown in Fig. 1.1 shows that multiple charge configurations can exist within the QD. In order to mitigate these effects, we use QDs embedded within a Schottky diode structure shown in Fig. 1.2. An n-doped GaAs layer is grown 35 nm below the QD layer providing an electron reservoir with Fermi energy E_{F}. A semi-transparent Titanium top-contact provides the Schottky barrier. A voltage can be applied between this top-gate and an Ohmic contact to the n-doped layer, thereby tuning the charging energy of the QD relative to the Fermi level of the electron reservoir. Crucially, Coulomb interactions between electrons confined to the QD raise the two-electron charging energy compared with the single electron energy. For temperatures lower than this splitting, the QD can therefore be deterministically charged with a single electron. Working at 4K satisfies this condition. Despite energy-conservation prohibiting further electron tunneling into the QD, a second order process involving simultaneous tunneling to and from the Fermi sea is allowed, called cotunneling. This process gives rise to electron spin relaxation and its rate can be tuned

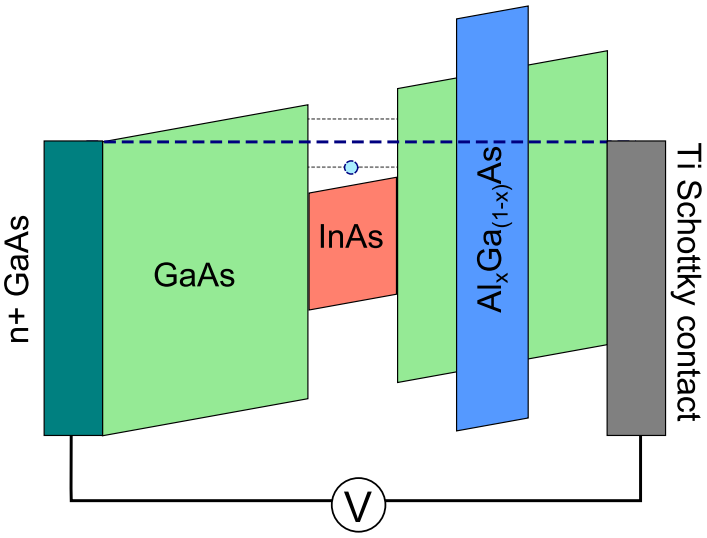

Fig. 1.2 Schematic diagram representing the band structure in the gated heterostructure. The dashed blue line represents the Fermi energy, and the dashed gray lines represent the charging energies within the QD, split by the Coulomb blockade. A voltage can be applied between the Ti Schottky contact and the n-doped layer to tune the charging energy levels relative to the Fermi level.

through the tunnel barrier thickness. The AlGaAs layer between the QD layer and Schottky contact prevents tunneling between these two, due to its larger band gap.

A further benefit of using a gated sample is that it offers us a tuning knob for emission energy through the quantum confined Stark effect. The electron and hole wavefunctions of a confined exciton are spatially separated, to some extent. This electric dipole is affected by external electric fields [5], thereby modifying the electron and hole energy levels and the emitted photon energy after recombination. Thanks to the confinement provided by the QD, the frequency tunability of the emission can be orders of magnitude larger than the linewidth without ionising the exciton, for a given charge configuration.

Charged Exciton Level Structure

Another important experimental tuning knob is given by applying a magnetic field of controlled magnitude and direction. Here, we briefly discuss the impact of such an external magnetic field on the level structure of the QD. As it is of interest for the work shown in this thesis, we will focus on the negatively charged QD level structure. Both the orientation and magnitude of the applied field will significantly modify the emission spectrum through the Zeeman effect. In the experiments shown here, we only use a magnetic field aligned along the growth direction (called Faraday geometry), but it is instructive to also consider the

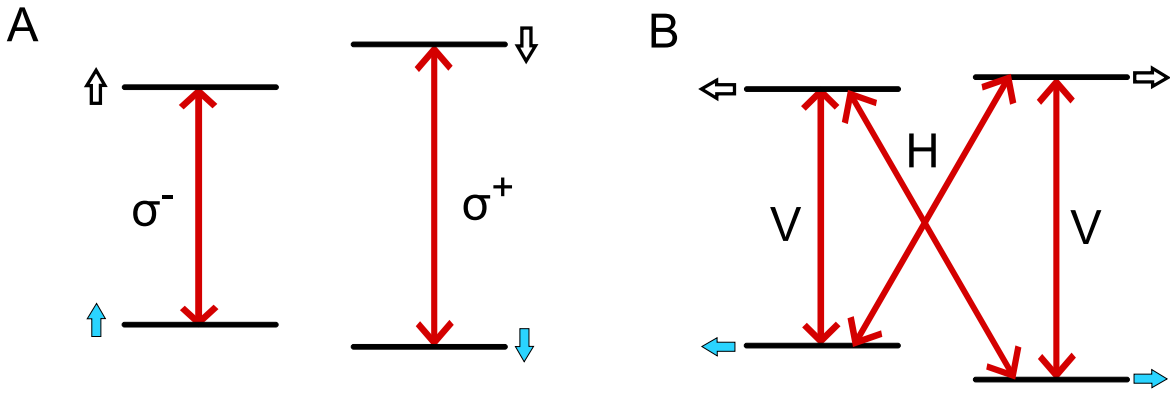

Fig. 1.3 **A.** Trion level structure under an applied magnetic field in the growth direction: the Faraday geometry. The red arrows indicate dipole allowed optical transition. The filled blue arrow represents the ground state electron spin and the hollow arrow represents the heavy-hole pseudo-spin. **B.** Trion level structure under an applied magnetic field orthogonal to the growth direction: the Voigt geometry.

orthogonal (Voigt) geometry, particularly when we come to discuss the effective magnetic field of the nuclei in chapters 5 and 6.

The ground state in a negatively charged QD is given by the electron spin, which can have the following spin projections along the growth direction $\{\,|\uparrow\rangle = |1/2\rangle\,, |\downarrow\rangle = |-1/2\rangle\,\}$. The lowest excited state is composed of two electrons in a singlet state and a heavy-hole spin. The paired electron spins play no role, and the excited states therefore have angular momentum projection $\{\,|\Uparrow\rangle = |3/2\rangle\,, |\Downarrow\rangle = |-3/2\rangle\,\}$. The electron triplet states have significantly higher energies and can safely be neglected here.

In the Faraday configuration, both excited and ground states split according to the hole and electron out-of-plane g-factors, as shown in Fig. 1.3 A. Of the four optical transitions, only two have angular momentum difference $\Delta M = 1$ and are optically allowed. The Zeeman splitting seen experimentally is then given by the difference of electron and hole g-factors. In this geometry we have two separate cycling transitions with ideally no diagonal relaxation. In practice, due to light-heavy hole mixing, the excited states have a finite component with angular momentum $|\pm 1/2\rangle$. The diagonal transitions are then dipole-allowed, which allows for optically-induced electron spin pumping [6].

In the Voigt configuration, shown in panel B, the Zeeman Hamiltonian admixes the z-projections of angular momentum [4]:

$$|\Uparrow\rangle_x = \frac{1}{\sqrt{2}}(|\Uparrow\rangle_z + |\Downarrow\rangle_z)$$
$$|\Downarrow\rangle_x = \frac{1}{\sqrt{2}}(|\Uparrow\rangle_z - |\Downarrow\rangle_z)$$
$$|\uparrow\rangle_x = \frac{1}{\sqrt{2}}(|\uparrow\rangle_z + |\downarrow\rangle_z)$$
$$|\downarrow\rangle_x = \frac{1}{\sqrt{2}}(|\uparrow\rangle_z - |\downarrow\rangle_z)$$

All four transitions between ground and excited states are then optically allowed. In this case ground and excited state splittings are determined by the in-plane electron and hole g-factors. To first approximation, all transitions have equal oscillator strengths and are linearly polarised as indicated in panel B. The presence of spin-flip diagonal transitions allows for ultrafast optical electron spin control [7].

1.2 Quantum Information Processing with Quantum Dots

1.2.1 State of the Art

One of the main motivations for the recent research into optics with quantum dots has been finding a good physical system with which to process quantum information. A spin confined to a quantum dot could provide such a system, and a great deal of research has been done to see whether this system fulfills the DiVicenzo criteria [8] for quantum computation. These criteria give a list of conditions a quantum system must fulfill in order to be useful for quantum information processing. Here, we will briefly summarise the state of the art in QD research compared with these criteria, with a particular focus on negatively charged QDs.

The first criterion is having a well defined qubit. As we have mentioned earlier, QDs allow the trapping of a single electron, for which the spin states can be considered as qubit states. Depending on the magnetic field used, electron spin relaxation between these states is limited by cotunneling processes or phonon-induced decay. This relaxation can be made longer than ms [9, 10], with an appropriate tunnel barrier and at moderate magnetic fields.

The second condition is to be able to initialise the qubit into a pure state. Considering the level structures of Fig. 1.3, this can be done by optical pumping. The rate at which one can initialise this state depends on the branching ratio, and therefore on the magnetic

field geometry. This has been shown both in the Faraday [6] and Voigt geometries [11], and initialisation fidelity higher than 99% can be obtained.

A further criterion states that a complete set of unitary operations is needed, and can be separated into two requirements of full single-qubit control and a two-qubit entangling gate. For single-qubit gates, various forms of coherent spin control have been shown in QDs. The Voigt geometry is the most useful in this instance, as a single electron spin can be manipulated optically through the spin-flip Raman transitions [7]. These optical transitions allow spin control on a timescale of ps through ultrafast pulses. These pulses dress the level structure through the AC Stark effect allowing coherent rotations about one axis of the Bloch sphere, while rotations about an orthogonal axis are achieved either through Larmor precession in the external magnetic field, or ultrafast geometric phase gates [12].

Another criterion concerns the interaction of the qubit with the environment, and how quickly the quantum information stored in the qubit is lost. This is quantified through the coherence time T2 of the qubit and will be discussed in more detail later in this section. How long the coherence time needs to be depends on the time required for qubit manipulation. This ratio is a standard benchmark for the comparison of different quantum systems. With quantum error-correcting codes [13], decoherence times 10^4 times longer than qubit manipulation times would be required. The latter is where QDs figuratively shine, as the qubit manipulation can be done optically on a timescale of ps, much faster than systems requiring microwave spin manipulation.

High fidelity and fast readout of the spin is also required. Again, this can be done optically with QDs. Single-shot readout is only possible in the Faraday geometry [14], due to the quasi-cycling transition. However the transitions have an appreciable spin-flip branching ratio (1:200) which limits the readout fidelity. High fidelity single-shot readout has been achieved with a qubit encoded in a QD molecule [15]. Reaching such a stage in single quantum dots will require further development of non-destructive readout techniques, such as Faraday rotation [6] or Kerr rotation [16] of a probe beam, which could be enhanced to single-shot level by quantum dot spin coupling to a quantum well [17].

Two further criteria concern the interconversion of stationary and flying qubits. Optically-active QDs naturally provide such a link due to its spin-correlated optical transitions. The presence of entanglement between spin and emitted photon required for such a link was shown recently with QDs [18–20]. This brings us back to the two-qubit entangling gate requirement that we mentioned earlier. One feasible architecture with QDs is based on the idea of a 'quantum internet' [21] composed of a set of quantum dot nodes connected by optical links. Entanglement between distant QD spins can then be created probabilistically through, for instance, a Bell state measurement of two photons emitted from each QD. This

effectively transfers the spin-photon entanglement to spin-spin entanglement. Combined with the aforementioned single qubit manipulation, this would satisfy the criterion of a universal set of quantum gates. However, this method relies on photons emitted by different QDs to be quantum mechanically indistinguishable in order to erase which-path information in the entanglement transfer. In this context, the solid-state environment once again comes into play.

1.2.2 Environmental Coupling in Quantum Dots

Although they are sometimes called artificial atoms due to their discrete optical transitions, charges confined to quantum dots exhibit a qualitatively different behaviour. Departures from the atomic picture are caused by the presence of a mesoscopic environment of nuclear spins and charge carriers, as well as coupling to phonon modes of the host lattice.

Hyperfine Effects in Quantum Dots

The SK-grown InGaAs quantum dots used in this thesis have very advantageous optical properties, in terms of quantum efficiency and single-photon quality. However, every naturally occurring isotope of all the atomic elements forming the QD have a nuclear spin: 9/2, 3/2, and 3/2 for the most common isotopes of In, Ga, and As respectively. Charge carriers confined to the QD therefore interact with a large bath of nuclear spins. In fact, the confinement of the carrier wavefunction within the QD exacerbates this interaction compared with a delocalised carrier. Indeed, the reduced size of the sampled nuclear spin bath means that random fluctuations no longer average to zero, leading to appreciable effects even in the absence of nuclear spin polarisation. This interaction can, to a good approximation, be treated as a mean field with a given statistical distribution and correlation time. This effective nuclear hyperfine magnetic field is called the Overhauser (OH) field, after the prediction by Albert Overhauser [22] that such an effective nuclear field can be generated by transfer of electron spin polarisation through the hyperfine interaction. Later, it was demonstrated that optical spin pumping of the electron offers an efficient means of generating significant OH fields [23], and this technique has since been a mainstay of optical studies of nuclear spin effects.

In terms of quantum information processing, random fluctuations of the OH field are problematic for the use of charges confined to QDs as local qubits. Indeed, a finite OH field distribution leads to uncertainty in the instantaneous Larmor frequency of the electron and consequently to spin dephasing. While the electron spin feels an effective magnetic field due to the nuclear spins, the opposite is also true and the nuclear spins precess in the effective

field produced by the electron spin. The two systems feed back onto each other and the dynamics of electron spin relaxation and dephasing are non-trivial. The Merkulov-Efros-Rosen model [24] describes the dynamics of electron spin relaxation in the presence of a random OH field and predicts multiple characteristic timescales. The fastest timescale is linked to the random orientation of the OH filed with respect to the initialised electron spin. The OH field modifies the precession axis shot-to-shot and a time-averaged measurement will exhibit dephasing on a timescale inversely proportional to the OH field dispersion [24]. The second fastest timescale is then linked to precession of the individual nuclear spins about the effective electron magnetic field, or Knight field. This model has been recently validated experimentally for InGaAs QDs, with the first and second timescales of order 1 ns and 300 ns respectively [14]. These two timescales are spin conserving within the QD, and further decay on longer timescales correspond to spin diffusion outside of the QD.
In terms of using the electron spin as a qubit, the hyperfine interaction therefore leads to a short inhomogeneous dephasing time T_2^*. Fortunately, as the nuclear spin diffusion is relatively slow compared to the electron spin manipulation times, much of the fast dephasing can be counteracted by using a spin-echo pulse scheme on the electron spin [25].

The growth process affects the nuclear spin dynamics, and hyperfine effects in the SK-grown QDs under study exhibit significant differences compared with unstrained QDs. The strain field is highly position-dependent within the QD and is maximum at the boundary with the GaAs matrix [26]. This gives rise to inhomogeneous electric fields which interact with the quadrupole moment of the nuclei, giving inhomogeneous spin splittings within the QD [27]. Nuclear spin diffusion through energy-conserving flip-flop processes is therefore suppressed which greatly prolongs the OH field correlation time [28], in the absence of a Knight field. Consequently, nuclear spin polarisation decays slowly compared with unstrained QDs [28, 29] and large degrees of nuclear spin polarisation can be achieved, corresponding to an effective magnetic field of several Tesla [30]. These QDs therefore offer an interesting testbed of a non-Markovian central-spin system.
The Overhauser effect isn't the only method allowing for control of the nuclear spin bath. Resonant optical excitation has also lead to striking observations of dynamic nuclear spin polarisation. In contrast to the Overhauser effect, this form of nuclear spin polarisation is independent on the polarisation of light used, is bidirectional, and is seen in both Faraday and Voigt geometries [26, 31]. This manifests itself experimentally as top-hat absorption spectra with a width up to an order of magnitude larger than the zero-field linewidth, with a hysteresis in laser frequency scan direction. These effects arise due to an effective non-collinear hyperfine term ($\hat{S}_z.\hat{I}_x$), giving qualitatively different behaviour from the well-know flip-flop terms ($\hat{S}_+.\hat{I}_- + \hat{S}_-.\hat{I}_+$) [27, 32, 33].

Finally, despite strain-field induced inhomogeneous broadening of nuclear spin transitions, radio-frequency control has also recently been achieved with self-assembled QDs [34, 35]. All these techniques show viable routes to OH field control and even perhaps a reduction in its fluctuations. Achieving such a narrowing would extend the coherence time of the electron spin without requiring complex dynamical decoupling schemes.

The hyperfine interaction in QDs will be discussed in chapters 5 and 6, particularly in the regime of low-magnetic field and low degree of nuclear spin polarisation. We show that the nuclear spin bath provides a quasi-static quantisation axis for the electron spin, giving a level structure intermediate between the Faraday and Voigt geometries. Optical spin control is then shown to be possible within this level structure.

Optical Linewidth Broadening via Charge Fluctuations and Phonon Coupling

The proposed 'quantum internet' architecture mentioned in the previous section requires reliable spin-photon interfaces, for which the quality of the emitted photon is key. One of the figures of merit of interest here is the indistinguishability of photons emitted at different times or by different QDs, which would ideally be unity for transform-limited emission with identical radiative lifetimes. The aforementioned nuclear spin dynamics will again be important, but other environmental couplings will contribute to a broadening of the emission beyond the transform limit: charge fluctuations within the semiconductor sample and coupling to bulk acoustic phonon modes. Depending on the sample quality, the former can lead to spectral diffusion or blinking of the emission in time. The state of the art in terms of indistinguishability of incoherently generated (postselected) photons from independent QDs is 82%, achieved in resonant excitation, and is limited by such spectral diffusion of both emitters [36].
Different approaches are possible to mitigate the effect of spectral wandering. By moving to the low power limit of excitation, where the emission spectrum follows that of the laser, near-unity indistinguishability can be achieved [37], at the expense of lowered emission probability. However, intensity fluctuations due to spectral wandering can still negatively impact the visibility of two-photon interference measurements [38] even in the coherent emission regime. Embedding the QDs within an optical cavity [39] could lead to a Purcell enhancement of the radiative decay rate thereby broadening the transform limit beyond the inhomogeneous contribution. Alternatively, external controls, such as electric and magnetic fields, can be used as a control knobs for feedback stabilisation of the emission frequency [40–42].

Due to the discrete nature of the energy levels within the QD, phonon coupling does not lead to direct energy relaxation of the confined ground state excitons. However, phonon-assisted radiative recombination occurs, leading to the creation of a broad component of the spectrum [43, 44]. This component is a further source of photon distinguishability. In practice, a spectral filter can be used to reject this part of the spectrum, in which case phonon-assisted processes can be thought of as an added optical loss in the detection path. In self-assembled QDs, this mechanism is a significant contributor to the total photon loss as the phonon-assisted emission typically corresponds to $\approx 10-15\%$ of the total emission intensity. Nonetheless, this value compares favourably with other solid-state emitters, such as nitrogen-vacancy or silicon-vacancy centers in diamond where the emission fraction into the phonon-sideband accounts for $\approx 96\%$ [45] and $\approx 20\%$ [46] respectively.

These two environmental couplings, and their impact on the QD spectrum, are the topic of chapter 4. Instead of treating the phonon-assisted emission as a loss, we show that it can be used to provide feedback stabilisation of the zero-phonon emission, thereby mitigating the effect spectral diffusion arising from charge fluctuations.

Chapter 2

Theory of Resonance Fluorescence from a Two-Level System

The problem of a single two-level atom interacting with a near-resonant electromagnetic field - resonance fluorescence - is a very simple one to state, but has been one of the most studied systems in quantum optics since its inception. It is of interest from a fundamental point of view, as the system is central to the understanding of light-matter coupling. Resonance fluorescence is also of interest as a method of generation of single photons for quantum information processing [47–49], quantum relays [50], and quantum networks [21]. Finally, resonance fluorescence is of particular interest for this thesis as an investigative tool to uncover the solid-state physics affecting the QD. Indeed, compared with incoherent excitation methods such as photoluminescence which creates a large number of interacting free carriers in the environment, resonant excitation below the band gap is relatively non-invasive. In addition, the coherent nature of the light-matter interaction allows emission spectroscopy for which the resolution is no longer limited by the radiative lifetime of the excited state.

The aim of this chapter is to give an overview of the predictions of resonance fluorescence and the theoretical tools used throughout the thesis to calculate observable correlation functions. In the first two sections of the chapter, we will review the textbook theory of resonance fluorescence and state its main predictions about the quantum state of the emitted light, particularly its first and second order coherence. In the third section we will deviate from textbook knowledge and discuss the phase-space properties of resonance fluorescence, particularly in the low power regime. Quadrature squeezing is the predicted outcome of the marriage of wave-like and particle-like characteristics in this regime. The content of this final section is adapted from a manuscript in preparation at the time of writing [51].

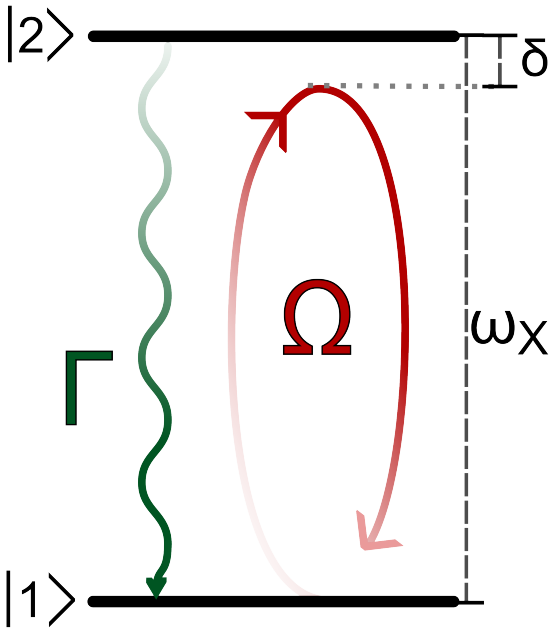

Fig. 2.1 Illustration of a two-level system interacting with a near-resonant electric field. Ω is a parameter related to the amplitude of the driving field and describes the rate of coherent energy transfer between field and atom. Γ is an incoherent decay rate describing the spontaneous emission.

2.1 Semiclassical Model of Light-Matter Interaction

The theory of resonance fluorescence describes the interaction between a two-level system and a near-resonant oscillating electric field and is a standard feature of most quantum optics textbooks [52–55]. Although most of the thesis involves more energy levels due to the presence of a hyperfine interaction, the two-level results illustrate the features of resonance fluorescence useful for solid-state spectroscopy and can be generalised to a system containing both spin and exciton states. The basic picture, along with the relevant physical parameters, is shown in Fig 2.1. Under the dipole approximation, an electric dipole in an electric field is described by the following interaction Hamiltonian:

$$H_{\text{int}} = -\mathbf{D}.\mathbf{E}(\mathbf{R},t) \tag{2.1}$$

where $\mathbf{D} = q.\mathbf{r}$ is the electric dipole moment for charge q and position operator $\mathbf{r}$. $\mathbf{E}(\mathbf{R},t)$ is the electric field at the location of the atom. The interaction between the atom and an intense oscillating electric field can be treated semi-classically, with the field being treated as a classical (linearly polarised) oscillating electric field: $\mathbf{E}(t) = \varepsilon cos(\omega_l t)\,\hat{x}$. After applying the rotating-wave approximation, the interaction Hamiltonian can be written:

$$\begin{aligned} H_{\text{int}} &= \frac{\hbar\Omega}{2}\left[\sigma_+ e^{-i\omega_l t} + \sigma_- e^{i\omega_l t}\right] \\ \Omega &= \frac{e\varepsilon}{\hbar}\langle 2|\,\mathbf{x}\,|1\rangle \end{aligned} \tag{2.2}$$

where e is the electronic charge, and we have assumed that the field is polarised along $\hat{x}$ and both the field amplitude and dipole matrix element have been absorbed into the Rabi frequency Ω. $\mathbf{x}$ is the position operator along $\hat{x}$, $\sigma_\pm$ are the atomic raising/lowering operators and ω_l is the laser frequency. Using the notation of Fig. 2.1, we define the basis as:

$$|1\rangle = \begin{pmatrix} 1 \\ 0 \end{pmatrix};\ |2\rangle = \begin{pmatrix} 0 \\ 1 \end{pmatrix} \tag{2.3}$$

The full Hamiltonian, after neglecting the approximately constant electric field energy term, can be written conveniently in the atomic basis :

$$H = \hbar \begin{pmatrix} 0 & \frac{\Omega}{2} e^{i\omega_l t} \\ \frac{\Omega^*}{2} e^{-i\omega_l t} & \omega_X \end{pmatrix} \tag{2.4}$$

where $\hbar\omega_X$ is the excited state energy. The dynamics of this system are then computed with the Liouville equation:

$$\frac{\mathrm{d}\rho}{\mathrm{d}t} = -\frac{i}{\hbar}[H,\rho] + \mathscr{L}[\rho] \tag{2.5}$$

where $\mathscr{L}[\rho]$ is the Lindblad superoperator describing the irreversible dynamics of the system, namely spontaneous emission and any pure dephasing processes. In the absence of the latter, this superoperator takes the form [52]:

$$\mathscr{L}[\rho] = \frac{\Gamma}{2}(2\sigma_+.\rho.\sigma_- - \sigma_+.\sigma_-.\rho - \rho.\sigma_+.\sigma_-) \tag{2.6}$$

where Γ is the radiative decay rate of the excited state. Equation 2.5 gives rise to a set of coupled differential equations, called the Bloch equations. By flattening the density matrix into vector form and using the fact that its trace is 1, we can rewrite the Bloch equations for

the slowly varying density matrix elements in a simple matrix form[54]:

$$\frac{\mathrm{d}S}{\mathrm{d}t} = -\,\mathrm{M}.S + \Lambda \tag{2.7}$$

$$S = \begin{pmatrix} e^{-i\omega_l t}\rho_{12} \\ e^{i\omega_l t}\rho_{21} \\ \rho_{22} \end{pmatrix}; \Lambda = \begin{pmatrix} i\Omega/2 \\ -i\Omega/2 \\ 0 \end{pmatrix}; \mathrm{M} = \begin{pmatrix} \Gamma/2 + i\delta & 0 & i\Omega \\ 0 & \Gamma/2 - i\delta & -i\Omega \\ i\Omega/2 & -i\Omega/2 & \Gamma \end{pmatrix}$$

where $\delta = \omega_l - \omega_X$ is the laser detuning from resonance and $\rho_{ij} = \langle i|\,\rho\,|j\rangle$. Pure dephasing terms can be added phenomenologically by making the replacement $\Gamma/2 \to \Gamma/2 + \gamma$ in the diagonal terms of M corresponding to the atomic coherences. Solving this equation in the steady-state limit $\frac{\mathrm{d}S}{\mathrm{d}t} = 0$ gives the steady state atomic populations and coherences. Analytical solutions exist for this simple system [53] and for exactly resonant excitation, the steady-state density matrix is given by:

$$\rho_{atom} = \begin{pmatrix} \frac{\Gamma^2+|\Omega|^2}{\Gamma^2+2|\Omega|^2} & \frac{i\Omega^*\Gamma}{\Gamma^2+2|\Omega|^2} \\ \frac{-i\Omega\Gamma}{\Gamma^2+2|\Omega|^2} & \frac{|\Omega|^2}{\Gamma^2+2|\Omega|^2} \end{pmatrix} \tag{2.8}$$

This simple expression is particularly useful as it gives the dependence of the QD populations on the input laser power. This allows for experimental calibration of the laser power without requiring full knowledge of the field amplitude at the QD or its dipole matrix element. For this we use another definition of the Rabi frequency :

$$\Omega = \Gamma\sqrt{\frac{\mathrm{s}}{2}} \tag{2.9}$$

where s is called the saturation parameter and is proportional to the input laser power. From equations 2.8 and 2.9, it follows that the $s = 1$ condition is obtained when the excited state population is half the high-power limit. So far these equations describe the state of the atom only, but in our experiments we always measure the emitted field. In the far-field limit, we can use the relation between source-field operator and atomic operator [53] $E^+_{\mathrm{sf}}(\mathbf{r},t) \propto \sigma_-(t - \mathbf{r}/c)$. Thus we can relate the time dependence of the measured field directly to the time dependence of the atomic operators by making the appropriate substitution.

2.2 Resonance Fluorescence Correlation Functions

Experimental techniques in optics are tailored for the measurement of correlation functions and the experiments presented here are concerned with those of resonance fluorescence

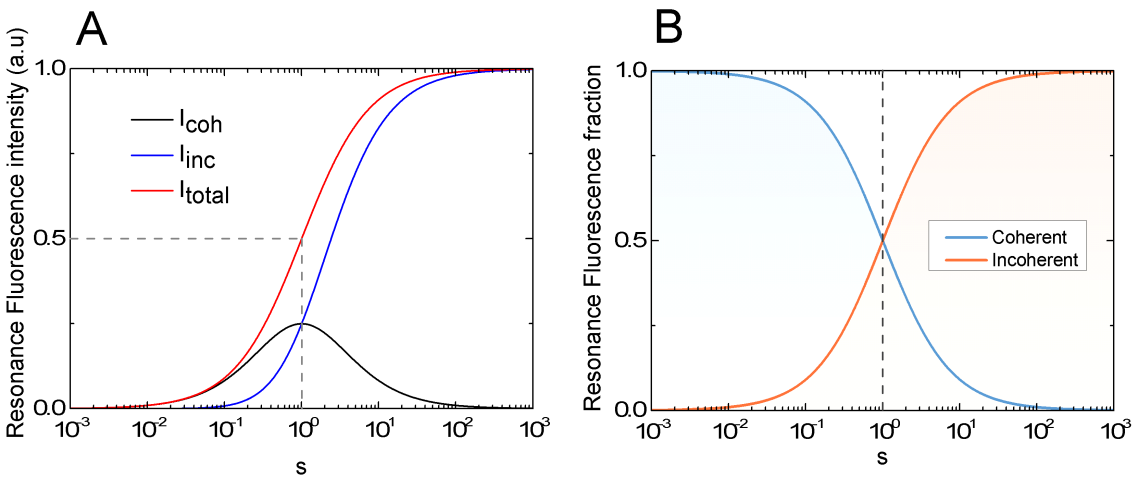

Fig. 2.2 **A.** Power dependence of the different components of the resonance fluorescence intensity. **B.** Incoherent and coherent fractions of resonance fluorescence demonstrating the existence of two power regimes.

from a QD. Analytical expressions exist for the most commonly used correlation functions, but we will not quote them here and instead concentrate on the interpretation of the main results. As we are interested in applying these results to a more complex four-level system, we will present a general method for the calculation of correlation functions which was used throughout the thesis in order to simulate the data. As an example, one of the most often studied correlation functions of resonance fluorescence is the intensity autocorrelation which is a useful tool for the study of the photon statistics of the emission. It is written as follows:

$$\begin{aligned} G^{(2)}(t_1,t_2) &= \left\langle E^-(t)E^-(t+\tau)E^+(t+\tau)E^+(t)\right\rangle \\ &\propto \left\langle \sigma^+(t)\sigma^+(t+\tau)\sigma^-(t+\tau)\sigma^-(t)\right\rangle \end{aligned} \tag{2.10}$$

where we have used the relation between field and atomic operators in the far field limit and neglected the time retardation. Under the Born-Markov approximation, the initial states of the atom and reservoir are separable:

$$\rho(0) = \rho_{atom}(0) \otimes \rho_R(0) \tag{2.11}$$

Defining $U(\tau)$ as the unitary time-evolution operator for the total system of atom and reservoir, the second order correlation can be written:

$$\begin{aligned} G^{(2)}(\tau) =& \mathrm{Tr}\left[\sigma^{+}U^{\dagger}(\tau)\sigma^{+}\sigma^{-}U(\tau)\sigma^{-}\rho\right] \\ =& \mathrm{Tr}\left[\sigma^{+}\sigma^{-}U(\tau)\sigma^{-}\rho\sigma^{+}U^{\dagger}(\tau)\right] \\ =& \mathrm{Tr}_{\mathrm{atom}}\left[\sigma^{+}\sigma^{-}\mathrm{Tr}_{\mathrm{R}}\left[\rho^{'}_{atom}(\tau)\otimes\rho_{R}(\tau)\right]\right] \end{aligned} \tag{2.12}$$

where we have used the cyclic property of the trace, and we have switched from the Heisenberg picture to the Schrodinger picture. Here, $\rho^{'}_{atom}(\tau) = [\sigma^{-}\rho_{atom}\sigma^{+}](\tau)$ is the result of time-propagation of the projected steady state density matrix ρ_{atom}. Equation 2.12 is equivalent to the single time correlation function $\langle\sigma^{+}(\tau)\sigma^{-}(\tau)\rangle$ with the replacement $\rho_{atom}(\tau) \rightarrow [\sigma^{-}\rho_{atom}\sigma^{+}](\tau)$. Equation 2.12 is a specific instance of the quantum regression theorem allowing the calculation of a two-time correlation from single-time expectation values, assuming a Markovian bath. From here, all we need is a method for propagating a general density matrix in time. For this, we effectively trace over the reservoir by calculating the non-unitary evolution given by the Liouville equation. Starting from the Bloch equations written in matrix form given by equation 2.7, the atomic state at time τ takes the following form [54]:

$$S^{'}(\tau) = e^{-M\tau}S^{'}(0) + \mathrm{Tr}[\rho^{'}_{atom}(0)]\left(1 - e^{-M\tau}\right)M^{-1}\Lambda \tag{2.13}$$

where the term $\mathrm{Tr}[\rho^{'}_{atom}(0)]$ has been included to preserve the trace of $\rho^{'}_{atom}(\tau)$. $S^{'}(\tau)$ is a vector of elements of $\rho^{'}_{atom}(\tau)$ defined similarly to equation 2.7.

2.2.1 First Order Correlation Function

The first order correlation function of an optical field describes its phase coherence and is therefore measured with an interference experiment, typically either a Michelson interferometer or a Fabry-Perot etalon. In the Heisenberg picture, this can be written as:

$$G^{(1)}(\tau) = \left\langle E^{-}(\tau)E^{+}(0)\right\rangle \tag{2.14}$$

This expression gives the correlation between the field at time t and time $t+\tau$, and is therefore naturally linked to the coherence time of the field. The zero delay value relates to

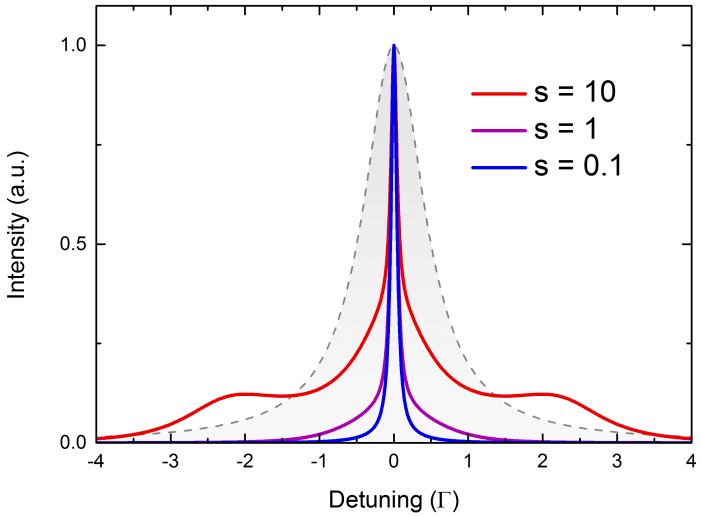

Fig. 2.3 Calculated spectra of resonance fluorescence for different excitation powers of 0.1, 1 and 10. The laser detuning from the bare resonance is zero in all cases. The dashed grey line corresponds to the spectrum of spontaneous emission corresponding to incoherent pumping. A finite spectral resolution is included, which limits the width of the low power spectrum.

the experimentally measured photon count, for integration time T, as follows:

$$\begin{aligned} I &\propto \int_0^T \mathrm{d}t \left\langle E^-(t)E^+(t)\right\rangle \\ &\propto \int_0^T \mathrm{d}t \left\langle \sigma^+(t)\sigma^-(t)\right\rangle = T\,\rho_{22} \end{aligned} \tag{2.15}$$

To gain some insight into the different contributions to resonance fluorescence, we can decompose the atomic operators as follows:

$$\sigma_\pm(t) = \langle\sigma_\pm(t)\rangle + \delta\sigma_\pm(t) \tag{2.16}$$

where $\langle\sigma_\pm(t)\rangle$ is given by the steady state solution to the Bloch equations, and $\delta\sigma_\pm(t)$ is a correction due to the effect of noise operators representing the interaction with vacuum fluctuations in the bosonic reservoir [55]. Inserting 2.16 into 2.15, and using $\langle\sigma_+(t)\rangle = \langle\sigma_-(t)\rangle^*$ we obtain:

$$\begin{aligned} I &\propto \int_0^T \mathrm{d}t\,|\langle\sigma_+(t)\rangle|^2 + \int_0^T \mathrm{d}t \left\langle \delta\sigma^-(t)\delta\sigma^+(t)\right\rangle \\ &\equiv I_{coh} + I_{inc} \end{aligned} \tag{2.17}$$

Here we have separated the resonance fluorescence into two components: I_{coh} which is linked to a coherent energy transfer from the driving field to the atomic dipole and into the resonance fluorescence field, and I_{inc} which is due to spontaneous emission from the atom. These two components have very different first order coherence properties and their relative contributions vary with driving power. We can relate the coherent component of resonance fluorescence to the atomic coherences:

$$\begin{aligned} I_{coh} &\propto \int_0^T \mathrm{d}t \, |\langle \sigma_+(t) \rangle|^2 \\ &\propto T \ |\mathrm{Tr}[\sigma_+ \rho]|^2 = T \ |\rho_{12}|^2 \end{aligned} \tag{2.18}$$

Figure 2.2 shows how the different components of the total emitted fluorescence vary with driving power. Two regimes are apparent: the first is the low power regime ($s < 1$) for which the intensity is approximately linear in driving power and the coherent component dominates, and the high power regime ($s > 1$) where the intensity increases sub-linearly with power while the incoherent component dominates. This can be understood as bleaching of the optical dipole when the Rabi frequency far exceeds the excited state decay rate. The emission tends towards a rate of $\Gamma/2$, showing the phenomenon of saturation characteristic of systems with a finite number of excited states. In this regime, the atomic coherences are averaged out and the steady-state is a statistical mixture of ground and excited states. The main difference between the coherent and incoherent components, as their names suggest, lies in their spectral properties. For a stationary process, the Wiener-Khinchin theorem states that the spectrum $\mathscr{S}$ is given by the Fourier transform of the first order correlation function of resonance fluorescence [55]:

$$\mathscr{S}(\nu) \propto \int_0^\infty \mathrm{d}\tau \left\langle E^-(\tau) E^+(0) \right\rangle e^{-i\nu\tau} + \mathrm{c.c.} \tag{2.19}$$

By separating the slowly varying atomic operators $S^\pm(t) = e^{\mp i\omega_l t}\sigma_\pm$ in the same way as equation 2.16, we can distinguish the coherent and incoherent components:

$$\begin{aligned} \mathscr{S}(\nu) &\propto \int_0^\infty \mathrm{d}\tau \left\langle S^+(\tau) S^-(0) \right\rangle e^{-i(\nu-\omega_l)\tau} + \mathrm{c.c.} \\ \mathscr{S}(\nu) &\propto \left| \left\langle S^+(t) \right\rangle \right|^2 \int_0^\infty \mathrm{d}\tau \, e^{-i(\nu-\omega_l)\tau} + \mathrm{c.c.} \\ &\quad + \int_0^\infty \mathrm{d}\tau \left\langle \delta S^+(\tau) \delta S^-(0) \right\rangle e^{-i(\nu-\omega_l)\tau} + \mathrm{c.c.} \end{aligned} \tag{2.20}$$

The first term, related to the steady-state atomic coherence, gives a delta function centered at the laser frequency. The second component gives rise to other characteristic features

of resonance fluorescence such as spontaneous emission and the Mollow triplet [56]. The Mollow triplet is linked to Rabi oscillations which modulate the excited state population, and their features have a spectral width limited by the excited state lifetime. The full derivation of the resonance fluorescence spectrum is beyond the scope of this chapter, but can be done by numerically solving the equations of motion in the Heisenberg picture and taking their Laplace transform. We refer the interested reader to section 5.3.2 for the calculation of the spectrum of the four-level system. Simulations of spectra for two-level resonance fluorescence are shown in Fig 2.3 and show the transition between coherent emission in the low power regime to incoherent emission characterised by a multi-peak spectrum with widths of order Γ and a splitting corresponding to the Rabi frequency. In this thesis, we are mainly concerned with using resonance fluorescence as a tool to uncover the underlying solid-state physics so we will be focusing on the low power regime which gives us access to sub-linewidth resolution in emission spectroscopy.

2.2.2 Second Order Correlation Function

The second order correlation of the resonance fluorescence field is a widely studied function in quantum optics as it describes the photon statistics of the field. This function can be written as follows:

$$G^{(2)}(\tau) = \left\langle E^-(0)E^-(\tau)E^+(\tau)E^+(0)\right\rangle \tag{2.21}$$

From this expression and the fact that E^-E^+ is proportional to the photon number operator, it is clear that $G^{(2)}(\tau)$ gives the correlation between photon number at t and $t+\tau$. In practice, this is measured by correlating arrival times of clicks on single photon detectors. This function is useful from a fundamental quantum optics perspective as it describes the quantum nature of photon emission from an atom. From a more technical perspective, the second order autocorrelation also holds an imprint of the magnitudes and timescales of intensity noise and is therefore useful as a tool for characterisation of the solid-state environment. In terms of atomic operators, this becomes:

$$G^{(2)}(\tau) = \left\langle S^+(0)S^+(\tau)S^-(\tau)S^-(0)\right\rangle \tag{2.22}$$

It is clear from this expression that the two level nature of the emitter will lead to a zero-time correlation of zero, as $\sigma_+(0)\sigma_+(0) = 0$, whereas the long-time value is $\langle S^+(\tau)S^-(\tau)\rangle^2 = {\rho_{22}}^2$. This condition of a negative value of $G^{(2)}(0) - G^{(2)}(\infty)$, referred to as antibunching, is a frequently used test of a quantum emitter as this effect has no classical counterpart. The

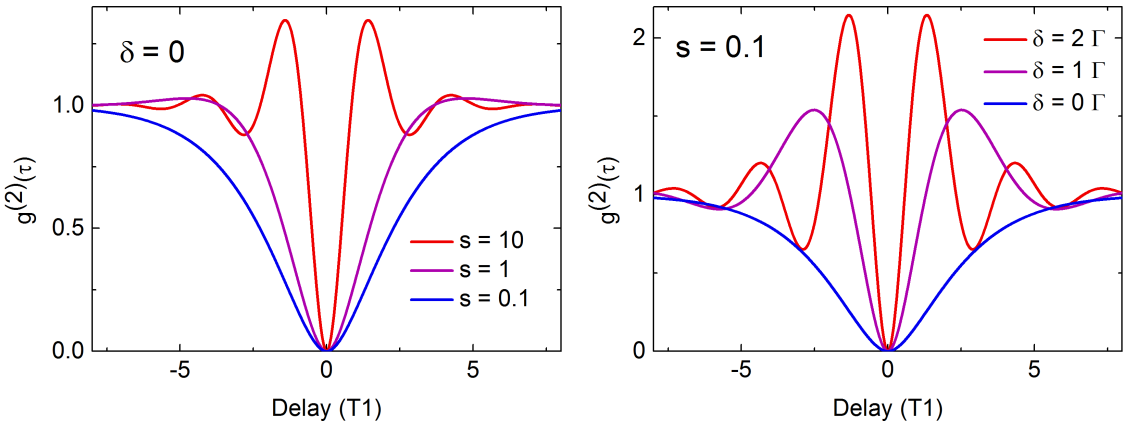

Fig. 2.4 Calculated intensity autocorrelation functions of resonance fluorescence for excitation powers for different driving powers and laser detuning from the bare resonance. T1 is the excited state lifetime.

intensity autocorrelation then maps out the probability of the atom being in the excited state a time τ after being projected into the ground state. Figure 2.4 shows that the antibunching feature at zero delay survives for a wide range of driving powers and detunings. With perfect detectors the antibunching feature would be visible for all powers and detunings, but for realistic timing resolutions the parameter space where this effect is visible becomes finite. The Rabi oscillations seen in the three peaked spectrum of Fig 2.3 can be seen in the time domain in the intensity autocorrelation as oscillations in the excited state probability. Equivalent oscillations are obtained by detuning the laser from resonance leading to the notion of a generalised Rabi frequency $\Omega_{\text{eff}} = \sqrt{\Omega^2 + \delta^2}$.

2.3 Phase Space Distribution of Resonance Fluorescence

In the previous section, we have discussed textbook examples of the first- and second-order coherence properties of resonance fluorescence. Notably we have shown that in the low power regime, the resonance fluorescence field inherits the coherence properties of the excitation laser while showing single photon emission. That is, the emission is phase coherent but the emitted field is not a coherent state. This may seem like a surprising result at first, considering that the phase of a single photon state is undefined [53]. In this section, we will deviate from textbook knowledge and will present an illustrative resolution of this wave-particle duality by looking at the properties of resonance fluorescence in phase space. We will describe a phase-space quasi-probability distribution often used in the quantum optics community: the

Wigner function. With the help of this distribution, we will then provide an intuitive picture of resonance fluorescence accounting for its first- and second-order coherence properties.

2.3.1 Wigner Functions

Phase space distributions are very useful tools in classical mechanics. These distributions describe the joint probability distribution of two variables representing degrees of freedom of the system. When these variables are related, an initial point in phase space will travel along a predictable trajectory. For a harmonic oscillator this trajectory is elliptical for a phase space defined by position and momentum. In quantum mechanics, it is in general not possible to define a joint probability distribution function for conjugate variables such as position and momentum due to the uncertainty principle. However, it is possible to construct distributions which have many characteristics of phase space distributions, while violating one or more of the axioms of probability. These are therefore called quasiprobability distributions. Several such distribution functions are commonly used in quantum optics [57, 58] and we choose to concentrate on the Wigner function [59] which provides a quasiprobability distribution of position and momentum which is well defined for all states, while giving negative values for non-classical states. It is formally defined as the Weyl transform of the density matrix [60, 61]:

$$\mathscr{W}(x,p) = \frac{1}{h}\int e^{-ipy/\hbar}\psi(x+y/2)\psi^*(x-y/2)dy \tag{2.23}$$

It can be seen that this definition has the useful property that the probability distribution in x can be recovered by integration over p, using $\int e^{ipx/\hbar}dp = h\delta(x)$:

$$\int \mathscr{W}(x,p)dp = \psi^*(x)\psi(x) \tag{2.24}$$

Here, we will consider a single mode of the electromagnetic field which is described identically to a harmonic oscillator, with the quadrature operators $\hat{X}_1 = \frac{1}{2}(\hat{a}+\hat{a}^\dagger)$ and $\hat{X}_2 = \frac{1}{2i}(\hat{a}-\hat{a}^\dagger)$ taking the role of position and momentum operators. The nth eigenstate of a harmonic oscillator in the position representation is:

$$\Psi_n(x) = \frac{1}{\pi^{\frac{1}{4}}}e^{-\frac{x^2}{2}}H_n(x) \tag{2.25}$$

Where $H_n(x)$ is the nth Hermite polynomial. By inserting 2.25 into 2.23, we obtain the Wigner function $\mathscr{W}_{|n\rangle\langle n|}$ for the n-photon Fock state:

$$\mathscr{W}_{|n\rangle\langle n|} = \frac{(-1)^n}{\pi}e^{-p^2-x^2}L_n\left[2(p^2+x^2)\right] \tag{2.26}$$

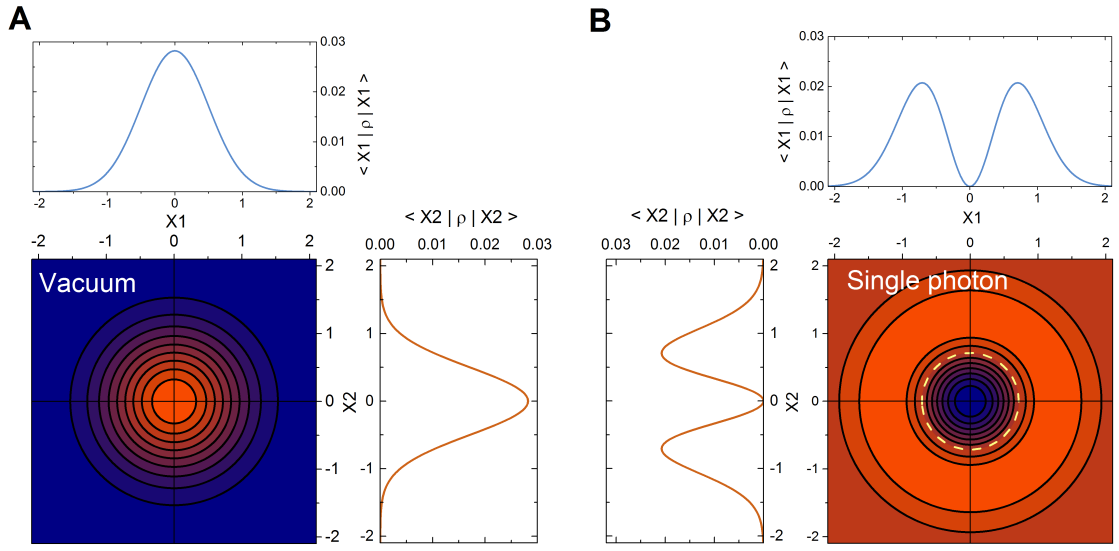

Fig. 2.5 Wigner function and corresponding quadrature distributions for the vacuum state (**A**) and the single photon Fock state (**B**). The dashed yellow line represents the intersection of the Wigner function with the zero plane.

Here, $L_n[x]$ is the n-th order Laguerre polynomial. The $n = 0$ and $n = 1$ Wigner functions are shown in Fig 2.5 along with the marginal distributions describing the single quadrature probability distributions obtained by integrating over the other quadrature. The vacuum state minimises the Heisenberg uncertainty relation for quadrature operators $\Delta\hat{X}_1^2 \Delta\hat{X}_2^2 \geq \frac{1}{16}$, and both marginal distributions are Gaussian with a mean of zero and a finite variance corresponding to $\Delta\hat{X}_{1,2}^2 = \frac{1}{4}$. Coherent states have the same distribution albeit displaced from zero, and any classical state can be described as a sum of displaced vacuum Wigner functions[61] with all features thereby being limited in width by the uncertainty principle. The Wigner function of a single photon state shows straightforwardly why we cannot interpret the Wigner function as a probability distribution. Indeed there is a region around zero for which the distribution is negative which is a direct indication of the nonclassicality of the state. However, for any state, the negative regions are balanced by positive regions such that the observable, the marginal distribution, only contains positive probabilities. The Wigner functions of Fock states have been reconstructed experimentally [62, 63] by measuring the marginal distributions and performing inverse Radon transforms. We also note that the distribution is circularly symmetric about zero, meaning that the single photon state, and indeed any Fock state, has no defined phase.

2.3.2 Squeezing in Resonance Fluorescence

With the Wigner function formalism in our toolkit, we can move on to discuss the state of light in resonance fluorescence. We have already described how to obtain the steady state of the atom under continuous illumination and will use these results here to analyse the emitted state of light. The key point is that the coherent interaction between the driving field and the atomic dipole creates steady state atomic coherences in the rotating frame which will map to a coherent superposition of vacuum and single photon Fock state in the output field. In general, a linear superposition of eigenstates does not lead to a linear superposition of the corresponding Wigner function, and the state of light will exhibit non-trivial properties such as phase coherence with the driving field and quadrature squeezing [64]. We use the relation between field and atomic operators in the far field limit ($\hat{a} \propto \hat{\sigma}_-$) to map the steady state atomic density operator onto the $\{ |0\rangle, |1\rangle \}$ subspace of the outgoing field. For illustrative purposes, we furthermore rewrite the density matrix as a mixture of vacuum and a pure superposition state:

$$\rho_{\mathrm{RF}} = A |\Psi\rangle \langle\Psi| + B |0\rangle \langle 0| \tag{2.27}$$

where:

$$\begin{aligned} |\Psi\rangle &= \alpha |0\rangle + \beta |1\rangle \\ A = \frac{\Gamma^2 + |\Omega|^2}{\Gamma^2 + 2|\Omega|^2}; &\quad B = \frac{|\Omega|^2}{\Gamma^2 + 2|\Omega|^2} \\ \alpha = \frac{\Gamma}{\Gamma + i|\Omega|}; &\quad \beta = \frac{-i\Omega}{\Gamma + i|\Omega|} \end{aligned} \tag{2.28}$$

The Wigner function of the full state is then:

$$\mathscr{W}_{\rho_{\mathrm{RF}}}(X_1, X_2) = A\, \mathscr{W}_{|\Psi\rangle\langle\Psi|}(X_1, X_2) + B\, \mathscr{W}_{|0\rangle\langle 0|}(X_1, X_2) \tag{2.29}$$

Combining equations 2.23, 2.25, 2.28, and 2.29 we obtain:

$$\begin{aligned} \mathscr{W}_{\rho_{\mathrm{RF}}}(X_1, X_2) = &\left(B + A|\alpha|^2\right) \mathscr{W}_{|0\rangle\langle 0|}(X_1, X_2) + A|\beta|^2 \mathscr{W}_{|1\rangle\langle 1|}(X_1, X_2) \\ &+ \frac{4A}{\pi} \Re(\alpha^* \beta (X_1 - iX_2)) e^{-X_1^2 - X_2^2} \end{aligned} \tag{2.30}$$

Wigner functions are plotted for finite driving powers of $s = 0.355$ and $s = 10$ (Fig 2.6) and in the limit of high driving power (Fig 2.7). The low power Wigner function no longer shows the phase invariance of the Fock states. In fact, by inspection of equation 2.30, the chosen phase is determined by the atomic coherence $\rho_{21} = \alpha^* \beta$ which is in turn imparted by the driving field through the complex Rabi frequency. This way resonance fluorescence exhibits wave-like properties despite showing anti-bunching. However, despite appearing similar to a classical field in a first order coherence measurement, the resonance fluorescence state cannot be a coherent state as it displays antibunching [65] and sub-Poissonian statistics [66]. The state therefore must deviate from a displaced vacuum state and becomes distorted as shown in Fig 2.6. In the linear regime ($s << 1$), the resonance fluorescence Wigner function remains approximately Gaussian with a small displacement, similar to a coherent state. As the driving power increases, so does the displacement until the excited state population becomes non-negligible at which point the Wigner function loses its Gaussian character, due to the lack of available multi-photon states. This distortion of the state leads to a redistribution of phase space density from one quadrature to the other. There is therefore a range of driving powers for which the variance in one quadrature is lower than the vacuum state at the expense of increased variance in the other quadrature. This quadrature squeezing can be seen in the individual quadrature distribution of Fig 2.6 A which are compared to the vacuum distributions. Here, the quadrature variance reaches $\Delta X_1^2 \approx 0.219$ corresponding to 87.5% of the vacuum variance. Figure 2.6 B and Figure 2.7 show the behaviour when the driving power increases. In this regime, the atomic coherence decreases with power, leading to a loss of phase coherence with the driving field. In the limit of high driving power, the state is a statistical mixture of the $n = 0$ and $n = 1$ Fock states and the circular symmetry is restored. The quadrature distributions become non-Gaussian and exhibit equal variances twice as large as the vacuum variance. For certain powers, resonance fluorescence therefore exhibits classical first order coherence inherited from the driving field while keeping the quantum nature imparted by the atomic transition. Combining both of these effects naturally leads to the conclusion that quadrature squeezing must also occur. This effect was predicted in 1981 by Walls and Zoller [67] for which the direct experimental demonstration has only recently been achieved [51], validating the full quantum picture of resonance fluorescence.

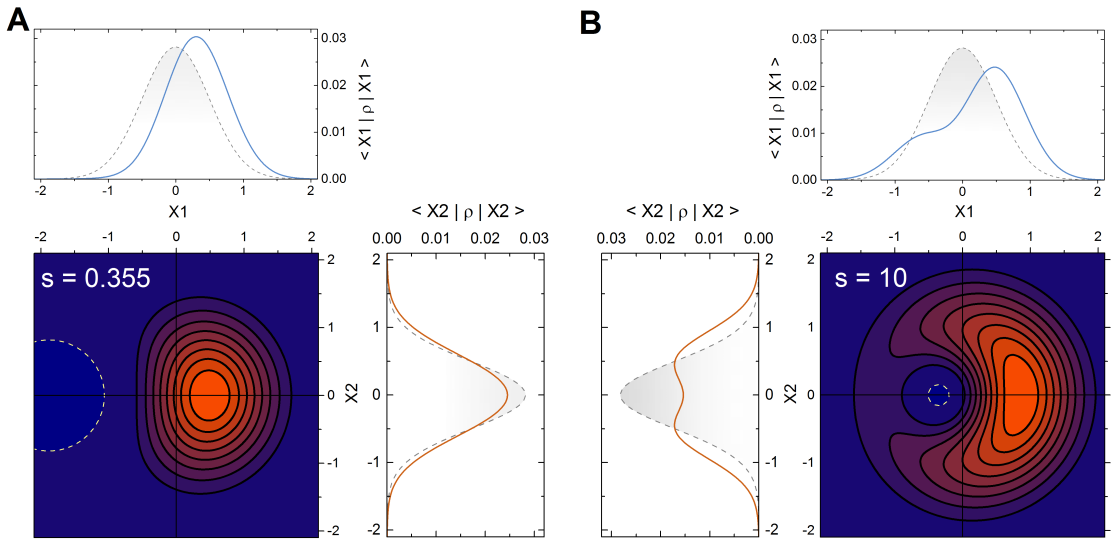

Fig. 2.6 Contour plot showing the Wigner function and corresponding quadrature distributions for resonance fluorescence driving at $s = 0.355$ (A) and $s = 10$ (B). The dashed yellow line shows the intersection with the z=0 plane. The orange and blue curves are the two quadrature distributions, and the dashed grey line is the calculated quadrature variance for the vacuum state.

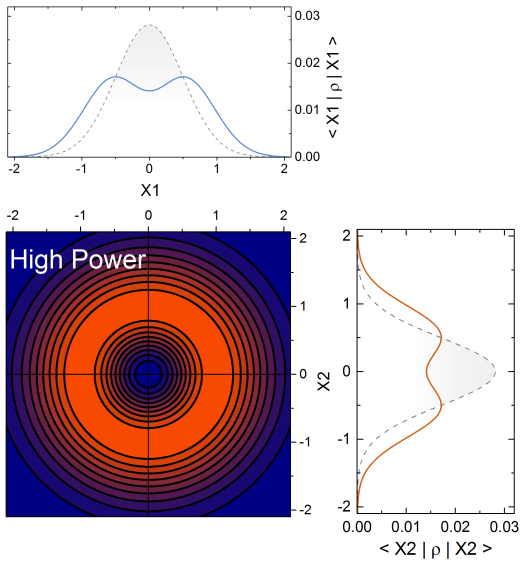

Fig. 2.7 Wigner function and corresponding quadrature distributions for resonance fluorescence driving in the limit of high power

Chapter 3

Experimental Methods for Quantum Dot Resonance Fluorescence

In this chapter, we give an overview of the experimental techniques used throughout this thesis, with a particular focus on resonance fluorescence as the technique of most interest. Resonant excitation of a quantum emitter offers a highly sensitive probe of environmental coupling in QDs and allows for control of a local spin qubit through coherent light-matter interaction [7, 68]. In this context resonance fluorescence is the central technique for the measurements shown in the following chapters, and we will discuss the experimental methods used for measurement of its emission spectrum and photon statistics. We will show measurements taken with a neutral exciton transition alongside the corresponding experimental setup in order to compare with the predictions of chapter 2 and discuss the interpretation of the neutral exciton as a two-level system before moving on to a more complicated level scheme in later chapters. The data shown in this chapter were taken over many years in collaboration with the members of the quantum dot subgroup. In particular, the Fabry-Perot spectral measurement of the neutral exciton transition was taken by Clemens Matthiesen and is presented with his permission.

3.1 Optics with Quantum Dots

3.1.1 Confocal Microscopy

For all of the measurements presented in this thesis, we use a confocal microscope mounted on top of a sample insert. A diagram of the microscope and cryostat is shown in Fig 3.1. The excitation fibre is a polarisation-maintaining single-mode fibre, and is followed by a 18.4 mm focal length aspheric lens for collimation of the beam within the microscope. A

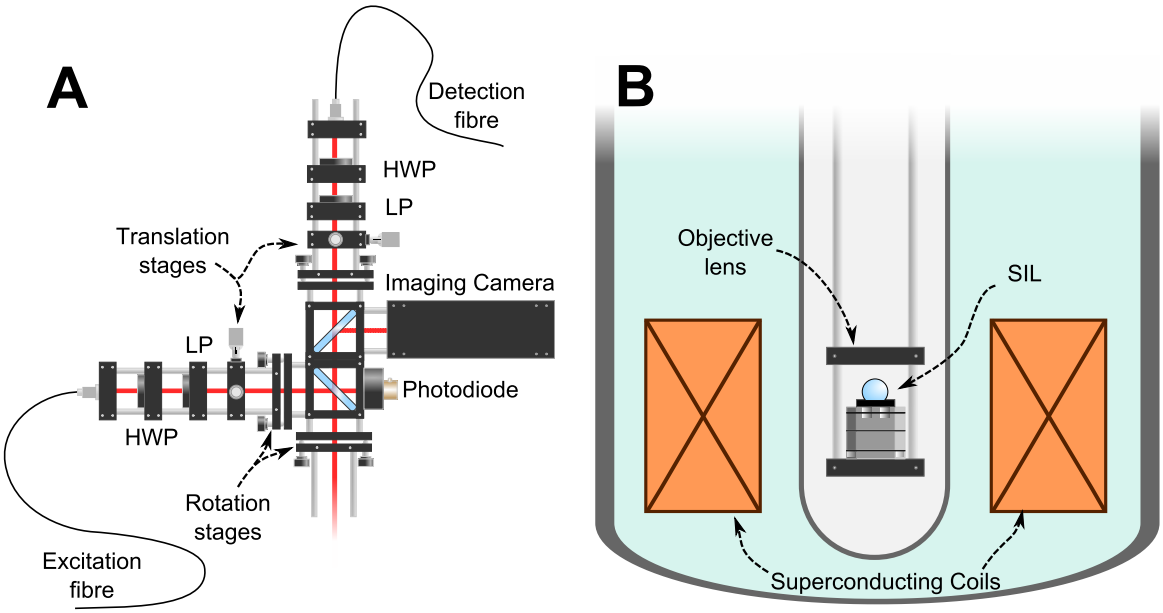

Fig. 3.1 **A.** Diagram of microscope head above the helium bath cryostat. The beam splitters used are designed to give 90% transmission. The translation and rotation stages give four degrees of freedom for excitation and detection arms. HWP: half-wave plate; LP: linear polariser. **B.** Diagram of the sample position within the bath cryostat. The sample is glued to a three-axis nanopositioner stack below the objective lens. Superconducting coils within the cryostat allow magnetic fields up to 7 T at the sample aligned along the optical axis. The electrical connection to the sample gate is not shown.

half-wave plate in the excitation path allows for excitation with arbitrary linear polarisation at the sample. A beam-splitter with 90% transmission reflects part of beam towards the sample, and the transmitted beam is incident on a photodiode to monitor the power. The imbalance in transmission and reflection coefficients minimises the loss of QD photons being transmitted through two beam-splitters. The reading on the photodiode is fed back onto an acousto-optic modulator to stabilise the laser power at the microscope. A single-piece aspheric lens with $NA = 0.5$ is mounted above the sample and acts as the objective lens. Both the laser reflection and the QD emission are collected by the same objective and directed to the detection fibre. A combination of a waveplate (either half-wave or quarter-wave) and polariser can be placed just before the detection fibre in order to reject the laser reflection from the sample. Figure 3.1 shows a typical arrangement of the polarisation optics, but the mounts allow for their removal, and the exact setup can be changed to suit the experimental requirements. The initial collimation of the beam is done with the insert outside the cryostat. Rotation and translation mounts in the microscope arms allow for fine adjustment of the alignment, with four degrees of freedom for both excitation and detection paths. The QD sample is mounted on a set of three-axis nano positioners (Attocube ANC 150/3) within an

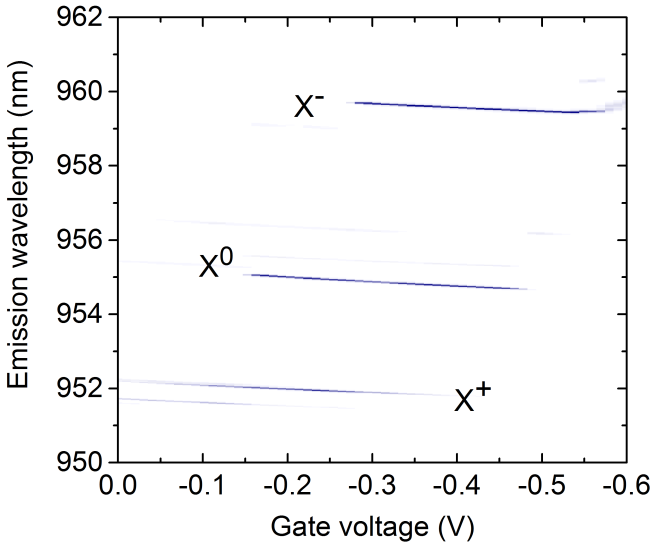

Fig. 3.2 Gate voltage dependence of single QD Photoluminescence taken with an excitation power well below the saturation point of the transitions. The labels indicate the nature of the level system corresponding to each peak. The width of each peak is limited to the resolution of the spectrometer (≈ 0.02 nm).

insert placed in a helium bath cryostat. The sample insert is first pumped to $\approx 10^{-5}$ mbar, and then filled with ≈ 20 mbar of helium acting as an exchange gas for thermalisation of the sample. The cryostat contains a superconducting coil allowing for the application of an external magnetic field aligned along the optical axis (Faraday geometry). The sample under study is grown with 40 alternating layers of GaAs and AlGaAs below the n-doped back contact. This structure forms a distributed Bragg reflector (DBR) optimised for broadband reflection in the near-IR in order to direct more of the QD emission into the objective lens. The high refractive index of GaAs is problematic for extraction of light into vacuum due to the shallow angle of total internal reflection with respect to the optical axis. To mitigate this effect, a super-hemispherical cubic Zirconia solid immersion lens [69] is mounted on top of the sample. We are working in the Weierstrass configuration [70, 71] which theoretically allows for an improvement of n^2 in the effective NA. This is only true for a SIL refractive index matching that of the sample, so, while they are more readily available than GaAs SILs, using a cubic Zirconia SIL ($n = 2.15$ compared with $n \approx 3.54$ at 950 nm for GaAs) is not ideal for extraction efficiency.

Once the optics are aligned, we can start characterising QDs, for which the first step is usually measuring the spectrum of photoluminescence. For this, we send 785 nm diode laser emission through the excitation fibre and couple the detection fibre into a 0.75 m diffraction grating spectrometer (Princeton Instruments Spectra Pro SP-2760) containing a 900 nm

longpass filter to reject the driving laser and luminescence from the GaAs matrix and InAs wetting layer. The dispersed beam is then read out on a liquid nitrogen-cooled CCD array (Acton Spec-10). The spectrometer is first calibrated by measuring the spectrum of a tunable single-mode laser while measuring its frequency on a high resolution wavemeter (High Finesse WS Ultimate). The excitation energy is above the GaAs band gap and therefore generates a large number of excitons which quickly relax to the lowest energy configuration. Some of the excitons decay into the quantum dot to occupy the discrete confined exciton energy levels. Fig 3.2 shows a spectrum of photoluminescence from a single quantum dot. Three discrete emission energies can be seen corresponding to the different charge states in the QD. Photon emission in all three cases is due to the recombination of an electron-hole pair, but the presence of an additional charge in the quantum dot leads to a Coulomb renormalisation of the emission energy leading to three different peaks. The labels beside the peaks describe the charge in the QD ground state. Of course, the data shown in Fig. 3.2 are not sufficient to justify this labelling, but the different charge configurations can be identified with additional polarisation-resolved and magnetic field-dependent photoluminescence [4]. We find that, although the X^0 transition energy varies considerably from dot to dot, the splitting between exciton and trion energies is fairly consistently ≈ 4 nm in our sample. The relative intensities of these three peaks depend on the gate voltage. The electric field tunes the QD charging energies across the Fermi energy given by the n-doped back contact. Therefore certain charge states are allowed in certain gate voltage regions. The gate voltage applied to the sample controls the charge state of the QD to some extent, but one can see significant overlap between the voltage regions showing emission corresponding to different charge states. The same processes describing exciton relaxation into QD excited states also lead to single charge carriers (conduction band electron or valence band hole) relaxing into the QD ground state, and multiple charge complexes are observed at a single gate voltage. A competition between the exciton radiative lifetime and the carrier tunneling rates determines the extent to which the peaks overlap in gate voltage. The emission wavelength is also seen to change linearly with gate voltage, revealing the quantum-confined Stark effect described in chapter 1.

3.1.2 Resonant Excitation

Photoluminescence gives a relatively simple first step to QD characterisation but the amount of information that can be extracted is limited. By its very nature, photoluminescence is a fairly invasive method of probing the QD, as a large number of excitons is generated in its surroundings and we have little control over the charge state of the QD at any given time. We are interested in probing the intrinsic fluctuations in the environment which affect the

QD transition on the order of its linewidth, and therefore a 'cleaner' excitation method is desirable. Resonant excitation provides a more direct method of addressing the transition and allows for resolutions much lower than the radiative linewidth (≈ 240 MHz), whereas the diffraction grating spectrometer has a resolution limited to ≈ 7 GHz. The resolution in resonant excitation is typically limited either by the driving laser coherence or the spectral response of the detection setup. We use frequency-tunable external cavity diode lasers (Toptica DL pro, Toptica TA pro, New-Focus Velocity 6319) for which the emission is single-mode to a good approximation. In practice, their long-time linewidths are limited by our frequency stabilisation protocol. We send part of the laser emission to a wavelength meter , and we feed back onto the laser frequency control. Typically, the remaining frequency fluctuations are ≈ 2 MHz giving a resolution several orders of magnitude lower than the radiative linewidth.

The main practical difficulty with resonant excitation in a confocal setup is separating the reflected driving laser from the QD emission. In principle these two fields do not have identical spectra, but in practice they cannot be separated spectrally by using common filters. Fortunately, there are other degrees of freedom in which the two fields are separable. As described earlier, changes in electric field applied to the QD lead to linear shifts in transition energy. This fact can be used to isolate the QD component of the detected field in a technique known as differential reflection (DR) [72]. Typically, the reflected laser field is several orders of magnitude more intense than the QD field, and the laser background would dominate in a simple absorption spectrum. However, we can use the fact that, in the low laser power regime, part of the QD emission is coherent and will interfere with the laser to perform a homodyne measurement:

$$\begin{aligned} I_{\text{detected}} &= |E_{\text{laser}} + E_{QD}|^2 \approx |E_{\text{laser}}|^2 + 2\,|E_{\text{laser}}.E_{\text{QD}}| \\ &\approx I_{\text{laser}} + 2\eta\cos(\phi)\sqrt{I_{\text{laser}}.I_{\text{coh}}} \end{aligned} \tag{3.1}$$

where I_{coh} is the coherent fraction of the QD resonance fluorescence intensity, ϕ is the relative phase between the QD emission and laser, η is a factor accounting for the different polarisations of reflected laser and resonance fluorescence, and we have assumed $|E_{\text{coh}}|^2 \ll |E_{\text{laser}}|^2$. The first term of equation 3.1 is the dominant term but we can subtract it by using the implicit dependence of the second term on gate voltage. For this, we modulate the gate voltage with an amplitude larger than the exciton radiative linewidth and demodulate the intensity measured on a photodiode at the same frequency with a lock-in amplifier. The constant term in equation 3.1 is thereby eliminated and we are left with a signal of amplitude proportional to $\sqrt{I_{\text{laser}}.I_{\text{coh}}} \propto \sqrt{s}\,|\rho_{12}|$. DR is a useful method for probing the steady-state

atomic coherence, but doesn't give access to the QD photons, making measurements such as the intensity autocorrelation of resonance fluorescence impossible. In addition, the measurement relies on integrating the signal over a few modulation periods, meaning that the measurement bandwidth is limited by the gate RC constant.

Another degree of freedom we can use to separate QD emission from reflected laser is polarisation. Typically, we drive the QD with a linearly polarised laser, which can therefore be suppressed with another linear polariser in the collection arm. The polarisation of the QD resonance fluorescence is determined by the transition selection rules, which in general don't coincide with the driving laser polarisation and the QD emission will be partly transmitted by the detection polariser. In practice, we minimise the laser throughput for a given excitation polarisation by rotating the collection polariser and then iterate for different excitation polarisations in order to find a global maximum in the extinction ratio. Typically this ratio reaches values of order $10^7 - 10^8$ and is highly frequency dependent. The use of a SIL is helpful in this context, as it reduces the size of the focal spot. This means that less laser power is required to saturate the QD and the signal-to-background ratio increases. In addition, it is sometimes necessary to add a diffraction grating between the laser and the excitation fibre to improve the laser spectrum when it shows broadband emission due to enhanced spontaneous emission as well as a single-mode peak. This can improve the polarisation extinction ratio by several orders of magnitude depending on the laser used. With this extinction ratio, we routinely achieve signal-to-laser background ratios above 100 at $s = 1$ measured with single photon counting avalanche photodiodes. The half-wave plate following the polariser in the detection arm is used to match the axis of the polarisation-maintaining fibre in order to avoid intensity fluctuations at the output due to motion of the fibre.

These two methods are central to the measurements shown in this thesis and are common techniques within the QD community, but both have their own advantages and disadvantages. DR is a simple technique to implement and allows for arbitrary excitation polarisation but leaves no access to the QD photons and suffers from a bandwidth limited by the gate. Polarisation suppression on the other hand gives access to the QD single photons and allows measurements of the first and second order correlation functions described in chapter 2 at the expense of freedom in excitation frequency and polarisation. A third measurement technique, developed for the measurements shown in this thesis, allows for both access to resonance fluorescence photons and excitation with multiple frequencies and polarisations. This method relies on spectral separation of phonon-assisted resonance fluorescence and is further described in chapter 4 when the exciton-phonon coupling is discussed in more detail.

3.2 Resonance Fluorescence Spectroscopy and Photon Statistics

3.2.1 Absorption Spectroscopy

The first step in resonant characterisation of a QD typically consists of a measurement of the DR contrast as a function of laser frequency and gate voltage. An example two-dimensional DR map is shown in Fig. 3.3 and gives a far more precise value for the transition frequency and DC Stark shift compared with non-resonant excitation. In most measurements, it is more convenient to change the gate voltage rather than the laser frequency and an accurate measurement of the Stark shift is therefore needed to calibrate the laser detuning in frequency units. Figure 3.3 B shows a typical low-power DR measurement as a function of laser detuning from resonance for a given laser frequency. As discussed in Chapter 1, the X^0 transition consists of the transition between the crystal ground state and a heavy-hole exciton. The degeneracy between the two heavy-hole excitons is lifted by the strain field in the quantum dot giving an anisotropic electron-hole exchange term [4]. Two peaks are apparent with a splitting (commonly called the X-Y splitting) determined by the anisotropic exchange term. Both transitions have similar oscillator strengths, and the relative size of the two peaks is mainly determined by the excitation polarisation. By varying the angle of the excitation polarisation, one can see that the relative contributions are anti-correlated and each peak can be suppressed at angles differing by 90 degrees. Hence, the two transitions are linearly cross-polarised with each other. In Figure 3.3, the suppressed peak is still visible due to finite ellipticity of the excitation polarisation at the sample location. What we are dealing with then is a three level system. However, if the X-Y splitting is large compared with the linewidth, spectral and polarisation selectivity allow us to isolate a two-level system. This QD shows a small X-Y splitting of 1.8 GHz compared to the typical value of ≈ 6 GHz observed with this sample.

As discussed in chapter 2, two-level effects appear in a wide variety of measurements. One of the simplest measurements, and one which is typically used to calibrate the Rabi frequency, is power-dependent absorption spectroscopy. These reveal saturation effects in different forms: the total fluorescence intensity reaches a maximum as the driving power is increased while the absorption linewidth begins increasing linearly with Rabi frequency [53]. Furthermore, the transition between the two power regimes is reflected in a decay of the coherent fraction of the fluorescence intensity. The latter effect can be probed straightforwardly with DR measurements, as these rely on the interference between the resonance fluorescence field and the reflected laser. When the laser intensity dominates over the QD

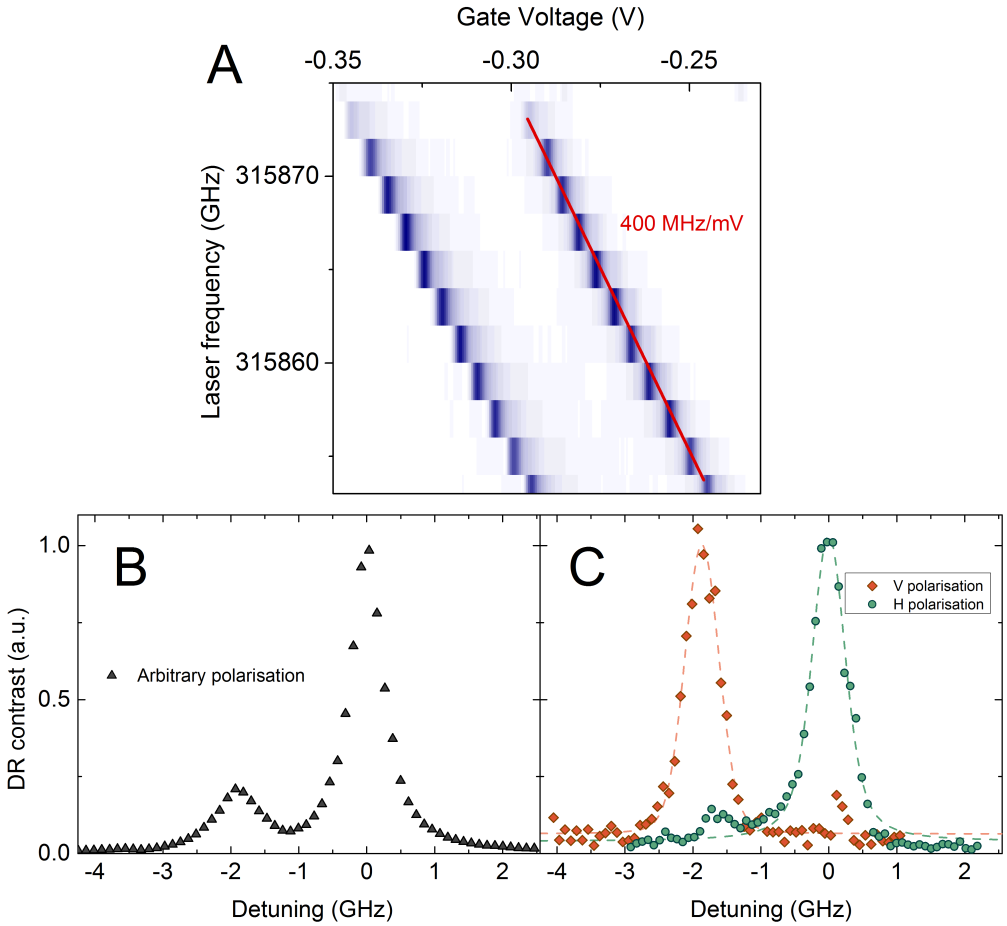

Fig. 3.3 **A.** 2D map of DR as a function of gate voltage and laser frequency. The linear shift in resonance frequency is due to the DC Stark effect. Measuring the gradient allows a conversion between laser frequency detuning and gate voltage detuning. **B.** DR measurement as a function of laser detuning from resonance for a fixed laser frequency. The excitation polarisation is linear at an arbitrary angle with respect to the neutral exciton transitions. **C.** DR measurements with excitation polarisations matching one of the two transitions. All curves are normalised to the peak of Voigt fits.

intensity, the measured contrast as a fraction of the total intensity on the photodiode is proportional to $\sqrt{\frac{I_{\text{coh}}}{I_{\text{laser}}}} \propto \frac{|\rho_{12}|}{|\Omega|}$. Figure 3.4 shows a power dependence of the DR contrast and resonance fluorescence count rate. In the low power regime, the fluorescence intensity is linearly dependent on driving power and is mainly due to I_{coh}, which explains why the DR contrast is constant while the RF counts increase linearly. The subsequent drop in DR contrast reflects the transition to incoherent fluorescence, while the RF count rate starts to show sub-linear behaviour. These two effects can be used to calibrate the saturation power. Assuming the reflected laser power is the main contribution to the total intensity (i.e. the contrast is small), the point of half maximum contrast directly gives $s = 1$. For the RF measurement, $s = 1$ corresponds simply to the point of half maximum count rate. For this QD, we find maximum resonance fluorescence count rates of 1.6 MHz. From the two level theory, we expect the emission rate to saturate at $\frac{\Gamma}{2}$ which, considering the measured lifetime of $T_1 = 0.58$ ns, would give a maximum emission rate of 862 MHz. The discrepancy arises from a large number of factors, which can be separated into a product of collection efficiency and detection efficiency. We use Si APDs which typically have detection efficiencies of $\approx 20\%$ at a wavelength of 950 nm meaning the efficiency of collection into the detection fibre is around 0.9 %. One of the main factors limiting this value is the fraction of dipole radiation which is directed to the 0.5 NA objective lens, even with the aid of a DBR and SIL. Further effects such as finite transmission of the optics, fibre coupling efficiency and partial polarisation rejection of the RF account for the rest of the collection efficiency.

Saturation of the two-level absorption also leads to an increase in absorption linewidth. In an ideal system, the low-power spectrum is Lorentzian with a linewidth given by the excited state lifetime $\Delta\nu = \frac{1}{2\pi T_1}$. In this sample, the spectrum is typically a composite of Lorentzian and Gaussian distributions and exhibits a linewidth $\approx 2\Delta\nu$. This is the first indication that the two-level approximation is incomplete for such a solid-state emitter, where interactions with a fluctuating environment lead to inhomogeneous broadening. This broadening is caused by charge fluctuations in the sample and hyperfine coupling to an uncontrolled nuclear spin environment. The former will be the main topic of interest in Chapter 4, while the latter will be studied in further detail in Chapters 5 and 6. Reference [73] shows a dependence of the absorption linewidth on laser frequency sweep rate, showing that the increased width is not caused by pure dephasing of the transition.

3.2.2 Emission Spectroscopy

Absorption spectroscopy allows us to probe the steady-state atomic population ρ_{22} and coherence $|\rho_{12}|$ but misses key features of resonance fluorescence such as Rabi flopping. Additionally, Fig. 3.4 A. shows the expected drop in coherent fraction as the driving power

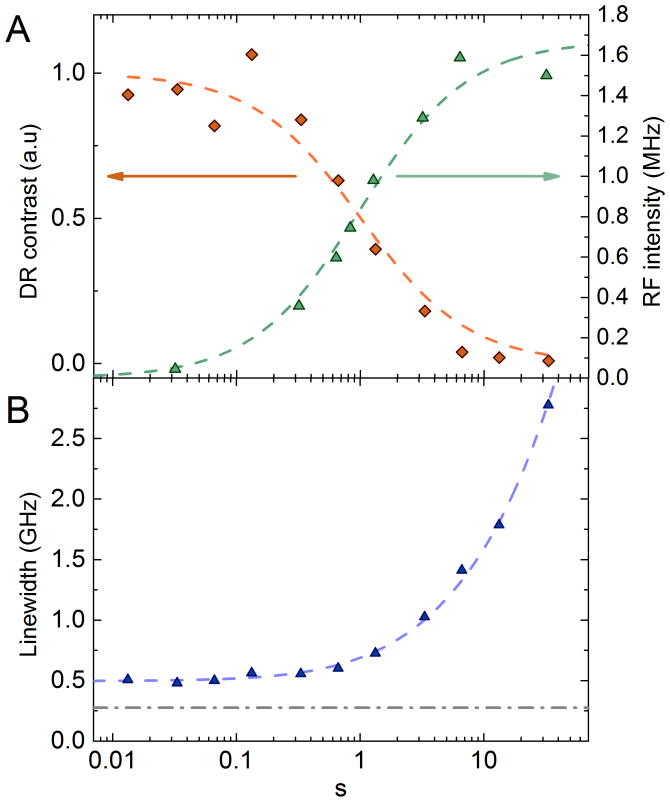

Fig. 3.4 **A.** Peak DR contrast (orange circles) and peak resonance fluorescence count rate (green triangles) as a function of driving laser power . The dashed orange curve is a fit to the functional form of $\sqrt{\frac{I_{\text{coh}}}{s}}$ and the green curve is a fit to the functional form of I_{total}. **B.** Resonance FWHM extracted from individual Voigt fits to the lineshape as a function of driving power. The dashed curve is a fit of the form $\sqrt{A+Bs}$. The dashed grey curve represents the expected low power FWHM given by the transform limit $1/(2\pi T_1)$ for an ideal two-level system.

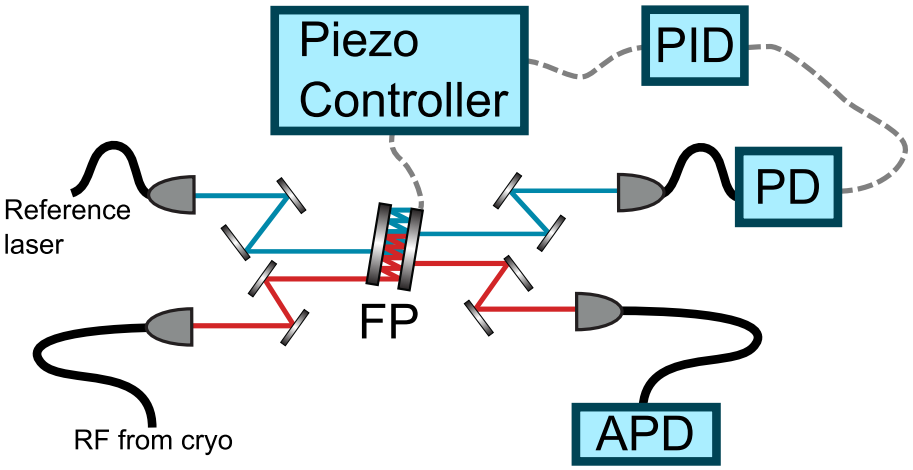

Fig. 3.5 Diagram of the scanning Fabry-Perot (FP) interferometer setup. The reference laser (blue beam) transmission is recorded on a photodiode (PD), the output of which is used as an input to a PID controller. The output of the PID is fed back to the controller to control the cavity length via a piezoelectric transducer. The resonance fluorescence collected from the microscope (red beam) is simultaneously sent through the cavity and the transmission is recorded on an avalanche photodiode (APD).

increases, but only gives us a decay relative to the low-power value and therefore limited information on the first order coherence. To measure the first order coherence of resonance fluorescence, we use a scanning Fabry-Perot interferometer setup shown in Fig. 3.5. A frequency-stabilised reference laser is sent through the FP and the throughput is measured on a photodiode. The cavity is composed of two confocal mirrors, for which the relative alignment is controlled by three piezoelectric transducers and one piezoelectric transducer controls the distance between the mirrors. The initial cavity alignment is done by ramping one of the voltages and minimising the width of the transmission peak with the other piezo actuators. Once the cavity is aligned, scanning the reference laser frequency gives a Lorentzian transmission peak of typically 20 MHz FWHM.

The cavity length is initially set to give half-maximum transmission of the reference beam, and this transmission is fed back via PID control to the controller to stabilise to this setpoint. Changing the reference laser frequency thereby tunes the cavity resonance by the same frequency difference. The signal from the detection fibre is simultaneously sent through the cavity and recorded on an APD. The peak transmission is typically on the order of 10% and the integration times used are therefore much longer than for an absorption spectrum. A comparable spectrum is taken by tuning the QD off resonance via gate voltage in order to measure the spectrum of laser leakage. This reference spectrum is then subtracted from the raw data to obtain the resonance fluorescence emission spectrum.

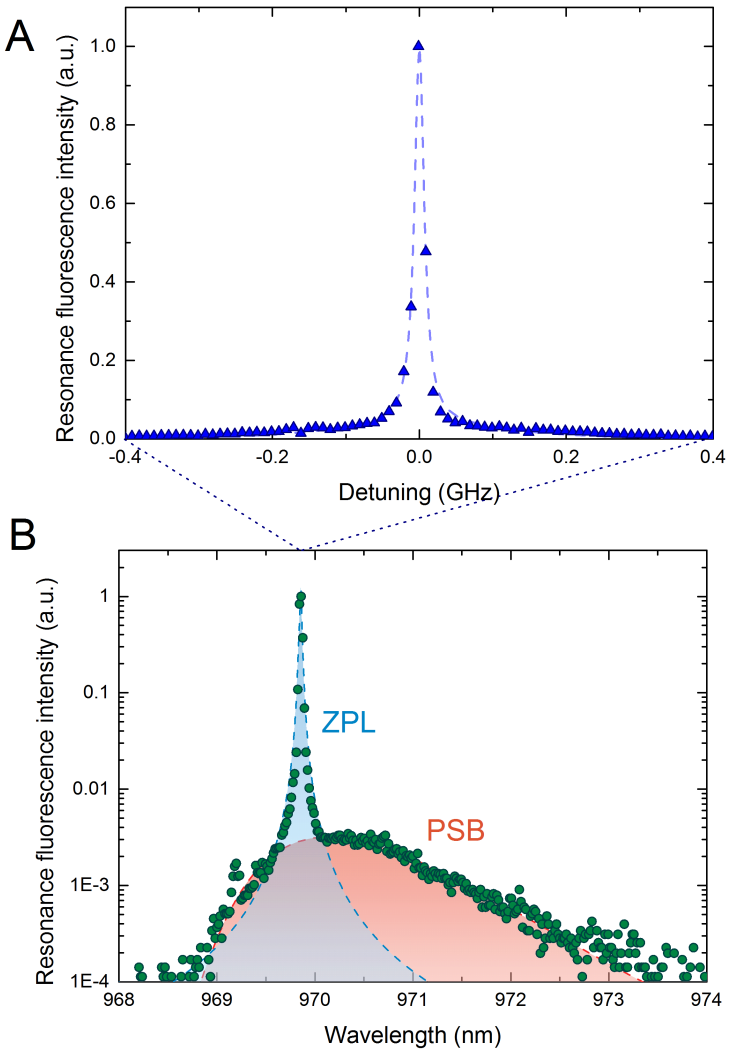

Fig. 3.6 **A.** X^0 emission spectrum taken around $s = 1$ with a Scanning Fabry-Perot measurement. The width of the spectrum is limited by the Fabry-Perot linewidth of ≈ 16 MHz. The dashed line is a two-level simulation including the experimental parameters of driving power and spectral resolution. **B.** X^0 emission spectrum taken at a similar driving power with a grating spectrometer. The dashed curves are guides to the eye. ZPL stands for zero-phonon line and PSB stands for phonon side-band. A background measurement with the QD off resonance was subtracted for both measurements.

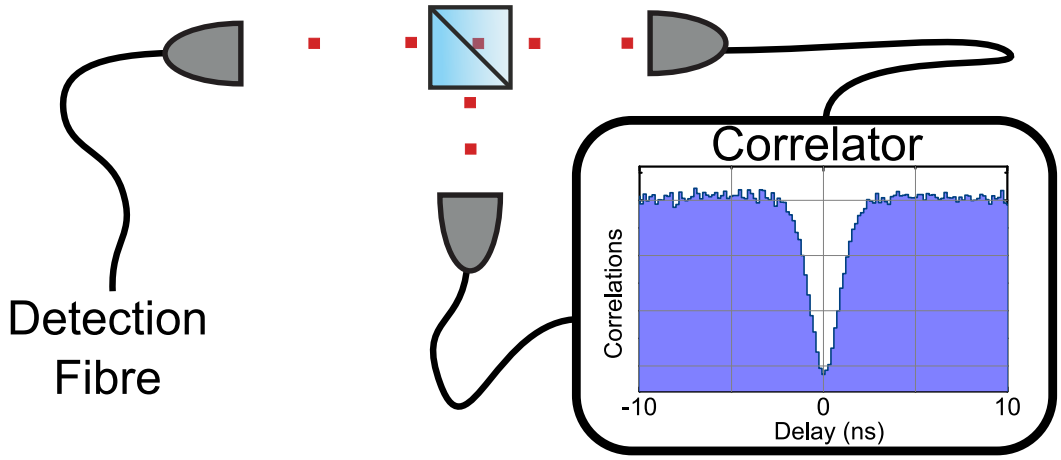

Fig. 3.7 Diagram depicting a Hanbury Brown and Twiss setup for measurement of resonance fluorescence intensity autocorrelation.

Figure 3.6 shows emission spectra measured with two methods: the first obtained with the scanning FP with a spectral resolution of $\approx$ 16MHz and a free spectral range on the order of a few GHz, and the second with a grating spectrometer with a resolution of order 10 GHz and a much larger detuning range. The FP measurements show a low power emission spectrum consistent with a two-level picture: a sub-linewidth peak due to coherent emission is present on top of a broad peak due to incoherent emission. The presence of a large proportion of coherent emission in the low power regime suggests that the neutral exciton transition suffers little from pure dephasing [37, 74] and is consistent with a simple two-level picture. The second measurement, in contrast, shows a broad sideband in addition to the narrow peak centered at the laser frequency. This sideband stems from exciton coupling to bulk acoustic phonon modes [43, 44] leading to phonon-assisted fluorescence even in the low power regime. The phonon sideband typically accounts for $10-15\%$ of the total emission intensity and leads to a ps timescale decay of the first order coherence [75]. This phonon coupling, and its impact on spectral indistinguishability, is covered in more detail in chapter 4.

3.2.3 Intensity Autocorrelation

As discussed in chapter 2, the intensity autocorrelation function gives useful information both on the quantum nature of photon emission in resonance fluorescence and on the classical noise sources affecting the emission. With an ideal detector and no photon loss, one would simply need to record arrival times of all photons and then compute the distribution of time delays between photons. However, technical limitations in realistic detectors have led to the adoption in the quantum optics community of a different correlation method called the

Hanbury Brown and Twiss setup shown in figure 3.7. Single photon detectors, such as the avalanche photodiodes used in this work, suffer from a recovery time after detecting a photon during which no detection can be made. For the detectors used here this dead time ranges from 30 ns to 50 ns. Antibunching, with features on the order of the radiative lifetime, therefore cannot be seen with a single detector setup. Instead, a 50/50 beam splitter is used to split the resonance fluorescence field which is then measured on two separate detectors. One detector is labeled 'start' and the other 'stop'. The electronic correlator (quTau time-to-digital converter) then builds a histogram of arrival times of 'stop' pulses conditioned on the arrival of a 'start' pulse. The exact algorithm used to build up the histogram depends on the correlator used. In the case of the quTau, once a 'start' pulse is detected, a correlation count is added for every subsequent 'stop' received until a new 'start' pulse is detected. If no 'stop' pulse is detected within a set time window, no correlations are added to the histogram and the correlator waits for another 'start' pulse. In the limit of low count rates, the histogram generated is equivalent to the intensity autocorrelation function multiplied by a constant factor determined by the collection and detection efficiencies. At high count rates, such that the probability of detecting two 'start' pulses within the time window is significant, the long-delay coincidences are underestimated. In fact, the histogram decays exponentially with a timescale corresponding to the mean 'start'-'start' delay. One way of correcting for this effect is to introduce loss in the resonance fluorescence (e.g. by insertion of a neutral density filter) such that the 'start'-'start' mean delay is long compared to the time window, or one can fit the exponential decay $e^{-t/\tau}$ and correct by dividing the measured histogram by $(1-e^{-t/\tau})$. The first option leads to a longer histogram acquisition time, so we usually opt for the second option. An electronic delay between the 'start' and 'stop' signals offsets the zero-delay point to a finite delay in the electronics, and the correction described above therefore does not accidentally correct for classical noise sources which would also appear as exponential decays.

Figure 3.8 shows intensity autocorrelation measurements of resonance fluorescence from the X^0 transition for two driving powers. The zero delay value is below 0.5 for both of these demonstrating that we indeed have a two-level system emitting single photons. However, there is significant deviation from the ideal two-level theory, particularly for the high power measurement where $g^{(2)}(0) \approx 0.3$. This is mostly due to the finite timing resolution of the HBT setup determined mainly by the timing jitter of the APDs used. The timing resolution of the HBT setup is obtained independently by measuring the width of pulses emitted from a mode-locked Titanium-sapphire laser at a similar mean count rate. The width of these pulses is less than 2 ps, whereas the width obtained via HBT measurement is typically ≈ 600 ps. Further deviation from the simple two-level theory is introduced because of the

inhomogeneous broadening caused by the environment. Therefore, Rabi flopping is not tied uniquely to laser power even when the mean detuning is zero, and the Rabi frequency tends to be higher than one would expect for a given driving power. In most simulations in this thesis, this broadening is included by averaging over a Gaussian distribution of detunings which is QD-dependent. On timescales far longer than the radiative decay, we observe a flat autocorrelation. This suggests that there is no significant decay into a dark state on a longer timescale.

We also use intensity autocorrelation measurements as a probe of the impact of environmental fluctuations on resonance fluorescence. These fluctuation timescales are typically far greater than the dead time of our detectors, therefore we can use a single detector in order to reduce the integration time needed. In classical optics, the intensity autocorrelation can be written [76]:

$$G^{(2)}(\tau) = \lim_{t\to\infty} \langle I(t+\tau)I(t)\rangle \tag{3.2}$$

where $I(t)$ is the field intensity at time t. Practically, this can be measured by taking a timetrace of resonance fluorescence for a given time T and time bin t_{bin}. To obtain an autocorrelation from a single timetrace, we do the following. We take two subsets of length T' from the initial timetrace, one starting at $t = 0$ and the other at $t = \tau$. We then multiply these two traces, element-by-element, and take the mean of the resulting vector. In the limit of large T', this value is equivalent to the right hand side of equation 3.2. By first subtracting the mean count rate squared, and then dividing by the same value, we obtain a normalised $g^{(2)}(\tau) - 1$. An example intensity autocorrelation of X^0 resonance fluorescence obtained with a single detector is shown in figure 3.9. This autocorrelation is the average autocorrelation of 10 timetraces taken under the same experimental conditions, with $T = 10$ s and $t_{\text{bin}} = 200\mu s$. The simple two-level model predicts that correlations in the resonance fluorescence intensity should decay on a timescale of order Γ. However correlations still persist at timescales of ms and even seconds, betraying relatively slow environmental fluctuations. One has to be cautious in assigning these fluctuations to the solid-state environment of the QD, as the correlations could also arise from more trivial technical reasons, e.g. electronic noise on the gate or intensity fluctuations caused by motion of the detection fibre. However, the fluctuations on the timescales shown are highly detuning- and power-dependent suggesting that the intensity noise is in fact related to frequency fluctuations of the transition [73, 77].

The measurements presented in this chapter show that, in many ways, the neutral exciton transition of a quantum dot behaves as a two-level system. Indeed, the short-time photon statistics show that it is a good single photon emitter and that it doesn't suffer significantly from decay into dark states. Furthermore, the presence of coherent emission at low powers signifies that the transition doesn't suffer from pure dephasing. However, the presence of the

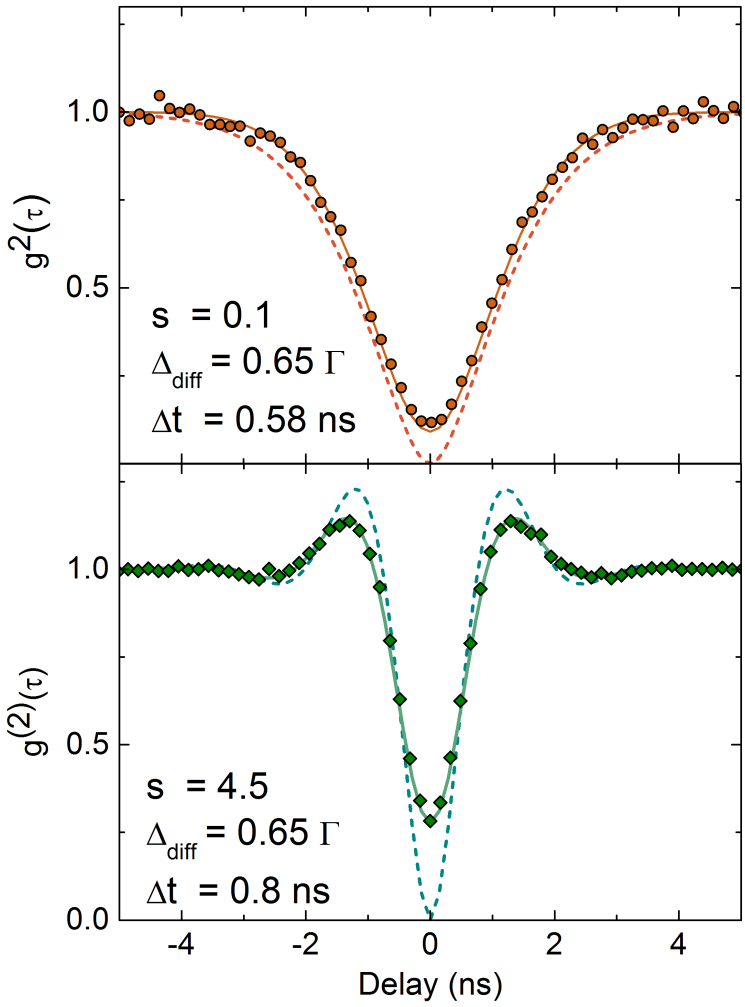

Fig. 3.8 Measured intensity autocorrelation of resonance fluorescence from the neutral exciton transition at driving powers of $s = 0.1$ and $s = 4.5$ shown as orange and green symbols respectively. The solid curve is a simulation with the parameters shown in the legend, where Δ_{diff} is the FWHM of the detuning distribution representing spectral diffusion and Δt is the time FWHM of the instrument response function. The dashed curves are simulations without spectral diffusion and without convolution with the instrument response function.

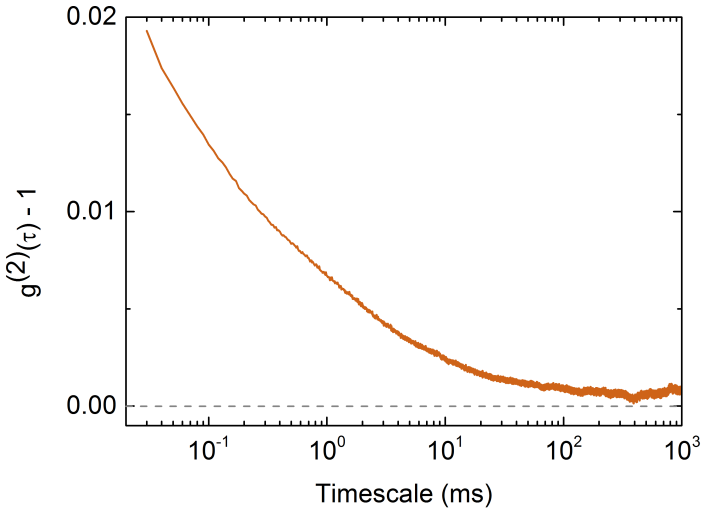

Fig. 3.9 Intensity autocorrelation of resonance fluorescence from the neutral exciton transition at a driving power of $s = 1$ and long delays. Correlations in the RF intensity can be seen as $g^{(2)}(\tau) - 1 > 0$.

environment is still clear in most of these measurements: charge and nuclear spin fluctuations lead to inhomogeneous broadening while phonon coupling gives a homogeneous broadening even at cryogenic temperatures. These effects are generally considered detrimental for the use of quantum dots as either single photon emitters or spin-photon interfaces. In the following chapters, we will add ground state spin into the mix and study these diverse environmental effects in more detail, with a particular focus on using this environment as a resource.

Chapter 4

Phonon-assisted Resonance Fluorescence Frequency Stabilisation

There exist multiple measures to quantify the quality of a single-photon emitter. In many respects, QDs show promise due to their high quantum efficiency, large oscillator strength, and low $g^{(2)}(0)$. Additionally, a lot of progress has been made in the integration of QDs within semiconductor nanostructures [78–80], leading to increased collection efficiencies and the prospect of on-chip architectures. From the perspective of the use of a single quantum emitter for quantum information, one of the most important figures of merit is the indistinguishability of independently emitted photons. Indeed, most quantum information processing protocols rely on interference of two single photons generated independently and a poor indistinguishability is a severe roadblock, e.g., imperfect spectral overlap would limit the entanglement fidelity of two distant QD spins in a distributed quantum network architecture [21]. As we have already briefly touched upon, the solid-state environment leads to inhomogeneous broadening of the exciton transition, thereby reducing the spectral overlap of independently emitted photons. Measurements of QD photon indistinguishability remain limited by environmental noise, even under resonant excitation [36, 81, 82]. Near-unity indistinguishability with QDs can be achieved despite the noisy environment in the regime of coherent single photon emission [37], as the spectrum is dictated by the excitation laser. However, this technique suffers from a low photon emission rate due to the low excitation power required. Furthermore, this method still suffers from the effect of inhomogeneous broadening, in the form of a reduction of emission intensity. If the intensity noise is large enough, this can in turn lead to a lowered two-photon interference visibility [38].

In this chapter, we concentrate on the effects of electric field fluctuations and phonon coupling on the QD resonance fluorescence. We further demonstrate a technique which makes use of the phonon-assisted emission to feedback on the zero-phonon line (ZPL) frequency,

thereby reducing the inhomogeneous broadening without sacrificing ZPL emission. Similar stabilisation protocols have been demonstrated with solid-state quantum emitters, but rely either on periodically scanning across the resonance which limits the bandwidth [41], or require the detection of a significant fraction of the zero-phonon emission to obtain an error signal [40, 42].

The measurements shown in this chapter, published in Ref [83], were taken in collaboration with the rest of the QD team and Carsten H. H. Schulte in particular. This chapter builds up on work done by Megan J. Stanley and Clemens Matthiesen, published in Refs [77, 84], quantifying the timescales and amplitudes of different noise sources in QD RF. In particular, the histogram analysis technique of Ref [84] was used to extract the detuning distribution.

4.1 Electric Field Noise in Quantum Dots

In this chapter we examine the negatively charged trion transition in the absence of an externally applied magnetic field. An example absorption linescan is shown in Fig 4.1 taken over a few seconds. The typical lifetime of the trion excited state in this sample is ≈ 0.7 ns, while the linewidth of the low-power absorption spectrum is 620 MHz, corresponding to almost three times the transform limit. As examined in Refs [73, 77], two physical mechanisms contribute to this inhomogeneous broadening. Firstly, the fluctuating OH field lifts the degeneracy between the ground states, and to a lesser extent the excited states. This random distribution of spin splittings leads to a broadening of the time-averaged absorption linewidth. The coupling to the nuclear spin bath is discussed in more detail in chapter 5 and 6. Secondly, fluctuations in the charge environment of the QD affect the permanent dipole moment of the excited state and consequently alter the transition frequency. Refs [73, 77] show that OH and electric field noise sources occur at different timescales. The OH field fluctuations typically occur on timescales between 10 μs and 100 μs whereas electric field fluctuations show timescales anywhere between 100 μs and ≈ 1 s. These fluctuations can be seen in the time-domain by using a frequency- and power-stabilised single-mode laser, initially tuned on resonance with the X^- transition. Panel B of Fig. 4.1 shows a typical timetrace with an integration time of 100ms. The effect of slow electric field fluctuations on the instantaneous transition frequency can be seen as large RF intensity fluctuations. The amplitude of these fluctuations is large relative to the corresponding shot noise for the same mean count rate, showing that we are far from having an ideal quantum emitter. The motivation behind the work presented in this chapter is then clear: one would like to minimise the effect of inhomogeneous broadening, both to reduce the photon distinguishability as well as improving photon emission rates under resonant excitation.

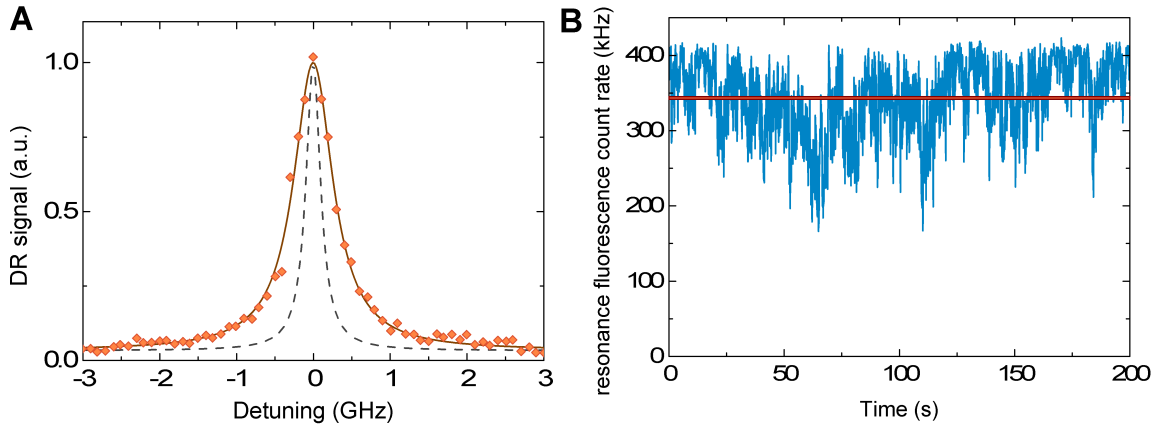

Fig. 4.1 **A.** Low-power differential reflection absorption spectrum (orange diamonds) along with a Voigt fit (brown curve). The best fit FWHM is 620 ± 10 MHz. The dashed curve shows the transform-limited spectrum for a transition with an excited state lifetime of 0.7 ns. **B.** Example resonance fluorescence timetrace (blue curve) for zero initial detuning and an excitation power of $s = 1$. The integration time in this measurement is 100ms. The red rectangle represents $\pm 1\sigma$ for a Poisson distribution with the same mean count rate and integration time.

To see what impact a realistic feedback stabilisation protocol would have, we turn to a more quantitative measurement of the noise timescales in this particular QD. For this, we measure 30 s long timetraces with an integration time of 200μs at an excitation power corresponding to $s = 1$. There exist noise contributions below 200μs, but we know that the gate on our sample has a bandwidth of ≈ 3 kHz, so feedback stabilisation of faster noise sources would be impossible for this sample. Figure 4.2 shows the average noise power spectrum and intensity autocorrelation $g^{(2)}(\tau) - 1$ for 100 such measurements. In this chapter, we use a normalisation such that the integrated power spectral density gives the average intensity variance over 30 s, as follows [73, 85]:

$$N_{\mathrm{QD}}(f) = \frac{(t_{\mathrm{bin}})^2}{T} \left| DFT \left[\frac{N(i)}{< N(i) >} \right] \right|^2 \tag{4.1}$$

where $N(i)$ is the number of counts in the ith bin of width t_{bin}, T is the total measurement time, and we take the Discrete Fourier Transform (DFT). The measurement shows a noise spectral density decreasing with increasing frequency. A general $1/f$-like trend accounts for most of the noise spectral density. The additional frequency dependence is due to the presence of an ensemble of fluctuators [73, 86] representing individual charge traps in the environment, each with its own characteristic timescale describing its charging dynamics. This typically gives a roll-off type spectrum in addition to the $1/f$-like dependence. A similar

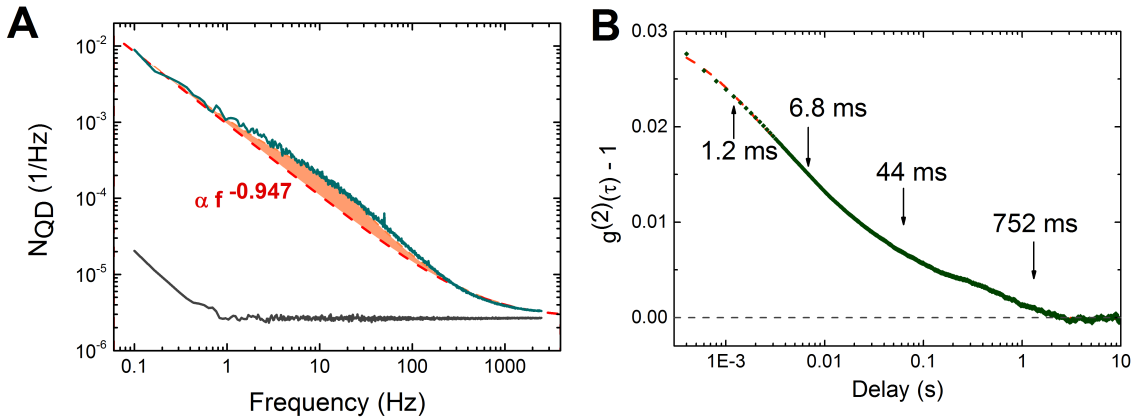

Fig. 4.2 **A.** Average noise spectral density of resonance fluorescence at a driving power of $s = 1$ (green curve). A reference measurement is obtained by un-suppressing the reflected laser (grey curve) such that the mean count rate is comparable with the green curve. The high frequency value corresponds to the noise spectral density due to shot noise. The dashed red curve is a fit to $Af^{-\alpha}$, and the orange shaded area is a similar fit with an added Lorentzian decay of 15Hz FWHM. **B.** Intensity autocorrelation function of resonance fluorescence. The dashed red curve is a multi-exponential fit with decay timescales as shown.

measurement is taken by detuning the QD and unsuppressing the laser reflection such that the mean count rate is the same as the RF measurement. This reference spectrum is flat at frequencies above 1 Hz, and gives an estimate of the contribution of shot noise to the measurement. There is an increase of noise power at low frequencies due to instabilities in the setup, which could be linked to polarisation fluctuations at the output of the PM detection fibre, which are mapped to intensity fluctuations due to the polarisation dependence of the optics used before detection (see next section). At frequencies above ≈ 1 kHz, the RF noise spectral density is of the same order of magnitude as shot noise. This tells us that a frequency stabilisation scheme operating with a bandwidth of 1 kHz would be sufficient to get the RF intensity noise down to the shot-noise level. The presence of individual fluctuators can be seen more clearly in the intensity autocorrelation [77, 87], which is well fit by a multi-exponential decay with four characteristic timescales ranging from 1ms to 1s. Each exponential decay timescale corresponds to a correlation time describing an environmental noise source, e.g. charge traps created by nearby defects [86].

The intensity noise shown in Fig. 4.2 betrays an underlying ZPL frequency fluctuation. There are various ways that this time-averaged detuning distribution can be measured. One possibility is to record RF intensity while scanning the laser frequency across the resonance and building statistics on the central frequency distribution. However, this method is limited both by the experimentally achievable sweep rates and by finite count rates which reduce the

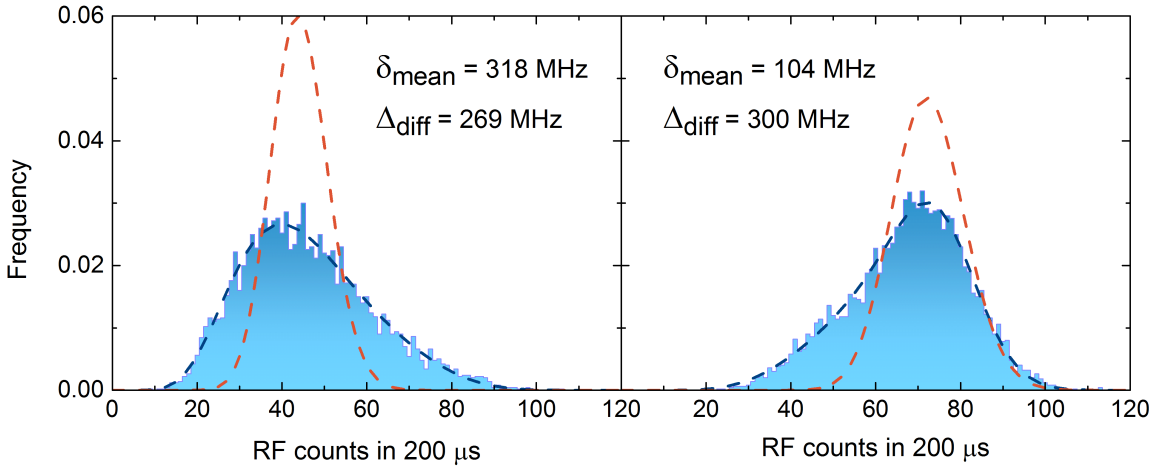

Fig. 4.3 Two example histograms of X^- resonance fluorescence (blue columns), taken for $1s$ long timetraces at $s = 1$ with an integration time of $200\mu s$. The blue dashed curve is a best fit assuming a Gaussian detuning distribution of shot-noise limited histograms. The dashed orange curve is the Poisson distribution corresponding to the same mean count rate.

quality of the peak fitting routine. Another less demanding method, developed by Clemens Matthiesen and Megan J. Stanley [84], is based on fitting the histograms of RF timetraces to a Gaussian detuning distribution of shot-noise limited histograms. For this, we assume that the time-averaged charge state of the environment leads to a Gaussian distribution of central frequencies, and that the measurement time is long enough to sample the entire distribution. From each timetrace, the mean detuning and Gaussian diffusion width can be extracted. Fluctuations faster than the measurement time will appear in the diffusion width, whereas slower fluctuations will lead to a different mean detuning in every subsequent timetrace. Two example histograms of 1 s long timetraces are shown in Fig. 4.3, along with the best fit and the corresponding fit parameters. By performing a χ^2 analysis, we find that the uncertainty on the best fit mean detuning is ≈ 20 MHz. For this QD, we find an average diffusion FWHM of 230 MHz which is on the order of the transform-limited linewidth, which explains the absorption linewidth measured in Fig. 4.1. This inhomogeneous broadening will have a detrimental effect on experiments relying on photonic coalescence from independent QDs [21, 48–50]. A calculation of the distribution of spectral overlaps for two emitter suffering from inhomogeneous broadening is shown in Fig. 4.4. For diffusion widths on the order of the radiative linewidth, the average spectral overlap reduces significantly, which is why Hong-Ou-Mandel type experiments with incoherently generated photons have shown photon indistinguishabilities significantly lower than 1 [36, 81]. Developing a method for reducing

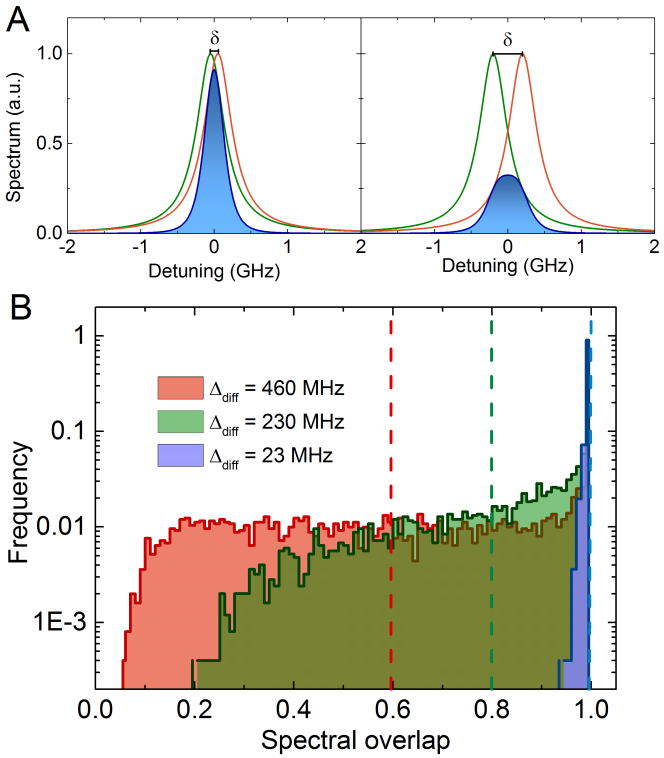

Fig. 4.4 Simulation of the distribution of spectral overlaps for photons emitted by two uncorrelated emitters. **A.** Example of spectral overlap for two emitter with normalised Lorentzian homogeneous spectra (red and green peaks) detuned with respect to the other emitter. The blue shaded region shows the result of multiplication of the spectra of the two emitters, for which the integral is proportional to the spectral overlap. **B.** Calculated distributions of spectral overlaps for 2500 samples of a Gaussian detuning distribution. Δ_{diff} represents the FWHM of the Gaussian distribution. Each spectral overlap is normalised to the integral of the squared homogeneous lineshape. The dashed lines represent the average spectral overlap for each diffusion width.

the diffusion width by an order of magnitude would therefore lead to significant improvement to photon indistinguishability.

This calculation of course assumes that spectral diffusion is the only source of indistinguishability affecting QDs. In the following section, we will discuss a second source of photonic distinguishability: exciton-phonon coupling.

4.2 Phonon Sideband Filtering

The effect of phonon coupling in QDs, due to their low-dimensionality, is qualitatively different from the case of bulk semiconductors. The discrete energy spectrum in QDs prevents direct phonon-mediated energy relaxation, and creates a so-called phonon bottleneck [88]. However, virtual transitions involving phonon absorption or emission still occur and contribute to broadening of the optical transition in QDs [89]. Historically, phonon-induced dephasing in QDs has been observed as a fast decay of the exciton coherence in four-wave mixing [90] and as a temperature-dependent broadening of the emission spectrum [43, 44]. The spectral shape is well reproduced by a model considering a coupling of the exciton to longitudinal-acoustic (LA) phonon modes through the deformation potential [89]. This model predicts three components to the spectrum: a peak at the exciton transition energy associated with the emission of a single photon (zero-phonon line), and blue (red) detuned sidebands associated with absorption (emission) of a single LA phonon. The exact spectral shape is determined by the temperature and the shape of the dot. The size of the dot, and therefore the extent of the exciton wavefunction, determines the lower limit of the wavelength of the coupled phonon modes. High temperatures, meaning high mean phonon numbers in the LA modes, cause an increase in the rate of phonon-assisted processes compared with the zero-phonon radiative decay and a subsequent increase in the spectral linewidth. Fortunately, the coupling rate to low-energy LA phonons tends to zero, and the ZPL itself doesn't suffer from significant dephasing. Several experiments have shown that, after filtering out the PSB, the ZPL shows photon emission with high indistinguishability [36, 37, 81]. Figure 4.5 B shows a resonance fluorescence spectrum at 4K. We find that typically $\approx 90\%$ of emission is in the ZPL (86% for this QD) and the phonon-assisted emission is highly asymmetric about the ZPL. The latter effect reflects the low occupation number of the LA phonon modes, and phonon emission is consequently far more likely than absorption.

By working with such a solid-state emitter, we therefore find that approximately a tenth of the emission intensity has to be thrown away in order to obtain near-unity indistinguishability. The idea behind the stabilisation scheme presented in this chapter is that, instead of discarding the PSB emission, we use it as an secondary channel to measure the instantaneous frequency

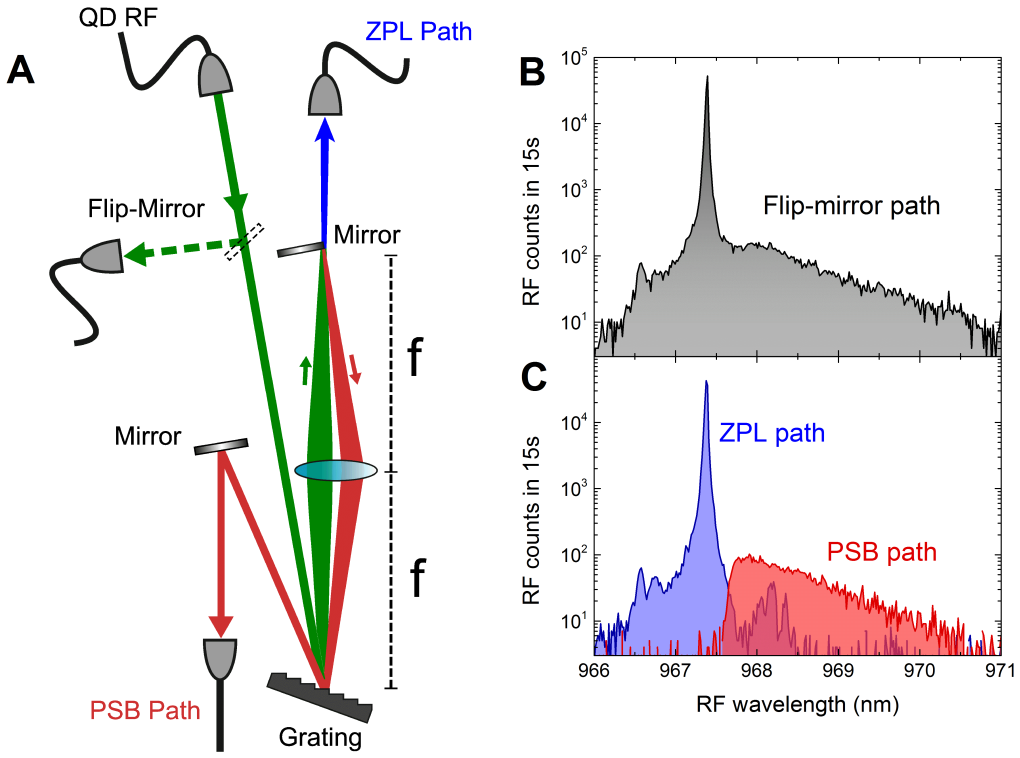

Fig. 4.5 **A.** Schematic diagram of the optical filtering setup used to measure the zero-phonon line (ZPL) and phonon sideband (PSB) of QD resonance fluorescence simultaneously. f describes the focal length of the lens. **B.** Resonance fluorescence spectrum of the X^- transition under an excitation power corresponding to $s = 1$ taken with the flip-mirror stage. **C.** Resonance fluorescence spectra taken through the ZPL (blue curve) and PSB (red curve) paths for the same excitation power and integration time as B.

of the ZPL. This way we can feedback on the transition frequency without needing to sacrifice any of the useful ZPL photons. In order to simultaneously measure both spectral components, we use the setup shown in Fig. 4.5. The phonon sideband peak is only ≈ 1 nm detuned from the ZPL, so we cannot simply use a dichroic mirror or a bandpass filter. Instead, in order to obtain a broadband collection of the PSB we use a 4-f-like setup. QD Resonance fluorescence is dispersed on a 1600 grooves/mm diffraction grating and a lens focuses the different spectral components at different points in the Fourier plane. By using a sharp-edged mirror, we selectively reflect part of the spectrum back onto the grating, where the beam is re-collimated and coupled into a single-mode fibre. The component which is not reflected is coupled into a different single-mode fibre. A flip-mirror can be inserted before the grating in order to measure a reference spectrum. Figure 4.5 C shows spectra of the ZPL and PSB modes under the same excitation condition. The two spectral components are well separated into two spatial modes, although there is some leakage of the PSB emission into the ZPL

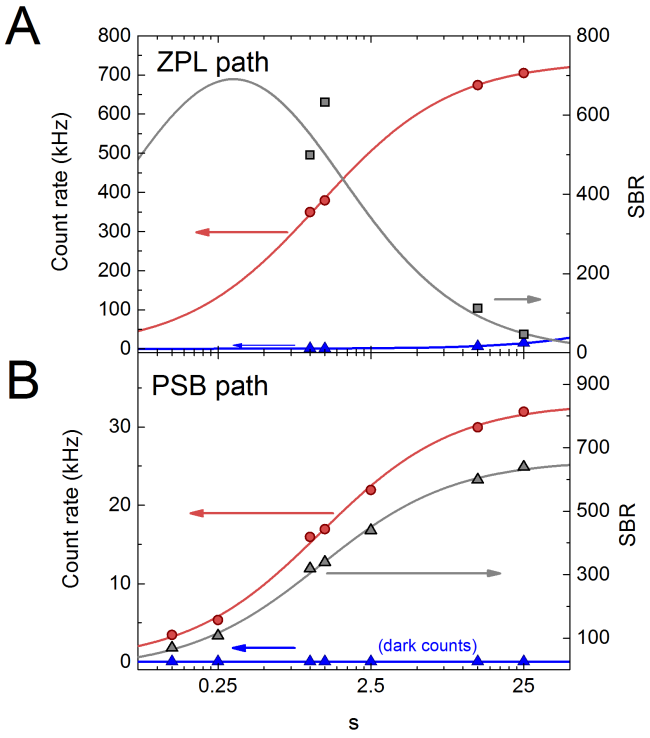

Fig. 4.6 **A.** Photon count rates with the ZPL path coupled to an APD, with the laser on resonance (red circles) and off resonance (blue triangles). The Signal-to-Background Ratio (SBR) is plotted as gray squares. The red curve is a fit to the standard two-level saturation behaviour, the blue curve is a linear fit, and the gray curve is the ratio of the two fits. **B.** Similar measurement to A, but with the PSB path coupled to the same APD. The blue line is flat, and the background is solely limited to the dark count rate of the APD of ≈ 50 Hz.

mode, probably due to scattering at the mirror edge. The peak count rate of the ZPL mode is $\approx 85\%$ that of the reference spectrum taken through the flip-mirror path. This loss is mainly due to the efficiency of the grating ($\approx 90\%$ for linearly polarised light) as well as finite transmission of the other optics. The peak PSB count rate is $\approx 60\%$ compared with the reference spectrum count rate at the same wavelength. This efficiency is lower due to the PSB beam double-passing the grating. Figure 4.6 shows count rates for the two modes, measured with the same avalanche photodiode. We measure around 4% of the ZPL count rate with the PSB mode, giving 17 kHz at a driving power of $s = 1$. For a wide range of powers, the signal to background ratio (SBR) is significantly higher than 100, as there is very little cross-talk between the two modes and therefore no laser background in the PSB mode. For all the powers shown here, the SBR is limited by the dark count rate of the APD. For the

ZPL mode the background is limited by imperfect polarisation suppression of the reflected laser.

Is this count rate high enough to stabilise against the noise described in the previous section? A rough estimate of the stabilisation bandwidth that the PSB mode would give can be obtained by considering the time needed to differentiate between the QD being on resonance and being detuned by a certain amount. From Fig. 4.6, driving at $s = 1$ we obtain a PSB count rate of 17 kHz on resonance. For the detuned PSB count rate, we assume a mean detuning equal to that of Fig. 4.1, where $I_{\max} = 416$ kHz and $I_{\text{mean}} = 343$ kHz. The detuned PSB count rate would then be $\frac{I_{\text{mean}}}{I_{\max}}.17$ kHz. The integration time needed for the difference between these two signals to be equal to shot-noise is around 2 ms. In practice the bandwidth will depend on the experimental implementation, but in principle the PSB count rates shown here should be sufficient to deal with most electric field noise sources for this QD.

4.3 Feedback Stabilisation Technique

Figure 4.7 shows the experimental setup used to convert the PSB channel into an error signal for feedback stabilisation of the ZPL frequency. A single mode laser, which is frequency-stabilised to ± 5 MHz and power-stabilised to $\pm 1\%$, is used to resonantly excite the trion transition at a driving power corresponding to $s = 1$. The resonance fluorescence is sent through the filtering setup and both the ZPL and PSB paths are coupled to separate APDs. The ZPL channel is used for characterisation and plays no further part in the stabilisation protocol. A simple measurement of the count rate from the PSB APD can give us information about the mean detuning from resonance but cannot distinguish between positive and negative detunings. For this we use a function generator to apply a small-amplitude modulation of the gate voltage. This modulation will be mapped onto the PSB signal, the phase of which gives the sign of the detuning. We demodulate the PSB signal with a lock-in amplifier to obtain a detuning-dependent error signal (shown in Fig. 4.8 B for a lock-in gain of 80 dB a modulation of 1.5 kHz and time constant of 1 ms) which can be used as input of a PID controller. The output $u(t)$ of a PID controller is related to the error signal $\varepsilon(t)$, defined as the difference between the measured value and the setpoint, as follows:

$$u(t) = \mathrm{P}.\varepsilon(t) + \mathrm{I}\int_0^t \varepsilon(t)\mathrm{d}\tau + \mathrm{D}\frac{\mathrm{d}\varepsilon(t)}{\mathrm{d}t} \tag{4.2}$$

Here D is not used as it can sometimes lead to amplification of high frequency noise, P and I are optimised by minimising the intensity variance after stabilisation. The output of the PI controller is fed back as a DC correction to the gate voltage. The modulation used here

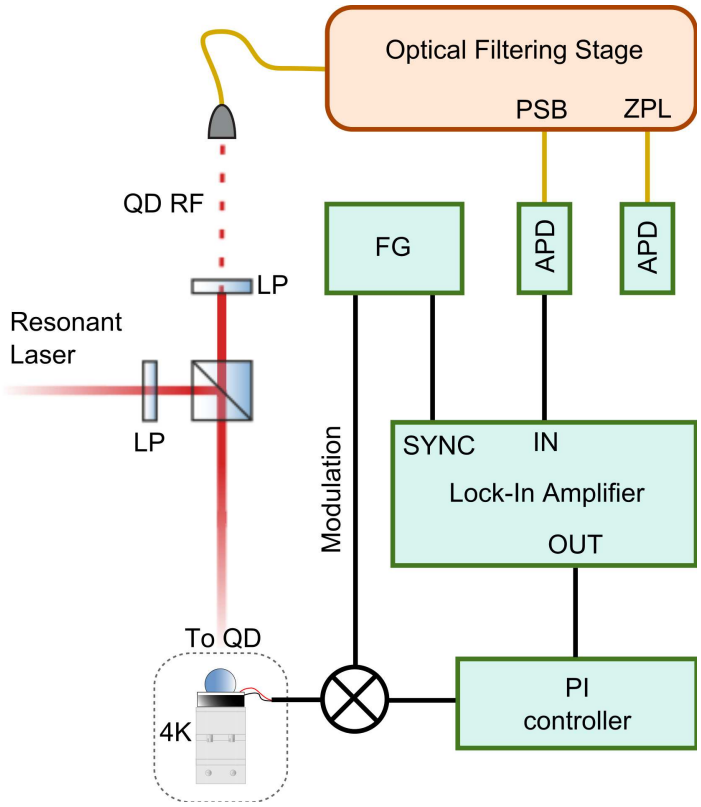

Fig. 4.7 Diagram of the feedback stabilisation scheme. We use a confocal microscope with polarisation rejection of the excitation laser to collect QD resonance fluorescence. The optical filtering stage is the one described in Fig. 4.5. LP: linear polariser, APD: avalanche photodiode, and FG: function generator.

is ≈ 0.5 mV corresponding to a modulation of the ZPL central frequency of ≈ 150 MHz in linear frequency. The absorption spectrum is consequently broadened from 620 ± 10 MHz to 760 ± 10 MHz. This unfortunately leads to a drop in peak count rate, but corresponds to a decrease of only 3% for this modulation amplitude. Figure 4.8 B shows that the error signal goes as the derivative of the lineshape, as the modulation amplitude is small compared with the linewidth. From panels C and D, we see that stabilisation beyond 1kHz will not be possible, both because the signal-to-noise ratio (SNR) drops below unity for integration times lower than 1 ms and because we are limited by the bandwidth of the Schottky diode. Higher stabilisation bandwidths may be obtained by increasing the modulation amplitude, at the price of lowering the peak ZPL count rate, but would also necessitate a device with a faster gate.

4.4 Stabilisation Results

We now turn to a characterisation of the stabilisation protocol, by comparing the intensity and frequency noise characteristics of the ZPL channel with and without stabilisation. For an appropriate 'unstabilised' comparison, a reference measurement is taken with no feedback or modulation applied to the gate voltage. All measurements shown in this section are taken at a driving power of $s = 1$ for a QD initially set to be on resonance.

4.4.1 ZPL Intensity Fluctuations

As a first characterisation step, we look at the difference in ZPL intensity noise between stabilised and unstabilised measurements. Figure 4.9 shows a relatively long (2000 s) measurement with an integration time of 100 ms. This experiment is thus sensitive only to the $1/f$-like component of noise, which appears as slow and high amplitude fluctuations in intensity. These are apparent in the unstabilised case (green curve) where the intensity drops almost by half at certain points throughout the measurement, and the stabilisation protocol (orange curve) shows suppression of this slow noise. Due to the gate voltage modulation, the stabilised curve shows a peak count rate $\approx 3\%$ lower than the unstabilised case. However, for long measurements, suppression of $1/f$-like noise leads to an increase of mean count rates by 7.3%.

For a comparison of the faster noise characteristics, we measure 100 ZPL resonance fluorescence time traces of 30 s length and 200 μs integration time. The noise spectral densities for stabilised and unstabilised cases are shown in Fig. 4.10, after subtraction of a reference measurement taken with laser reflection. A significant improvement is seen with

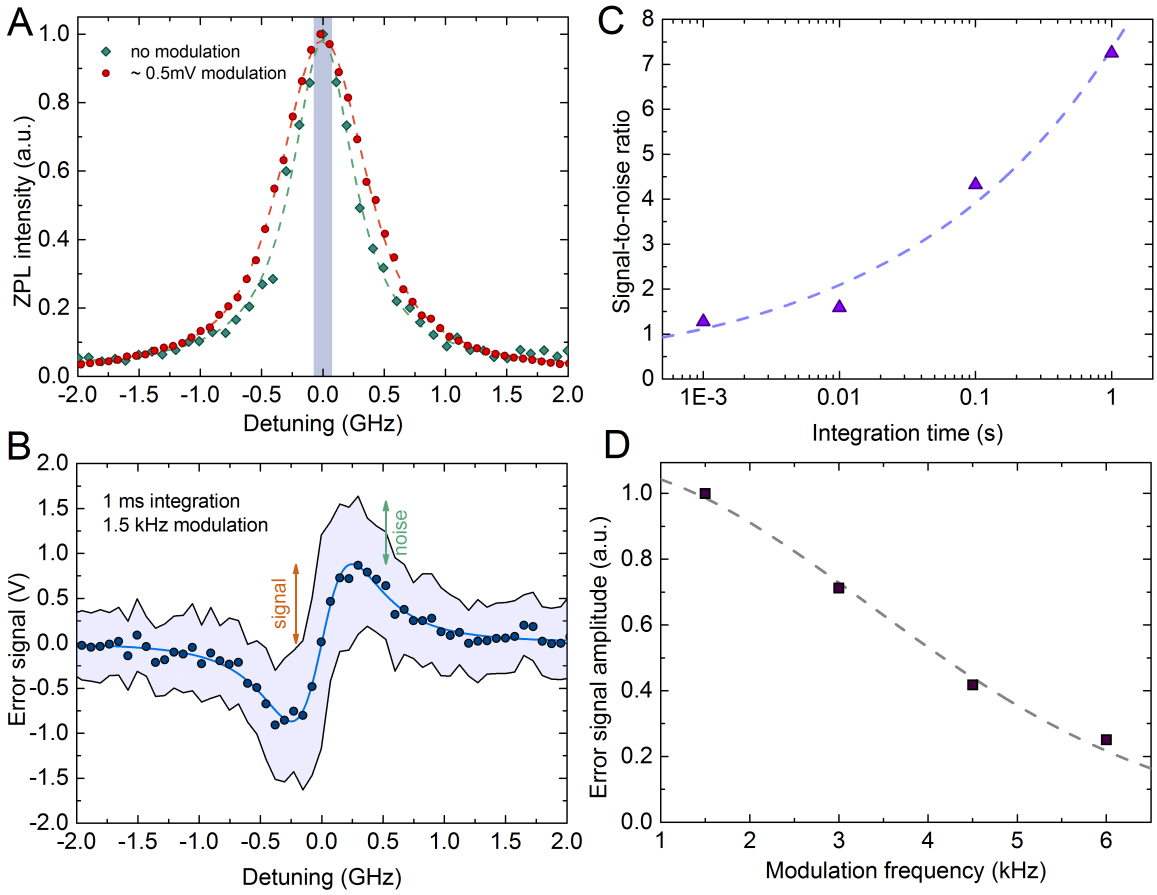

Fig. 4.8 **A.** Normalised absorption spectra with (red circles) and without (green diamonds) gate modulation and a driving power of $s = 1$. The curves are fits to Voigt profiles. The gray bar represents the amplitude of the modulation in linear frequency. **B.** Mean error signal obtained at the output of the lock-in amplifier (blue circles) with $\pm 1\sigma$ shown as a shaded region. The blue curve shows a fit to the derivative of a Lorentzian profile. **C.** Signal-to-noise ratio (purple triangles) as a function of lock-in time constant for a modulation at 1.5 kHz. The dashed curve is a fit to a power law with best fit exponent of 0.27 ± 0.04. **D.** Amplitude of the error signal (purple squares) as a function of modulation frequency for a fixed time constant of 1 ms and a fixed modulation amplitude. The gray curve is a fit to a Gaussian decay and serves as a guide to the eye.

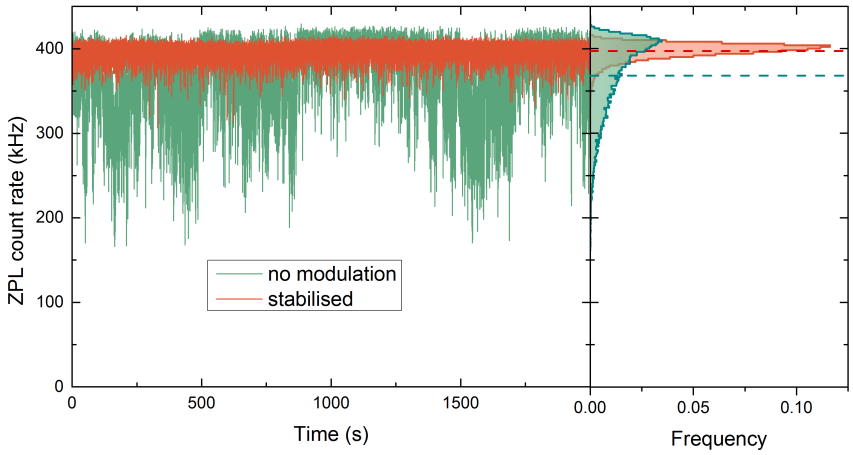

Fig. 4.9 Timetraces of resonance fluorescence for an initial condition of zero detuning. The integration time is 100 ms and the driving power corresponds to $s = 1$. The green (orange) trace is the measurement without (with) modulation and stabilisation. The right panel is the corresponding histogram over the entire measurement time. The dashed lines represent the mean count rate which is 370 kHz for the unmodulated measurement and 397 kHz with stabilisation.

stabilisation, particularly in the low frequency region where the noise power is reduced by more than 2 orders of magnitude. The additional peaks in the stabilised spectrum arise from the gate modulation at 1.5 kHz and extra noise due to the PI electronics. From the perspective of using this stabilisation scheme to improve photonic coalescence between independent QDs, the added noise at the modulation frequency is not necessarily limiting, as the same function generator can be used to drive both QDs in phase. With the normalisation of equation 4.1, the integrated power spectral density gives the average variance in ZPL intensity over 30s. For the unstabilised case this gives a variance 44 times higher than the corresponding shot-noise (estimated with the laser reference measurement), whereas with stabilisation it is only twice shot-noise. Of course, this comparison with shot noise is slightly arbitrary in the sense that the result depends on experimental parameters such as collection and detection efficiency. However, we can see that the noise contribution due to electric field fluctuations is reduced by a factor of 22. A more complete characterisation of the stabilisation would require an estimate of the bandwidth of stabilisation which can be compared with the electric field noise characteristics. Fig. 4.10 shows an improvement in intensity noise up to ≈ 1 kHz. However, the interpretation of this improvement at high frequencies is not trivial, due to the detuning dependence of electric field noise. As demonstrated in [73, 77], the sensitivity to electric field noise varies as the derivative of the homogeneous lineshape and therefore has a local minimum at zero detuning. Thus, by suppressing the slow frequency fluctuations, the mean

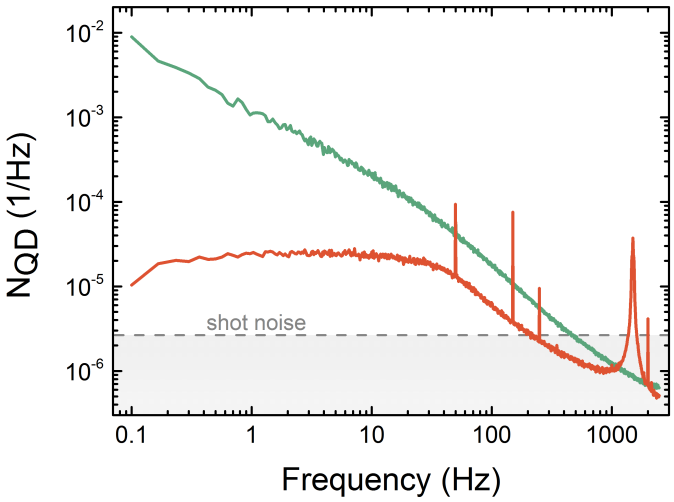

Fig. 4.10 Average noise spectral density of 30 s long resonance fluorescence time traces with an integration time of 200 μs where the measurement with (without) stabilisation is shown in orange (green). The broad peak in the stabilised spectrum corresponds to the applied gate modulation frequency of 1.5 kHz, and other peaks are caused by the introduction of additional noisy electronics. A reference spectrum, taken with unsuppressed laser with a similar mean count rate, is subtracted to obtain both curves. The gray dashed curve shows the shot-noise level for a measurement at comparable count rate.

detuning is reduced along with the sensitivity to electric field noise. This explains why the noise spectral power is lower in the stabilised case even for frequencies above the modulation frequency, which cannot correspond to a stabilisation bandwidth.

4.4.2 Stabilization Bandwidth

Obtaining a stabilisation bandwidth from a noise spectrum is not simple due to the confounding factor of detuning dependent noise sensitivity. As explained earlier, the intensity autocorrelation gives us information about the distinct fluctuation timescales corresponding to individual fluctuators. With no stabilisation we find that a multi-exponential decay with four characteristic timescales (1.2, 6.8, 44, and 752 ms) fits the data well. Our stabilisation scheme corrects the emission frequency of the QD, but as the corrections to the electric field required are small, we assume that our stabilisation scheme does not affect the inherent charge dynamics in the environment. Therefore, we can use the knowledge of the charge dynamics to see the effect of the stabilisation at each timescale. Figure 4.11 A shows the intensity autocorrelation with and without stabilisation. We fit the stabilised curve with a multi-exponential decay with the same timescales as the unstabilised case. An extra decaying oscillation at 1.5 kHz is included to model the gate modulation. The ratio of best fit amplitude with and without stabilisation at the same timescale ('Noise contribution ratio') is plotted in panel C and shows a complete suppression of the two slowest timescales. The fact that each timescale is reduced by a different factor is a first indication that the improvement is not solely due to a lower sensitivity. For a more precise estimate of the bandwidth we can look at the decay timescale of the oscillations in the autocorrelation. This decay is linked to the acquisition of an error signal and subsequent compensation, and its timescale therefore quantifies the bandwidth of the stabilisation. To motivate this interpretation, a similar measurement for higher value of P is shown in panel B. A revival of the oscillations is seen along with a phase flip, due to the feedback overshooting the setpoint because P is too high. This is a common problem with PID control systems, and the data shown here are with optimised values of P and I. The best fit to the decay of oscillations in the orange curve gives a stabilisation bandwidth of 191 ± 4 Hz. This is comparable to the fastest electric field fluctuations in the sample and should lead to a significant reduction in the inhomogeneous width of the ZPL. A modest improvement of the collection or detection efficiency would allow the complete suppression of electric field noise for this QD. This could be achieved by embedding the QD in an optimised dielectric structure [91–93], combined with a structure allowing faster gate control[94, 95]. In principle, with near-unity collection and detection efficiencies, PSB count rates could allow for partial feedback correction of nuclear spin fluctuations. However, reaching these timescales would require vast technical improvements.

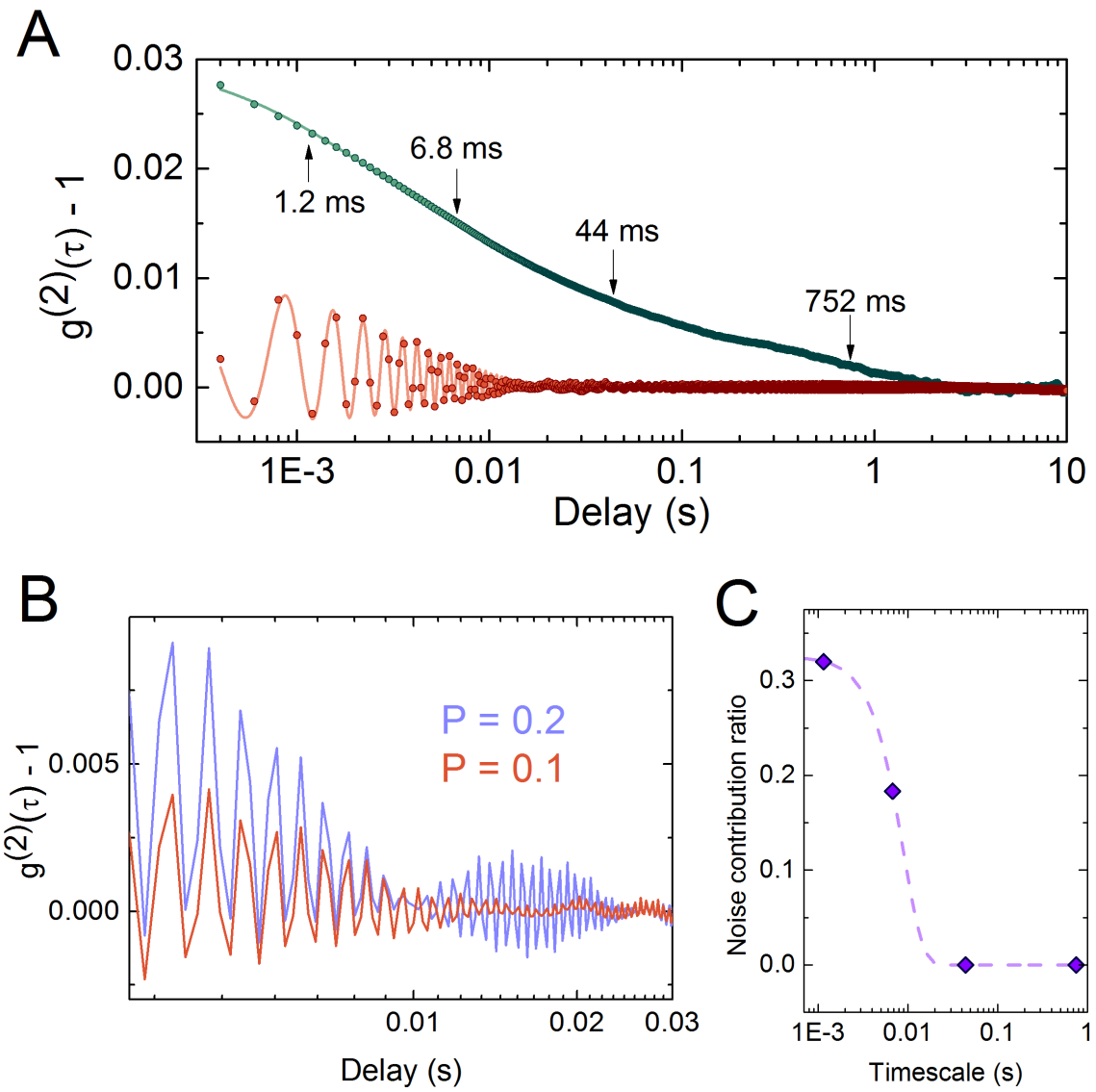

Fig. 4.11 **A.** Intensity autocorrelation of 30 s long resonance fluorescence timetraces with an integration time of 200μs. The green circles are the same data as Fig.4.3 taken with no stabilisation. The orange circles show the stabilised measurement with optimised values of P and I. The oscillations at 1.5 kHz are caused by the gate voltage modulation. The solid curves are multi-exponential fits with the decay timescales shown. The fit to the orange data further includes a decaying sinusoid component to fit the oscillations. **B.** Two stabilised autocorrelation measurements for two values of P. A revival of oscillations can be seen for higher P along with a phase flip. **C.** Ratio of the best fit decay amplitudes extracted from **A** at the four timescales after and before stabilisation. A value of zero indicates that noise at that timescale is completely suppressed. The dashed curve is a Gaussian fit serving as a guide to the eye.

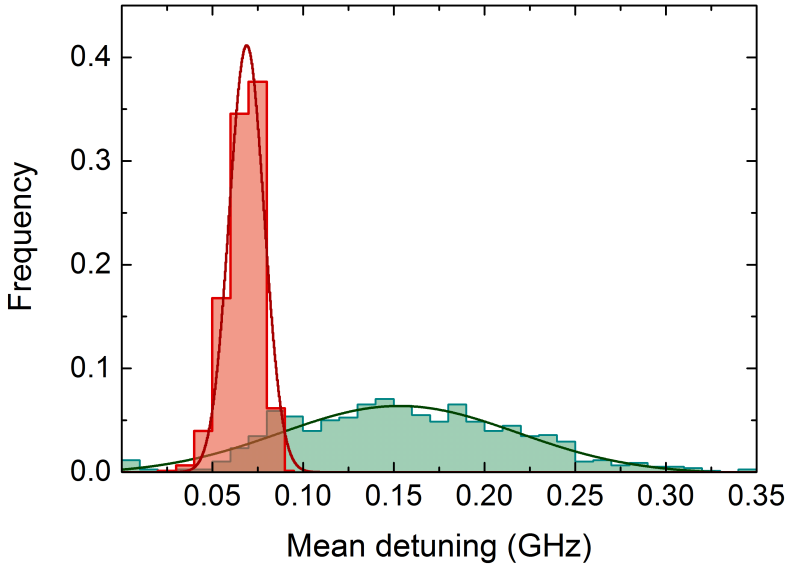

Fig. 4.12 Distribution of central frequencies with (without) stabilisation shown as an orange (green) histogram. The central frequency is extracted from histogram analyses of 781 measurements of 1 s long timetraces. The curves are Gaussian fits with 23 MHz and 154 MHz FWHM for the stabilised and unstabilised measurements respectively.

4.4.3 Inhomogeneous Broadening

The decrease in intensity noise shown above is encouraging, but a more useful figure of merit, in terms of the use of QDs as sources of on-demand indistinguishable single photons, would be the corresponding time-averaged frequency distributions. As described in section 4.1, we record a large number of 1 s long timetraces with an integration time of 200μs with and without stabilisation and perform a histogram analysis to extract the mean detunings for each histogram. The distribution of this fit parameter over 781 measurements is shown in Fig. 4.12. In the stabilised case, we fit to a sum of two Gaussian detuning distributions separated by the modulation amplitude (150 MHz in QD frequency) in order to model the square-wave gate modulation. The distribution for the stabilised data is centered at 70 MHz corresponding to half the modulation amplitude, and it is $\approx$ 150 MHz for the unstabilised case as the QD drifted off resonance throughout the measurement. From the Gaussian fits, we find that the distribution FWHM decreases from 154 MHz to 23 MHz with the stabilisation scheme. By performing a χ^2 analysis on the fitting routine, we estimate that the standard error on the best fit is 23 MHz. Therefore, the measured stabilised frequency distribution is limited by the fitting routine and is likely to be significantly narrower. Sub-Hz frequency fluctuations are therefore suppressed to the extent that they can no longer be resolved.

Chapter 5

Hyperfine Effects in Resonance Fluorescence

An electron spin confined to a QD shows promise as an efficient spin-photon interface, and as such is a strong candidate for an optically-addressable stationary qubit forming the basis of an optical quantum information processor. However, the coupling of this spin degree of freedom to a mesoscopic nuclear spin bath is an important consideration. Random fluctuations of the nuclear spin bath lead to uncertainty in the electron Zeeman splitting and consequently to spin dephasing. This hyperfine coupling in QDs has drawn a large part of the community's focus in recent years [27, 34], both as a central challenge to future QD application and as a fundamental realisation of the central spin problem. We concentrate here on the low-magnetic field regime, where hyperfine effects are obscured by the broad radiative linewidth of QDs.

In this chapter, we present measurements of X^- resonance fluorescence emission spectra and intensity autocorrelations. First, we will show that optically-induced electron spin pumping persists down to zero applied field showing that the hyperfine interaction lifts the spin degeneracy and provides a quantisation axis for the electron spin. This zero-field quantisation affects both the spin-splitting as well as the optical selection rules, changing from Voigt-like to Faraday-like depending on the orientation of the effective magnetic field. Both of these effects are seen in low-power emission spectra, revealing coherent Raman transitions in the Lambda-system created by the Overhauser field. The low-power regime of resonance fluorescence is a key tool, enabling spectroscopy with a resolution below the radiative linewidth. The measured spectra contain information on the nuclear spin bath, and provide a direct measurement of the time-averaged distribution of magnitudes and orientations of the Overhauser field. In the final part of the chapter, we explore the effect of a small external magnetic field on the emission spectra and provide high-resolution measurements of subsequent nuclear spin polarisation and anisotropic nuclear spin distributions.

The intensity autocorrelation data shown here and their subsequent analysis are based on data published in reference [96]. The results shown here were obtained in collaboration with the rest of the QD team, in particular Carsten Schulte and Claire Le Gall who helped coax the temperamental FP cavity into shape in order to take these measurements. The data of Fig. 5.12, 5.10 and the neutral exciton data in Fig. 5.7 were taken by Clemens Matthiesen and are shown with his permission.

5.1 Mean-field Approach to the Hyperfine Interaction

We are working here with the X^- trion transition between a single conduction band electron in the ground state and the lowest energy trion as the excited state. The level structure assumed for the theoretical modeling is shown in Fig. 5.1. At zero external magnetic field, there is no Zeeman splitting of the states, but the spin eigenstates are still in general non-degenerate due to the hyperfine interaction with the nuclear spin bath. The ground state manifold of the charge complex is composed of two orthogonal non-degenerate electron spin states and the excited state is composed of an electron spin singlet and a heavy hole. The electron spin singlet does not contribute to the excited state splitting, which is therefore determined by the heavy hole hyperfine interaction. In general, the hyperfine interaction between spin S and nuclear spin I can be decomposed into three contributions: the Fermi contact hyperfine interaction ($\delta(\mathbf{r})\mathbf{S}.\mathbf{I}$ form), the dipole-dipole interaction ($[(\mathbf{r}.\mathbf{S})(\mathbf{r}.\mathbf{I})] - \mathbf{S}.\mathbf{I}$ form) and the coupling to the orbital angular momentum ($\mathbf{L}.\mathbf{I}$ form) [97, 98]. The symmetry of the carrier wavefunction determines which of these contributes most to the strength of the interaction. For s-type wavefunctions, such as the conduction band electron in the ground state, the Fermi contact interaction dominates and leads to an isotropic interaction with a strength proportional to the electron wavefunction at the nucleus position. This interaction can be written as follows:

$$\hat{H}_{\mathrm{FC}} = v_0 \sum_j A^j \left|\psi(\mathbf{r}_j)\right|^2 \left(\hat{I}_z^j \hat{S}_z + \frac{\hat{I}_+^j \hat{S}_- + \hat{I}_-^j \hat{S}_+}{2}\right) \tag{5.1}$$

where v_0 is the two atom cell volume, A^j is the hyperfine constant of nucleus j with $\mathbf{r}_j$ its position, $\psi(\mathbf{r})$ is the electron wavefunction. The first term within the brackets has an effect similar to that of an external magnetic field which splits the electron spin states. Here, z represents the quantisation axis of the electron spin, which is determined by both the applied field and the instantaneous nuclear spin state. Considering the $\mathcal{O}(10^5)$ nuclei within the electronic wavefunction, we take the mean field approach. We define the resulting effective

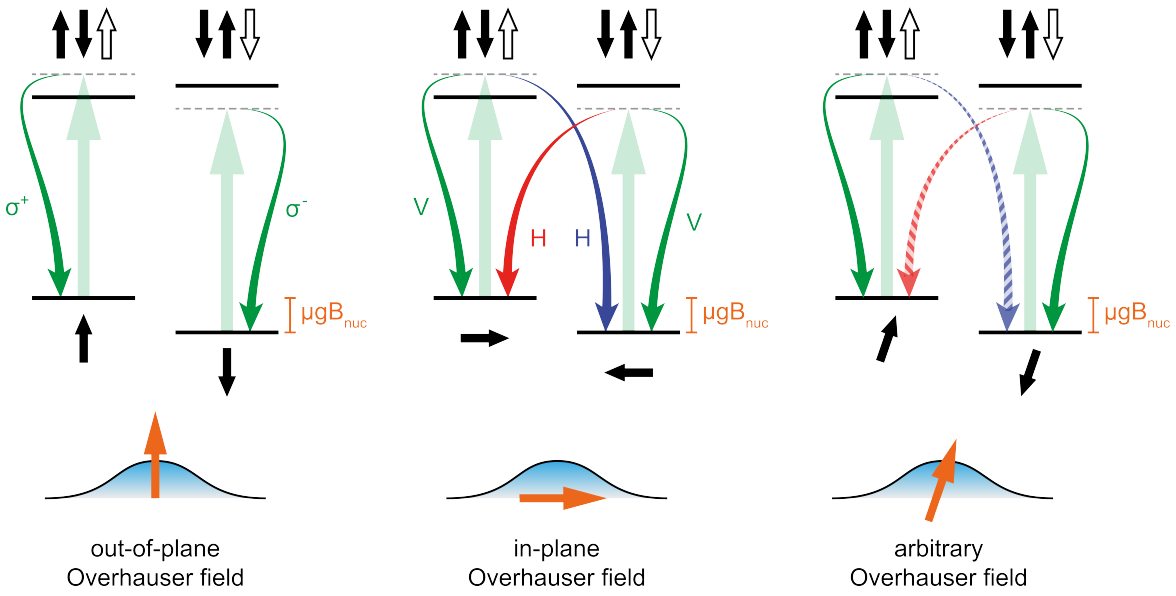

Fig. 5.1 X^- Level structure in the absence of an external magnetic field, for different orientation of the OH field (orange arrow). The straight green arrow represents the linearly polarised driving field, and the curved arrows represent dipole allowed elastic and inelastic transitions. Filled black arrows represent a conduction band electron spin, and hollow arrows represent a valence band hole pseudo-spin.

magnetic field affecting the electron, the Overhauser (OH) field [27], as follows:

$$B_{\mathrm{N}} = \frac{v_0}{\mu_B g_e} \sum_j A^j \left|\psi(\mathbf{r}_j)\right|^2 \left\langle \hat{I}^j \right\rangle \tag{5.2}$$

where μ_B is the Bohr magneton, g_e is the isotropic electron g-factor, and B_N is the effective nuclear magnetic field. The mean field picture then leads to a frozen Zeeman-like splitting. The dynamics of the system are given by the second term in the brackets of equation 5.1, which leads to the exchange of spin angular momentum between the confined electron and the individual nuclei. This term results in electron spin relaxation, as well as the possibility of polarising the spin ensemble by exciting the dot circularly and transferring the resulting electron polarisation to the nuclei via flip-flop [99].

The excited state hyperfine interaction is determined by the heavy-hole spin. The valence band has mainly p-type symmetry [100] and the hole has no overlap with the nuclei, therefore suppressing the Fermi contact interaction. The dipole-dipole form of the hyperfine interaction dominates, but its strength has been measured to be an order of magnitude smaller than the electron hyperfine coupling [101, 102]. For this reason, we neglect the hyperfine interaction in the excited states in this chapter. The confinement is strongest in the z-direction, leading

to a splitting of heavy and light hole bands, which we take to provide a hole spin quantisation axis along the z-direction in the absence of hyperfine splitting.

The strong confinement of the electron wavefunction means that the electron spin samples a relatively small ensemble of nuclear spins. Therefore, a random distribution of nuclear spin orientations in the QD is not averaged to zero, and the OH field generally has a finite dispersion proportional to $1/\sqrt{N}$, where N is the number of nuclei contained within the electron wavefunction. We treat fluctuations in the nuclear spin bath as a random walk of the magnitude and orientation of the OH field. As the electron hyperfine interaction is isotropic, we treat the x, y and z components of the OH field as independent. In the absence of nuclear spin polarisation, each OH field component follows a Gaussian distribution centered at zero with equal dispersions. The magnitude of the OH field determines the electron spin splitting. Additionally, The electron spin quantisation axis follows the OH field, and the selection rules fluctuate accordingly as shown in Fig. 5.1. On the one hand, for an OH field aligned along the optical axis the selection rules are the same as those obtained in the Faraday geometry, giving two circularly polarised transitions with a small branching ratio for the spin-flip transitions. On the other hand, an in-plane OH field gives Voigt-like selection rules with equal contribution of spin-conserving and spin-flipping transitions. In a time-averaged measurement, with the OH field free to evolve in three dimensions, we expect selection rules somewhere in between these two limiting cases, with an additional broadening of the ground state splitting. Under low power resonant excitation, this should lead to the observation of coherent elastic (Rayleigh) as well as inelastic (Raman) contributions to the fluorescence emission spectrum. Both coherent Raman and Rayleigh transitions occur via a virtual level, but the linewidth of the former will be broadened by the dispersion of the OH field distribution, whereas the latter will have coherence properties determined by the driving laser.

The basis and notation used in the calculation is the following: $|1\rangle = |\downarrow\rangle, |2\rangle = |\uparrow\rangle, |3\rangle = |\downarrow\uparrow\Downarrow\rangle, |4\rangle = |\uparrow\downarrow\Uparrow\rangle$, where single arrows represent electron spin states and double arrows represent heavy hole pseudo-spin states.The component of the Hamiltonian representing the Fermi coupling, $\hat{H}_{\mathrm{FC}}$, can be represented as follows in the $\{|0\rangle, |1\rangle\}$ basis for the ground state:

$$\begin{aligned}\hat{H}_{\mathrm{FC}} =& \frac{\mu_B g_e}{2} \mathbf{B_N}.\sigma \\ =& \frac{\mu_B g_e}{2} \left(B_X.\hat{\sigma}_X + B_Y.\hat{\sigma}_Y + B_Z.\hat{\sigma}_Z\right) \\ =& \frac{\mu_B g_e}{2} |B_N| \left(\cos(\theta)\hat{\sigma}_Z + \sin(\theta)\left(e^{i\phi}\hat{\sigma}_+ + e^{-i\phi}\hat{\sigma}_-\right)\right)\end{aligned} \tag{5.3}$$

where the $\hat{\sigma}_\mu$ operators are the usual Pauli spin operators for the ground states. θ and ϕ are the polar and azimuthal angles relative to the optical axis, respectively. The quantum dot is additionally coupled to a classical oscillating linearly polarised electric field describing the excitation laser, which is approximately resonant with both dipole allowed trion transitions ($1 \rightarrow 3$, and $2 \rightarrow 4$). In the dipole and rotating wave approximations, this component of the Hamiltonian, $\hat{H}_{\text{rad}}$, can be written as follows:

$$\begin{aligned}\hat{H}_{\text{rad}} =& -\left(\mathbf{D}_{1,3}+\mathbf{D}_{2,4}\right).\mathbf{E} \\ =& \Omega_{1,3}\left(\sigma_{31}e^{-i\omega_l t}+c.c\right)+\Omega_{2,4}\left(\sigma_{42}e^{-i\omega_l t}+c.c\right)\end{aligned} \tag{5.4}$$

where $\mathbf{D}_{i,j} = \mu_{i,j}\sigma_{ij} + \mu_{j,i}\sigma_{ji}$ is the dipole operator of the transition $i \rightarrow j$, $\sigma_{ij} = |i\rangle\langle j|$ in our previously defined basis, $\Omega_{i,j}$ is the Rabi frequency (taken to be real) and $\mu_{i,j}$ is the dipole matrix element describing transition $i \rightarrow j$. ω_l is the laser angular frequency. The total Hamiltonian of the system can then be written:

$$\hat{H} = \hat{H}_{\text{FC}} + \hat{H}_{\text{rad}} + \sum_{i=3}^{4} \hbar\omega_{\text{T}}\sigma_{ii} + \hat{H}_{\text{Zeeman}} \tag{5.5}$$

where the third term describes the degenerate excited state energy, and the fourth term describes the Zeeman splitting due to an external field in the Faraday geometry. In matrix form this gives:

$$\hat{H} = \begin{pmatrix} \frac{\mu_B g_e}{2}\left(|B_N|\cos(\theta)+B_{\text{Z}}\right) & \frac{\mu_B g_e}{2}|B_N|\sin(\theta)e^{-i\phi} & \frac{\hbar}{2}\Omega_{1,3}e^{i\omega_l t} & 0 \\ \frac{\mu_B g_e}{2}|B_N|\sin(\theta)e^{i\phi} & -\frac{\mu_B g_e}{2}\left(|B_N|\cos(\theta)+B_{\text{Z}}\right) & 0 & \frac{\hbar}{2}\Omega_{2,4}e^{i\omega_l t} \\ \frac{\hbar}{2}\Omega_{1,3}e^{-i\omega_l t} & 0 & \hbar\omega_T + \frac{\mu_B g_h}{2}B_Z & 0 \\ 0 & \frac{\hbar}{2}\Omega_{2,4}e^{-i\omega_l t} & 0 & \hbar\omega_T - \frac{\mu_B g_h}{2}B_Z \end{pmatrix}$$

where g_h is the hole pseudo-spin g-factor in the $\hat{z}$ direction, and B_Z is the magnitude of the applied magnetic field. We can then use the methods described in chapter 2 to calculate the second order correlation function for the trion system. The methods used for the calculation of the emission spectrum are shown in the section 5.3.2.

Most of the data shown in this chapter were obtained with a single QD (nicknamed 'Felix'). In order to simulate the data, a few parameters are needed, namely: the radiative decay rate, the distribution describing the spectral wandering, and the electron and hole g-factors. The first is obtained with a pulsed measurement. The excitation laser is passed through a high-bandwidth electro-optic amplitude modulator. Voltage pulses longer than the radiative lifetime are sent to the EOM, and the subsequent time-resolved RF is recorded. By subtraction of a reference time-resolved measurement with unsuppressed laser at a

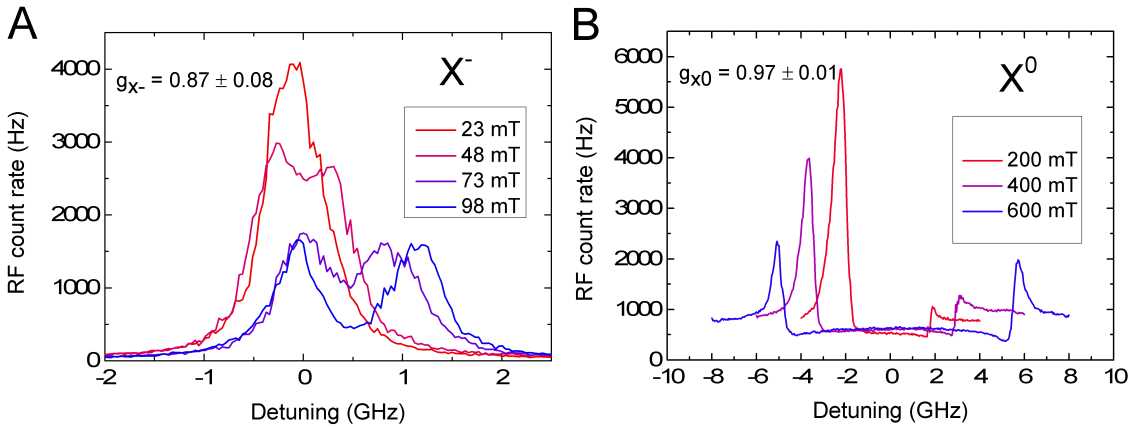

Fig. 5.2 Magnetic field-dependent absorption spectroscopy with a negatively charged QD (**A**) and a neutral QD (**B**). The QD is driven below saturation with a linearly polarised laser. We fit all curves to a sum a two Voigt peaks and extract the frequency difference to obtain the Zeeman splitting. The extracted g-factors for X^0 and X^- are shown inset. The X^0 measurement shows a dispersive component due to interference of the QD RF with the laser background.

comparable count rate, we are able to obtain a decay in RF once the driving laser is switched off, giving a $1/e$ time of 740 ps. The measurement of an absorption spectrum, combined with the knowledge of the radiative lifetime, gives the extent of the inhomogeneous broadening. The electron and hole g-factors can be measured separately by comparing Zeeman shifts of bright and dark excitons in the Voigt geometry [103]. Having access only to the Faraday geometry in this experiment, it is not feasible to obtain an independent measurement of both g-factors. Instead, we measure the Zeeman splitting of the exciton and trion transitions, and make an educated guess of the electron g-factor based on measurements on similar QDs, to obtain the hole g-factor. Figure 5.2 shows B-field dependent absorption of X^- and X^0 transitions. In a first-order approximation, we would expect these to show the same g-factors corresponding to $g_X = |g_e - g_h|$. This is indeed what is seen, both for this dot and two others in the sample, despite there being a large range of g_X (from 0.8 to 1.9). For similar InAs QDs, typical values of the out-of-plane electron g-factor are typically around $g_e = -0.6$ [4] and do not vary significantly with exact QD shape, as opposed to the hole g-factor [104]. For the simulations presented here, we therefore assume an isotropic electron g-factor of $g_e = -0.6$ and an out-of-plane hole g-factor of $g_h = 0.3$. Figure 5.2 additionally shows the difficulty of performing measurements of hyperfine effects in the low B-field regime and in the absence of nuclear spin polarisation: even under 23 mT, no splitting can be resolved and the expected OH field is commensurate with both the radiative linewidth and the spectral diffusion.

5.2 Optically Induced Spin Dynamics

We turn to autocorrelation measurements of the X^- transition. For the ideal two-level system discussed in chapter 2, besides the antibunching and Rabi oscillations decaying on a timescale of the radiative lifetime, we expect a complete loss of correlations on all longer timescales. Intensity autocorrelations, and their detuning dependence, have been used to show fluctuations of the OH field on timescales ranging from tens to hundreds of μs [73, 77]. Here we focus on shorter timescales, from zero delay up to tens of ns. This time window, shorter than OH field dynamics and longer than the radiative lifetime, allows for unobstructed access to the optically-induced electron spin dynamics, revealing a sub-linewidth level structure determined by the hyperfine interaction.

5.2.1 Finite Magnetic Field

First, we look at the photon statistics with an applied field large enough to split the two transitions. Figure 5.3 shows intensity autocorrelation measurements taken at 76 mT in the Faraday geometry, driving the QD below saturation at $s = 0.1$. Using such a low driving power ensures that no bunching arises due to a combination of Rabi oscillations with a finite timing resolution. Measurements at six different detunings are taken. When the laser is set at equal detuning from both transitions (measurement 4), a small degree of bunching is seen ($g^{(2)} - 1 = 0.23$). Additionally, The antibunching dip almost disappears, due to the increased effective Rabi frequency which cannot be resolved with our correlation setup. As the laser is detuned from the point of symmetry, strong bunching appears and continues to increase even when red-detuned from both transitions. The bunching arises due to the spin-flip Raman transition. An optical transition is associated with each of the spin states, and when the laser is further detuned from one transition than from the other, the electron spin is shuffled from an optically bright state to a slightly darker one. This effect leads to photon correlations on a timescale of a few optical cycles and creates bunching in $g^{(2)}$. The clear detuning dependence indicate that the bunching arises from competing processes of optically-induced spin pumping, repumping, and spin relaxation. From exponential fits to the decay of the bunching, we extract similar timescales of ≈ 40 ns for all measurements. This timescale corresponds to a ≈ 2.5 optical cycles at this power, and already shows that the hyperfine interaction modifies the time-averaged branching ratio in the low magnetic field regime.

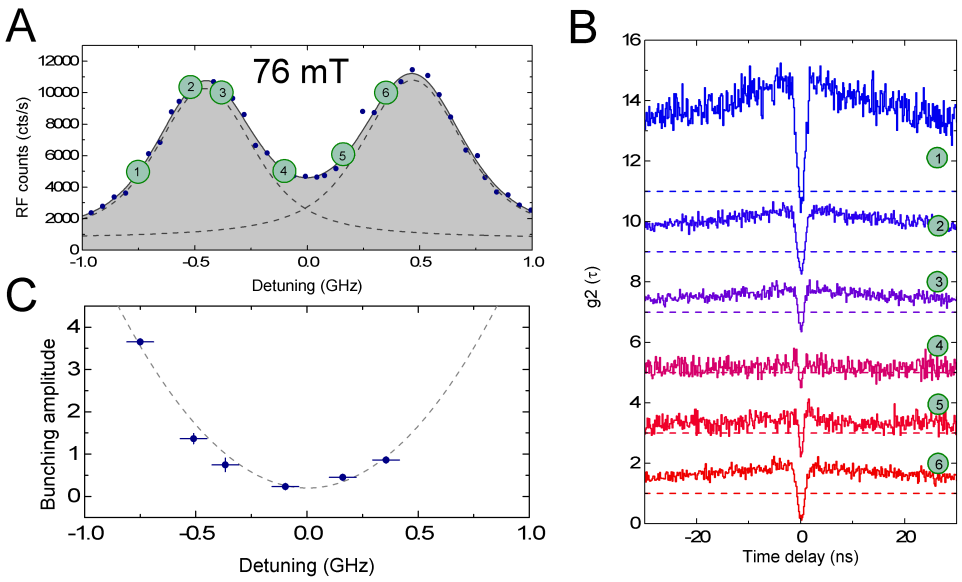

Fig. 5.3 **A.** Detuning-dependent resonance fluorescence (blue circles) from the X^- transition at a driving power below saturation ($s \approx 0.1$) under a finite magnetic field in the Faraday configuration with 1 s integration time. The dashed lines show the lineshapes of the two transitions, derived from a fit to the data. The green points show the detuning settings and average RF intensity for the measurements shown in panel **B**. **B.** Normalised intensity autocorrelations taken at the detunings shown in **A** for $s = 0.1$. Each curve is offset for clarity, and the dashed line represents the $g^{(2)} = 1$ condition. **C.** Extracted bunching amplitudes from exponential fits to the data shown in **B**. The dashed line is a quadratic fit and serves as a guide to the eye.

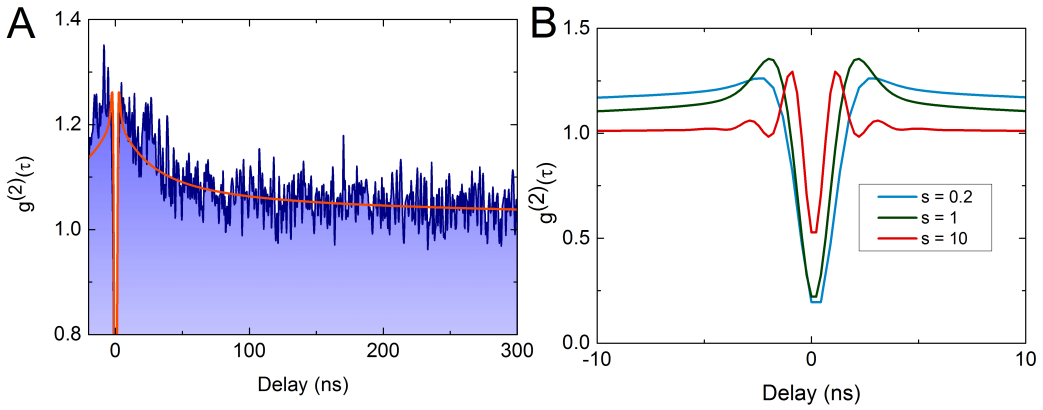

Fig. 5.4 **A.** Low power ($s = 0.1$) intensity autocorrelation for zero mean detuning. The blue curve shows the measured data, normalised to the long term value (at $\tau = 10\mu s$). The orange curve is a simulation using a four level master equation including a diffusion width equal to Γ and averaged over an isotropic OH field distribution with a dispersion of 22 mT. A finite timing resolution of 0.6 ns is also included in the calculation. **B.** Simulations of intensity autocorrelations for different driving powers indicated in the legend. The long-time bunching amplitude is determined by the absorption linewidth and is most clearly observed in the low power regime.

5.2.2 Zero Applied B-field

We perform a similar measurement in the absence of an external magnetic field, shown in panel A of figure 5.4. Again, we drive the QD at $s = 0.1$, initially on resonance. A significant degree of bunching ($g^{(2)} - 1 \approx 0.25$) reveals the spin-flip transitions enabled by the in-plane component of the OH field. The decay timescale of 38 ± 3 ns is consistent with that of Fig. 5.3 for the same driving power, confirming that the same mechanism - optically-induced electron spin flips - is at play in both cases. Panel B shows intensity autocorrelation calculations at different driving powers and shows bunching in all cases. However, there is a clear dependence of the bunching amplitude and timescale on power, marking the transition between two sources of bunching. In the low-power limit, where the mean spin splitting is commensurate with the homogeneous linewidth, the bunching occurs on a long timescale and is related to electron spin dynamics. In contrast, in the high power regime both transitions are homogeneously power-broadened to such an extent that the spin splitting becomes negligible; the bunching amplitude is then entirely due to Rabi oscillations, and no bunching is expected beyond a timescale on the order of the radiative lifetime.

Bunching on a timescale of tens of ns could arise from blinking of the transition on a fast timescale [87]. However, this mechanism should not depend on laser-detuning on the scale of the linewidth, therefore a detuning-dependence should unambiguously point

to optically-induced electron spin flips as the underlying mechanism. Looking back at the finite field measurement of Fig. 5.3, we see that the bunching amplitude shows a local minimum when the laser is symmetrically detuned from both transitions. In this condition, spin pumping and repumping rates are equal and neither spin state is 'darker' than the other. We should observe a similar behaviour in the zero-field case, due to the finite electron spin splitting generated by the OH field.

However, a detuning dependence is not as straightforward to obtain as in Fig. 5.3, due to spectral wandering on the order of the transform-limited linewidth. The largest contribution to spectral wandering is the slow $1/f$-like noise (c.f. chapter 4) and sub-linewidth control of detuning is rendered difficult for long measurements, such as intensity autocorrelation. Instead, we initially set the laser on resonance and save correlation histograms every 50 s while monitoring the mean count rate within each time window. We then postselect the histograms according to their mean count rate, and obtain separate histograms for each intensity bin. The post-selection technique is depicted in Fig. 5.5. By comparison of the intensity bins with an absorption spectrum measured on a shorter timescale (≈ 2 s), we can convert the intensity bins to detuning bins. The bunching amplitude for each detuning bin is extracted by fitting each post-selected histogram with an exponential decay (panel C). The bunching amplitudes are summarised in panel D, showing a sub-linewidth detuning dependence. This confirms that the degree of bunching depends on optically-induced spin pumping and repumping rates.

To fit the data in panel D, we develop a simple model based on solving the 4-level Bloch equations described by the Hamiltonian of equation 5.5. With a finite ground state splitting and a laser detuned from the bare resonance, a steady state ground state population imbalance can be created through preferential excitation of one of the transitions. The calculated laser detuning dependence of the created populations is shown in Fig. 5.6. This imbalance in turn leads to correlations in the RF signal from the QD on the timescale of optical pumping. In order to extract a bunching amplitude from the calculated steady-state spin polarisation, we compare the expected autocorrelation in two regimes: for timescales much smaller than the optical spin pumping rate (but longer than the radiative lifetime) $g^{(2)}(\tau < T_{\mathrm{SP}})$, and the long timescale autocorrelation $g^{(2)}(\tau \to \infty)$. Ignoring further correlations due to electric field and OH field fluctuations and working in the low power regime ($\rho_{11}^{\mathrm{SS}} + \rho_{22}^{\mathrm{SS}} \approx 1$), the unnormalised long timescale autocorrelation value can be approximated as:

$$G^{(2)}(\tau \to \infty) \propto (\rho_{11}^{\mathrm{SS}} \mathscr{L}[\Delta_1] + \rho_{22}^{\mathrm{SS}} \mathscr{L}[\Delta_2])^2 \tag{5.6}$$

where ρ_{ii}^{SS} is the steady state population of ground state i, and $\mathscr{L}[\Delta_i]$ is the photon detection rate from the transition associated with spin i with a Lorentzian dependence on laser detuning

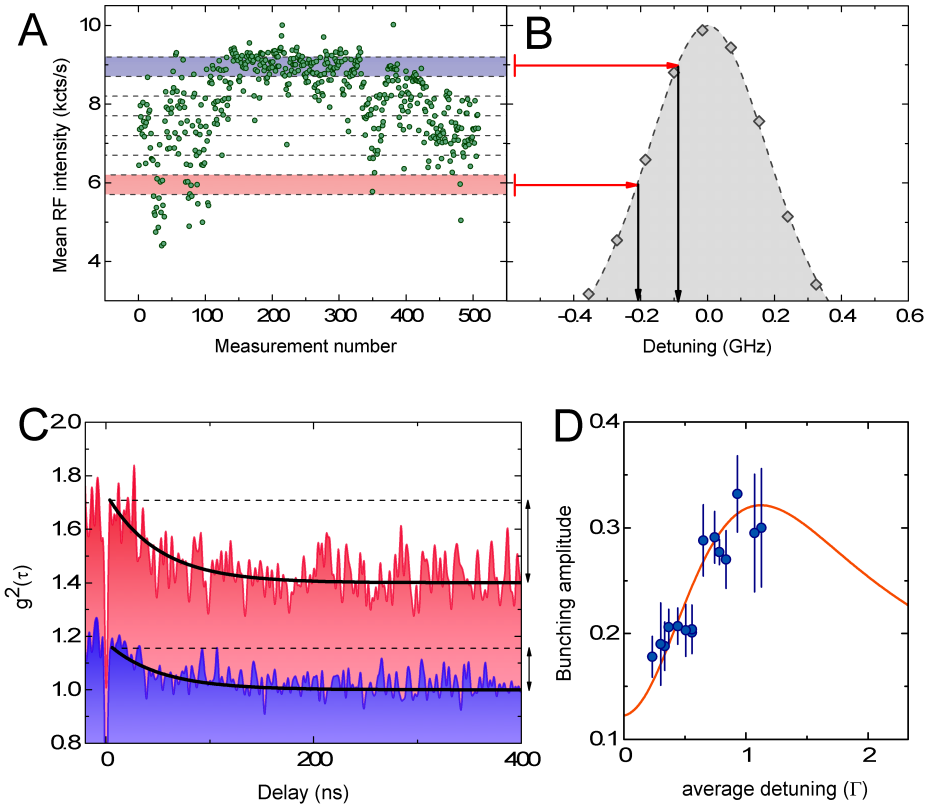

Fig. 5.5 **a.** Mean RF count rate (green circles) for an integration time of 50 s, driving at $s = 1$ initially on resonance. The dashed lines represent the postselection bins used to measure a detuning-dependent $g^{(2)}(\tau)$. The blue and red regions correspond to the post-selected histograms shown in panel **c**. **b.** Absorption linescan taken over $\approx 2s$ used to convert the data from intensity bins to detuning bins. **c.** Two representative post-selected histograms (blue and red curves) corresponding to the intensity post-selection of **a**. These curves are normalised to the long term correlation value. We fit exponential decays to the bunching component of the correlation and extract the bunching amplitude (represented by the arrows). **d.** Extracted bunching amplitudes (blue circles) as a function of post-selected detuning. The error bars represent the standard error in the exponential fits to each post-selected histogram. The red curve shows the calculated bunching amplitude from a 4-level rate-equation model assuming an isotropic OH field distribution with a dispersion of 18 ± 1mT

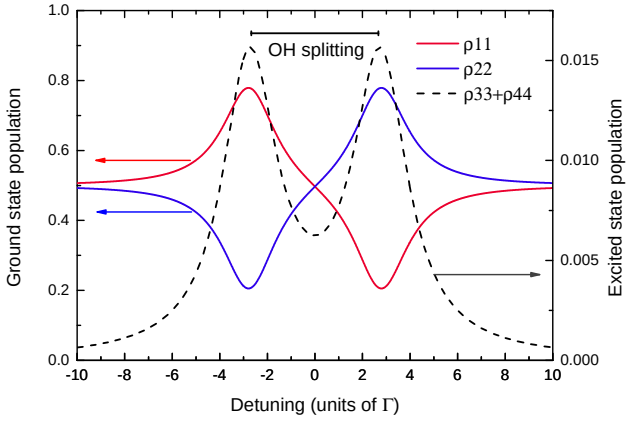

Fig. 5.6 Detuning dependence of the calculated steady-state atomic populations for resonant excitation of the X$^-$ transition at $s = 0.1$. The red and blue curves show the ground state populations and the dashed grey line shows the total population in the excited state manifold. The OH field is fixed with a magnitude corresponding to the splitting in the dashed curve.

Δ_i. For timescales shorter than the optical pumping rate, as the electron spends a fraction of time ρ_{ii}^{SS} in spin state i, we have:

$$G^{(2)}(\tau < T_{SP}) \propto \rho_{11}^{\mathrm{SS}} \mathscr{L}[\Delta_1]^2 + \rho_{22}^{\mathrm{SS}} \mathscr{L}[\Delta_2]^2 \tag{5.7}$$

The bunching amplitude BA is then given by:

$$BA = \frac{G^{(2)}(\tau < T_{\mathrm{SP}})}{G^{(2)}(\tau \to \infty)} - 1 \tag{5.8}$$

We are then left with two free parameters: the OH field dispersion (assuming a Gaussian isotropic distribution) and Gaussian broadening of the line due to electric field noise on a 50s timescale. By fitting the data of Fig. 5.5, we perform a χ^2 analysis to find 18 ± 1 mT and 80 ± 10 MHz respectively. This model is simplistic, in that it ignores both the antibunching at small timescales and the spin pumping rate, but it gives a good quantitative agreement with the data. Although the model depends strongly on the time-averaged magnitude of the OH field, it has no dependence on its orientation. The decay timescale of the bunching corresponds to ≈ 2.5 optical cycles. This is inconsistent with the branching ratio in the Faraday geometry ($\approx 0.5\%$) indicating that the OH field has a significant in-plane component, but this measurement alone doesn't give a quantitative estimate of the in-plane OH field variance. A different measurement method is needed to obtain a good estimate of the full OH field distribution.

5.3 Coherent Raman Spectroscopy under Zero Magnetic Field

We move to measurements of the first order coherence of the trion system, again in the low magnetic field regime. As discussed in chapter 2, the two-level resonance fluorescence is composed of coherent and incoherent fractions, which display different spectral properties. In the low power regime, the coherent fraction dominates giving a spectral linewidth limited either by the excitation laser or the measurement resolution. This regime therefore offers a significant improvement in resolution over absorption spectroscopy and allows for measurement of sub-linewidth features due to the hyperfine interaction.

5.3.1 Deviation from Two-Level System

Panel A of Fig. 5.7 shows a comparison of emission spectra obtained with a driving power of $s = 0.1$ for the neutral exciton and the negatively charged trion transitions. For both measurements, the FP transmission function is determined with a measurement of reflected laser and displays a Lorentzian lineshape with a FWHM of $\approx 20MHz$. The X^0 spectrum shows the expected two-level behaviour, i.e. a single line centered at the laser frequency with a width given by the FP response. This sharp feature is also observed in the case of the X^- spectrum, indicating Rayleigh scattering. However, in sharp contrast with the X^0 transition, two broad sidebands are also seen either side of the peak of elastic scattering. These are typically detuned from the laser frequency by ≈ 200 MHz and have a linewidth of ≈ 250 MHz. These reveal a deviation from two-level behaviour due to inelastic scattering.

Panel B shows a similar comparison between low power X^- emission spectra with and without an applied magnetic field. The application of 100 mT completely suppresses the sidebands, and a behaviour similar to that of a two-level system is recovered. At first glance, it seems that several mechanisms can plausibly explain the observation. Perhaps the sidebands stem from the incoherent contribution to the fluorescence, and by applying the magnetic field, we are simply detuning the QD from the laser and thereby increasing the coherent fraction of the scattering. The sidebands in this case would signify the onset of the Mollow triplet [105], and the splitting between the sidebands would be highly power- and detuning-dependent.

Figure 5.8 shows measurements of the trion RF emission spectra as a function of laser detuning from resonance. We find that the integrated intensity drops, following the absorption lineshape of the transition. However, the shape of the spectrum remains almost unaffected: the detuning between sidebands is constant, and the fraction of emission in the sidebands does not decrease with detuning. These observations point to the fact that these sidebands

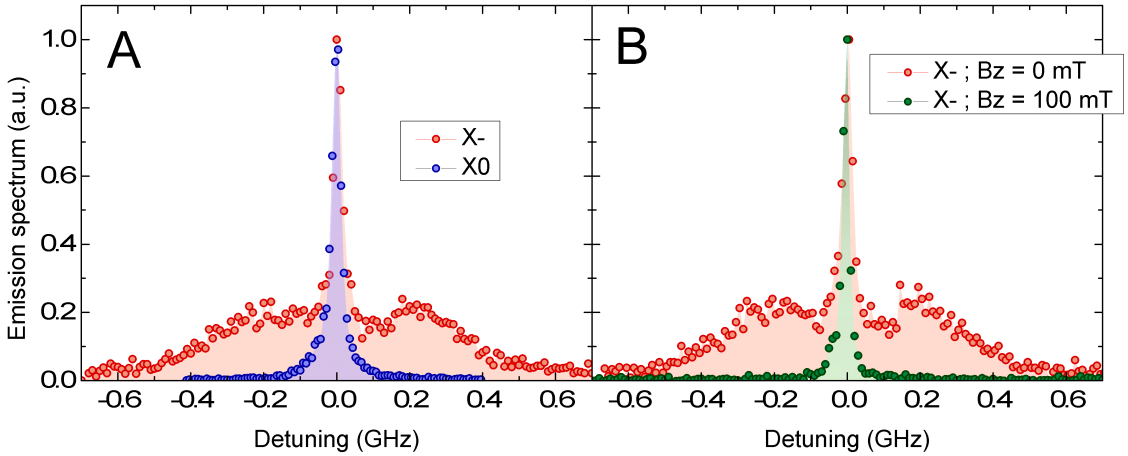

Fig. 5.7 **A.** Typical RF emission spectra measured at low driving power $s = 0.1$ for the X^- (red circles) and X^0 (blue circles) transitions normalised to the peak count rate. **B.** Low-power RF emission spectra measured with (green circles) and without (red circles) an external applied magnetic field in the Faraday configuration.

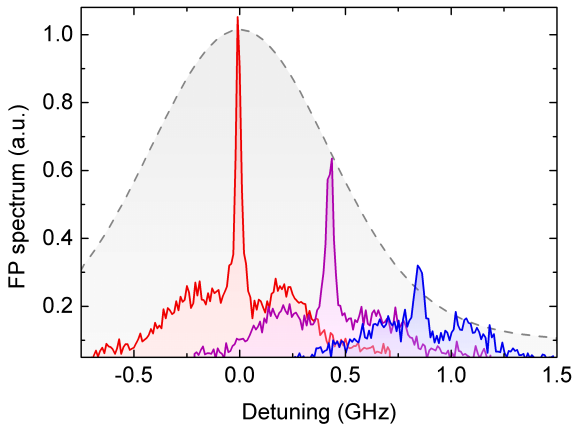

Fig. 5.8 Detuning dependence of the X^- RF emission spectra measured at low driving power $s \approx 0.1$. The laser frequency was kept constant, and the detuning was controlled with the gate voltage. The emission is centered at the laser frequency, but the curves are offset by an amount corresponding to the applied gate voltage for clarity. The dashed grey curve represents the absorption lineshape typically measured for this QD.

arise from a coherent Raman transition. The scattering occurs via a virtual level and the difference in energy is accounted for with an electron spin flip in the basis defined by the OH field.

5.3.2 Calculation of Four-Level Resonance Fluorescence Spectrum

In this section, we present the theoretical methods used for the calculation of the emission spectrum of resonance fluorescence, with a negatively charged QD. The hyperfine coupling to the nuclear spin bath is treated in a mean-field approach, as described in section 5.1. For the coupling to the driving laser field, we will borrow the methods discussed in chapter 2, in relation to the two-level system, which we will generalise to the four-level system here. Once again, we can describe the dynamics in the system with a Liouville equation, using the Hamiltonian of equation 5.5:

$$\frac{\mathrm{d}\rho}{\mathrm{d}t} = -\frac{i}{\hbar}[H,\rho] + \mathscr{L}[\rho] \tag{5.9}$$

where, $\mathscr{L}[\rho]$ is the Lindblad superoperator describing the irreversible dynamics of the system, namely spontaneous radiative decay and other pure dephasing processes. This takes a slightly different form to 2.6, as we are dealing with two distinct optical transitions. Working in the basis defined in section 5.1, we have two dipole allowed transitions: $|1\rangle \rightarrow |3\rangle$ and $|2\rangle \rightarrow |4\rangle$. The Lindblad superoperator, excluding for the moment any pure dephasing terms, becomes:

$$\begin{aligned}\mathscr{L}[\rho] =& \frac{\Gamma_{13}}{2}\left(2\sigma_{13}\rho\sigma_{31} - \sigma_{33}\rho - \rho\sigma_{33}\right) \\ &+ \frac{\Gamma_{24}}{2}\left(2\sigma_{24}\rho\sigma_{42} - \sigma_{44}\rho - \rho\sigma_{44}\right)\end{aligned} \tag{5.10}$$

where Γ_{13} and Γ_{24} are the radiative decay rates corresponding to transitions $|3\rangle \rightarrow |1\rangle$ and $|4\rangle \rightarrow |2\rangle$ respectively. For a stationary stochastic process, according to the Wiener-Khinchin theorem, the spectrum is simply given by the Fourier transform of the first order correlation function of the electric field operator describing the amplitude of the emitted field. In the Heisenberg picture this is given by equation 2.19. The relation between electric field and atomic operators once again differs from the two level case:

$$E^{-}(t) \propto \mu_{13}\sigma_{13}(t) + \mu_{24}\sigma_{24}(t) \tag{5.11}$$

where μ_{13} and μ_{24} are the dipole moments associated with both transitions. So far, we have ignored the vectorial nature of the dipole operators. In contrast with the two-level system, we will have to take the detection polarisation into account which will introduce cross-terms

in the first order correlation function. Assuming a left-hand circularly polarised $|3\rangle \rightarrow |1\rangle$ transition, a right-hand circularly polarised $|4\rangle \rightarrow |2\rangle$ transition, a linearly polarised excitation along $\hat{x}$ and a linearly polarised detection along $\hat{y}$, the detected field can be written:

$$E^{-}_{\text{det}}(t) \propto i\mu_{13}\sigma_{13} - i\mu_{24}\sigma_{24} \tag{5.12}$$

In order to calculate the emission spectrum, we operate in the Heisenberg picture and solve the Langevin equations of motion. These equations of motion have a form similar to the Liouville equation for the density matrix in the Schrodinger picture but also consider a noise operator. We will operate in the Markovian regime where the noise is delta correlated in time so its stationary two-time contribution will be zero. Therefore, the Langevin equation of motion will closely follow equation 5.9, with $\sigma_{ji}(t)$ replacing ρ_{ij}. In a similar way to equation 2.7, we can write the resulting equations of motion for the slowly varying atomic operators in matrix form:

$$\frac{\partial}{\partial t}\Psi(t) = \frac{\partial}{\partial t}\begin{pmatrix} S_{12} \\ S_{13} \\ \vdots \\ S_{43} \\ S_{44} \end{pmatrix} = L\Psi(t) + \Lambda + F(t) \tag{5.13}$$

where $S_{ij} = A_{ij}\sigma_{ij}$, and A_{ij} is a time dependent coefficient used to cancel out terms oscillating at the driving frequency. The condition of unit trace has been used to eliminate S_{11}, giving rise to vector Λ, $F(t)$ is a vector describing the noise operators, and L is a time-independent 15x15 matrix omitted here for lack of space. The RF spectrum can then be obtained by inserting the detected field of equation 5.12 into equation 2.19. Assuming that $|\mu_{13}| = |\mu_{24}|$, we obtain:

$$\begin{aligned} \mathscr{S}(\nu_0) \propto & \int_0^\infty d\tau \langle S_{31}(\tau)S_{13}(0)\rangle e^{-i(\nu_0-\omega_1)\tau} + c.c \\ & - \int_0^\infty d\tau \langle S_{31}(\tau)S_{24}(0)\rangle e^{-i(\nu_0-\omega_1)\tau} - c.c \\ & - \int_0^\infty d\tau \langle S_{42}(\tau)S_{13}(0)\rangle e^{-i(\nu_0-\omega_1)\tau} - c.c \\ & + \int_0^\infty d\tau \langle S_{42}(\tau)S_{24}(0)\rangle e^{-i(\nu_0-\omega_1)\tau} + c.c \end{aligned} \tag{5.14}$$

Each term is closely related to the Laplace transform of the correlation functions $\langle \Psi_i(\tau)\Psi_j(0)\rangle$ with $p = -i(\nu_0 - \omega_1)$ as the variable of the kernel. Therefore, all we need to calculate the

spectrum is to find the values of the Laplace transforms corresponding to the four terms in equation 5.14, which we now write $\Phi_{i,j}(p) = \int_0^\infty \langle \Psi_i(\tau)\Psi_j(0)\rangle e^{p\tau}$.

We first differentiate the correlation function using equation 5.13, and take zero contribution from the noise operators as they have a delta-function correlation in time:

$$\frac{d}{d\tau}\langle \Psi_i(\tau)\Psi_j(0)\rangle = \langle (L\Psi(\tau)+\Lambda)_i \Psi_j(0)\rangle \tag{5.15}$$

Then, using the property of the Laplace transform of a differential ($\mathfrak{L}[f'(t)] = p\mathfrak{L}[f(t)] - f(0)$) and of a constant ($\mathfrak{L}[A] = \frac{A}{p}$), we take the Laplace transform of the previous expression:

$$p\Phi_{i,j}(p) - \langle \Psi_i(0)\Psi_j(0)\rangle = \sum_{k=1}^{15} L_{ik}\Phi_{k,j}(p) + \frac{\Lambda_i}{p}\langle \Psi_j(0)\rangle \tag{5.16}$$

After defining $\varphi_j(p) = (\Phi_{1,j}(p), \Phi_{2,j}(p), \cdots, \Phi_{15,j})$, this can be conveniently rewritten in matrix form and the problem is reduced to simple algebra:

$$(pI_{15} - L)\,\varphi_j(p) = \zeta_j(p) \tag{5.17}$$

where I_{15} is the 15x15 identity matrix, and the ith component of ζ_j is $\langle \Psi_i(0)\Psi_j(0)\rangle - \frac{\Lambda_i}{p}\langle \Psi_j(0)\rangle$, which can be found by calculating the stationary solutions of the Langevin equations of motion. Being a problem with 15 simultaneous equations, the calculation of $\varphi_{i,j}$ is rather cumbersome to perform analytically so it is done numerically in this thesis. In order to obtain spectra with finite linewidths, a real part λ is added to the Laplace variable p, such that $p = -i(\nu_0 - \omega_1) + \lambda$. This parameter gives rise to a Lorentzian spectral resolution with a FWHM of 2λ, corresponding to the Fabry-Perot interferometer cavity linewidth. By comparison with equation 5.14, the full spectrum is then given by:

$$\mathscr{S}(p) \propto \Re\left\{\varphi_{2,8}(p) + \varphi_{7,13}(p) - \varphi_{7,8}(p) - \varphi_{2,13}(p)\right\} \tag{5.18}$$

5.3.3 High Resolution Measurement of the Nuclear Spin Distribution

Combining the mean-field model discussed earlier in this chapter with the theoretical methods of the previous section, we can calculate the expected trion emission spectra for a given nuclear spin distribution. Figure 5.9 shows a low power ($s = 0.4$) emission spectrum along with an absorption spectrum for reference. The spectral features of the emission vary on a scale smaller than the absorption linewidth, highlighting the benefit of using the low-power regime to resolve hyperfine features. The coloured spectra are simulations for different fixed OH fields with a very narrow spectral resolution. The individual spectra are composed of

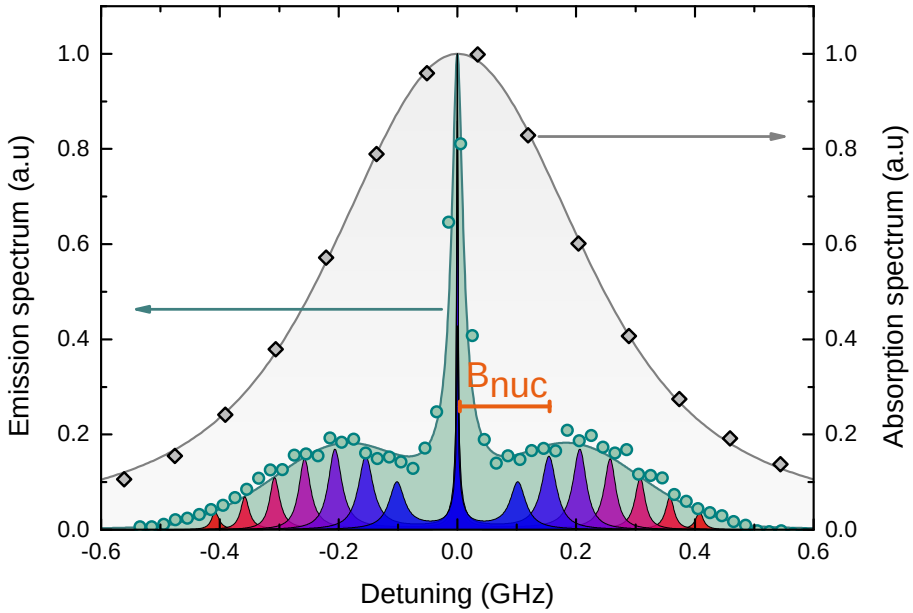

Fig. 5.9 Measured absorption (grey diamonds) and emission (green circles) spectra at $s = 0.4$. For the absorption spectrum, the detuning refers to driving laser detuning from the trion resonance. For the emission spectrum, the detuning refers to the FP detuning from the laser frequency. Different coloured lines show calculated spectra for different fixed OH field magnitudes varying from 12 mT to 47.5 mT, weighted by the nuclear spin distribution. The solid green curve is the calculated time-averaged spectrum with a finite resolution and an OH dispersion of 22mT.

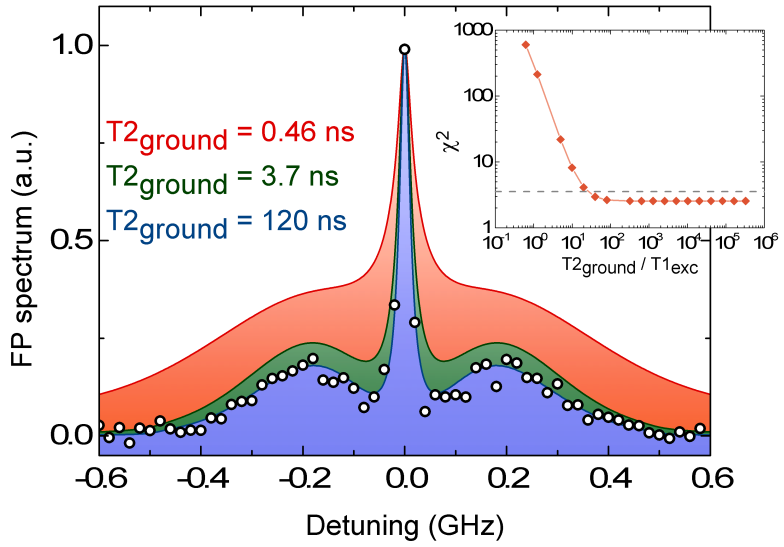

Fig. 5.10 X^- RF emission spectrum (white circles) for a driving power of $s = 0.016$. The curves are simulations for different ground state dephasing rates as shown. The inset shows the reduced χ^2 for different dephasing rates for a best fit analysis. The value for χ^2 reaches a minimum for $T2_{\text{ground}} \approx 70 T1_{\text{excited}}$. The data are therefore consistent with long electron spin coherence. The dashed curve shows the $\chi^2_{\text{min}} + 1$ and gives an indication of the lower limit of best fit spin coherence time.

three narrow peaks: the elastic Rayleigh peak with a width limited to the laser coherence, and two Raman peaks either side of the Rayleigh peak. The Raman peaks are broadened by laser-induced spin relaxation and ground state decoherence. Their detuning from the Rayleigh peak is directly given by the instantaneous ground state splitting. Additionally, the integrated intensity in the Raman sidebands relative to the Rayleigh peak is determined by the branching ratio for the diagonal transitions. The exact shape of the emission spectrum is therefore a complex function of OH field magnitude and orientation, as well as electron spin coherence. The full spectrum is obtained by averaging over a Gaussian distribution of OH field components in three dimensions. These spectra are insensitive on in-plane angle ϕ so it is convenient to work with a cylindrical coordinate system, where the OH field is decomposed into its in-plane and out-of-plane components. On the one hand, the shape of the sideband relates to the time-averaged distribution of OH field magnitudes. On the other hand the integrated intensity in the sideband relative to that of the Rayleigh peak relates to the time-averaged optical selection rules, and therefore the OH field orientation. Therefore, a single spectrum simultaneously contains information on both the in-plane and out-of-plane OH field distributions. For this measurement we find that an isotropic distribution with a dispersion of 22 mT fits the data well.

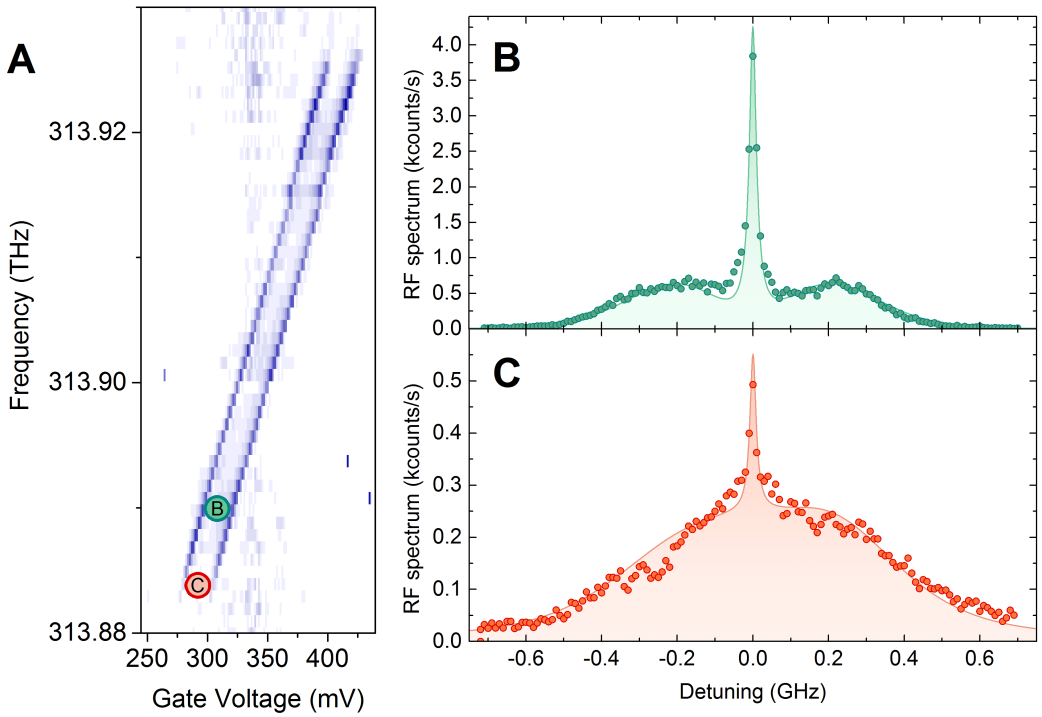

Fig. 5.11 **A.** Differential reflection map of the X^- transition. The green and red labels represent the measurement conditions used in panel **B** and **C**. The cotunneling region corresponds to the gate voltage at which the X^- emission begins to broaden and loses intensity. **B.** X^- emission spectrum taken at low power ($s = 0.1$) far away from the cotunneling region showing coherent Rayleigh and Raman peaks. The solid curve shows a simulation for an OH field dispersion of 18 mT with negligible pure dephasing. **C.** Emission spectrum taken in the cotunneling region, showing a relative decrease of coherent emission and a broad incoherent peak. The solid curve is a simulation with an OH field dispersion of 18 mT, a ground state pure dephasing rate equal to the radiative decay rate, and a detuning of 30 MHz.

Figure 5.10 shows the dependence of the simulated spectra on pure dephasing of the ground states. The dataset used as a comparison is taken at a very low power $s = 0.016$ in order to minimise broadening of the Raman peaks through laser-induced electron spin relaxation. The presence of pure dephasing of the ground states is expected to significantly broaden the sidebands, and we find that the data is consistent with little pure dephasing of the electron spin. A χ^2 analysis suggests a lower bound on the pure dephasing rate at least an order of magnitude longer than the radiative decay rate. The simulations shown here assume a static level structure, but fast fluctuations of the OH field would appear as a pure dephasing in the best fit to the data. Therefore, the data of Fig. 5.10 suggest that the model of the electron experiencing a 'frozen' OH field on the timescale of radiative decay seems valid.

The nature of the sample structure readily offers a method of tuning the electron spin

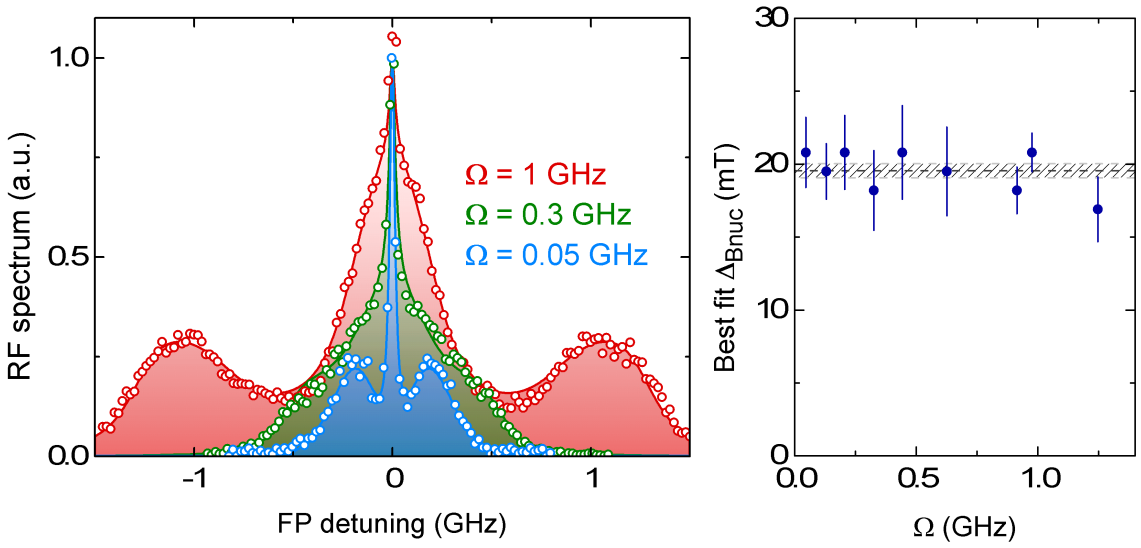

Fig. 5.12 **A.** (a) Emission spectra (hollow circles) measured for different driving laser Rabi frequencies as shown. The solid curves are the best fits with peak height and OH field dispersion as fit parameters. (b) Summary of OH field dispersion values which give the best fits at different Rabi frequencies, where the error bars arise from a $\chi^{(2)}$ analysis. The line and shaded region show the mean best fit OH field dispersion and the standard error respectively.

relaxation rate through cotunneling with the back contact [106]. Figure 5.11 shows emission spectra measured for the same driving power ($s = 0.1$) with two different applied gate voltages. Panel B shows a measurement which is taken far away from the edge of the charging plateau (panel A), where cotunneling rates are slow [106], showing a behaviour similar to Fig. 5.10. Panel C, in contrast, shows a broad incoherent spectrum well fit with the addition of a pure dephasing rate comparable to the radiative decay rate. This verifies that the coherent Raman transitions are highly dependent on the electron spin coherence.

As we have seen from Figs. 5.3 and 5.4, the electron spin dynamics are drastically modified in the presence of the driving laser. In order to see what impact the resonant excitation has on the OH field distribution, we turn to a power dependence of the trion emission spectrum. Figure 5.12 shows emission spectra under different driving powers below ($s \approx 0.1$), above ($s \approx 38$), and close to the saturation point ($s \approx 3$). The sidebands, which are clearly separated from the Rayleigh peak in the low power measurement, are no longer resolved at intermediate power. Increasing the power further generates the well know Mollow triplet, and the system behaves similarly to a two-level system. The solid curves are best fits to simulations using the model described earlier, with the OH field dispersion as the fitting parameter. Panel B shows a summary of best fit OH field dispersions for different driving

powers. We find no significant variation in best fit value over three orders of magnitude in driving power, indicating that, although the driving power may change the timescale of OH field dynamics [77], the time-averaged distribution is unaffected by the measurement. Furthermore, no significant nuclear spin polarisation is created, as expected for a linearly polarised driving field.

The data shown in this section support the conclusion that, in the absence of an external magnetic field, fluctuations in the nuclear spin bath of the QD lead to a fluctuating electron spin splitting and quantisation axis. On the timescale of electron spin dynamics, the 'frozen' nuclear spin model fits the data well, and the hyperfine generated Λ-system can be described as quasi-static. In the absence of an external magnetic field, the time-averaged OH field distribution is isotropic with a Gaussian distribution. For the three QDs measured here, we obtain best fit dispersions of 22 ± 1 mT, 19.5 ± 0.5 mT, and 18 ± 1 mT. The OH field provides a spin splitting and optical selection rules propitious for optical spin control. We have already shown this, to some extent, with single-laser electron spin pumping (c.f. Fig. 5.4). The principle of OH-enabled optical spin control will be extended to two-colour excitation schemes in chapter 6.

5.4 Nuclear Spin Polarisation under Low Magnetic Fields

Already in Fig. 5.7, we have seen that the hyperfine effects in the emission spectrum disappear with the application of a modest out-of-plane magnetic field. The B-field dictates the electron spin quantisation axis and the associated optical selection rules. The branching ratio in the Faraday geometry, determined by light-heavy hole mixing, is small, therefore the emission spectrum is similar to that of a single two-level system. In this section, we take a closer look at the transition between the low- and high-magnetic field regimes. Figure 5.13 shows emission spectra measured at $s = 1$ for different out-of-plane magnetic fields, commensurate with the OH field dispersion. The solid curves are simulations assuming a fixed isotropic OH field distribution, with no mean nuclear spin polarisation. This assumption fits the data well in the case of low (2.6 mT) and high (100 mT) fields, but a striking deviation is seen at intermediate fields. Here the simulations predict increased detuning between the Raman sidebands due to the magnetic field giving an additional contribution to the electron spin splitting, and a decrease in Raman contribution to the total spectrum. However, the data do not show the predicted increase in spin splitting. We fit the spectra at each magnetic field with a sum of two Gaussian peaks (representing the Raman sidebands) and one Lorentzian (for the elastic scattering) peak. Panel B shows the summary of the ratio of best fit Gaussian area to Lorentzian area, as a function of magnetic field. As expected, this decays on a scale

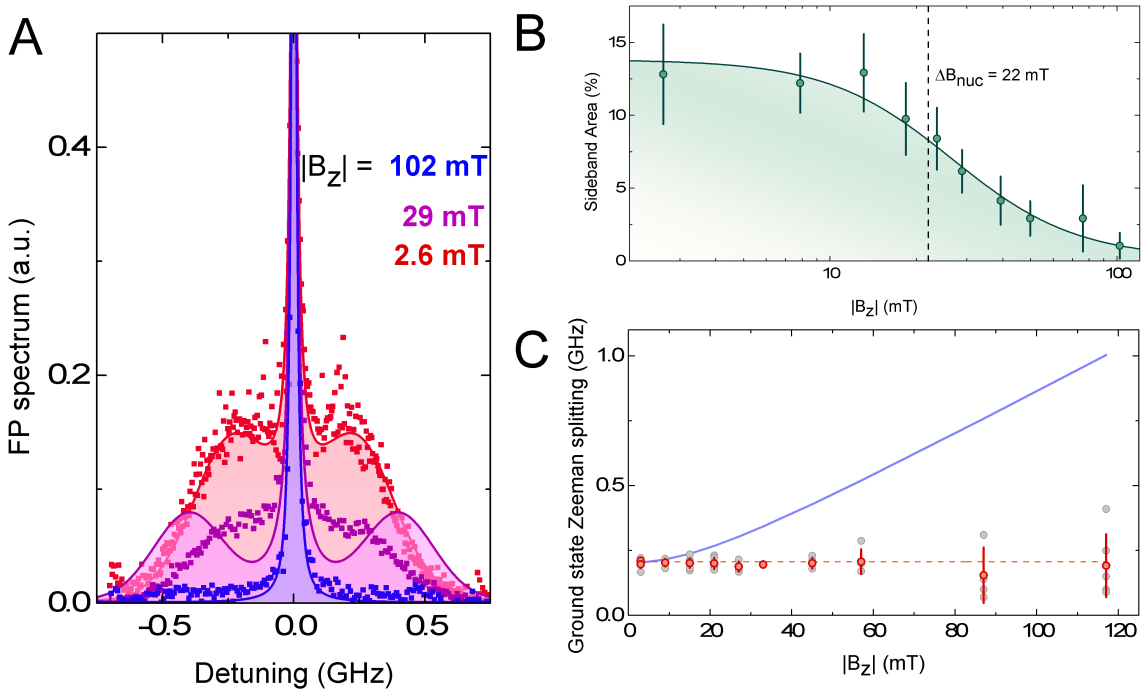

Fig. 5.13 **A.** Low-power X^- emission spectra (squares) for different values of applied magnetic field in the Faraday geometry. The solid curves are simulations assuming an isotropic OH field distribution with a constant dispersion of 22 mT. **B.** Ratio of the sideband area to the Rayleigh peak area extracted from fits to three peaked spectra. The error bars arise from standard errors in the area fit parameters. The solid curve is a Lorentzian fit to the data and serves as a guide to the eye. **C.** Ground state Zeeman splitting (grey circles) and their mean (red circles) extracted from three peaked fits to data. The solid blue curve shows the expected behaviour assuming a constant isotropic OH field distribution with a dispersion of 22 mT. The error bars show the standard deviation of measured Zeeman splittings. The dashed line shows a linear best fit to the data, and its gradient is consistent with zero.

commensurate with the zero-field OH field dispersion. However, the best fit Raman detuning (panel C) is constant up to 100 mT, above which the Raman sideband area decreases such that it cannot be fit. If the OH field distribution were unaffected by the B-field, we would expect a dependence of the form $\sqrt{B_{\mathrm{N}}^2 + B_{\mathrm{ext}}^2}$, which is shown as a solid blue curve.

Clearly, the data are inconsistent with a fixed OH field distribution. In this case, the nuclear spins are polarised so as to minimise the electron spin splitting. Nuclear spin polarisation in the low magnetic field regime has been observed [107], but was induced by circularly polarised optical excitation. Here the excitation polarisation is linear, and the laser does not selectively address either spin state due to the sub-linewidth splitting.

Figure 5.14 shows an emission spectrum under an applied magnetic field of 29 mT. The solid curves are simulations with different OH field distributions. The red curve shows

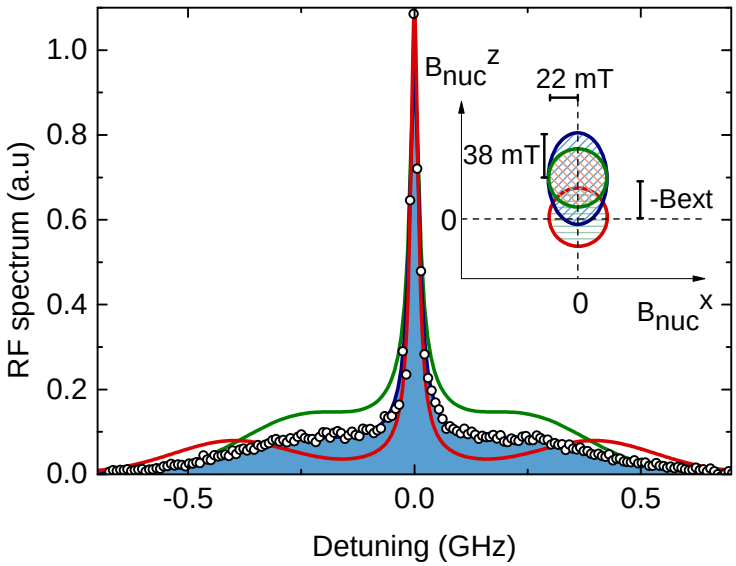

Fig. 5.14 Low power X^- emission spectrum (hollow circles) measured with an applied field of 29 mT in the Faraday configuration. The red curve is a simulation assuming an isotropic OH field with a dispersion of 22 mT, equivalent to the best fit value at zero field. The green curve is a simulation for a mean OH field equal and opposite to the applied field, with a dispersion of 22 mT. The blue curve shows a simulation assuming an anisotropic OH field distribution with a mean equal and opposite to the applied field, an in-plane dispersion of 22 mT and an out-of-plane dispersion of 38 mT. The inset shows the OH field distributions assumed in the corresponding simulations.

the calculated spectrum for an isotropic distribution, with the same dispersion as the best fit value for zero-field and no nuclear polarisation. Here, the increase in electron Zeeman splitting can be seen with an increased splitting of the Raman sidebands. The green curve shows the calculated spectrum for an isotropic distribution with the same dispersion, but with a mean polarisation equal and opposite to the applied B-field, in agreement with Fig. 5.13 C. In this case, the Raman detuning matches the data, but the relative Raman sideband intensity is over-estimated. This indicates that the time-averaged Zeeman splitting fits the data, but the fraction of time that the OH field spends in-plane is overestimated, pointing to an increase in fluctuations in the out-of-plane direction. The blue curve is obtained by lifting the requirement of isotropy, and assuming an out-of-plane dispersion larger than in-plane. We find an in-plane dispersion of 22 mT, unchanged from the zero-field value, and an out-of-plane dispersion of 38 mT fits the data best. The increased out-of-plane fluctuations, possibly linked to the nuclear spin polarisation, cause the time-averaged branching ratio to decrease and the Raman contribution decreases accordingly. The data are obtained by averaging over a few single FP scans, and the signal-to-noise ratio obtained clearly distinguishes between the different models. Typically, we obtain standard errors of 1-3 mT for the dispersion in both orientations, and the model with an isotropic distribution is clearly inconsistent with the data.

The Raman transitions are linked to the flip-flop term of the Hamiltonian and are therefore accompanied by a nuclear spin flip. In principle, this effect does provide a mechanism for creation of nuclear spin polarisation by pumping the diagonal transition [108]. However, we operate in a regime where the electron spin states are not resolved in absorption and we therefore should have approximately equal spin pumping rates in both directions through this mechanism. This would lead to laser power-dependent dynamics but shouldn't lead to a mean nuclear spin polarisation.

A qualitatively different form of nuclear spin polarisation under resonant excitation has previously been observed, dubbed the 'dragging' effect [26, 31]. The name arises from the striking lineshapes observed for neutral and charged excitons in the Faraday and Voigt geometries. Under an applied B-field larger than 1 T, scanning the laser frequency across the blue Zeeman transition leads to a flat-top spectrum with a width up to an order of magnitude larger than the zero-field value. Additionally, this effect is bi-directional indicating it is not driven by electron spin pumping. The nuclear spin polarisation is mediated by the electron spin without flipping it. The non-collinear interaction, arising either from the hole hyperfine interaction [33] or from the quadrupolar field in highly strained QDs [32], leads to a laser detuning-dependent polarisation rate which provides a feedback mechanism locking the QD transition on resonance. It is not clear whether the same mechanism underlies the nuclear

spin polarisation observed here, but the fact that both observations occur under resonant excitation with linearly polarised light indicates a possible link. However, the absorption scans of Fig. 5.2, measured under the same magnetic field as Fig. 5.14, show no such 'dragging' feature.

In summary, we note that the measurement of low-power emission spectra presented here offers a high-resolution probe of nuclear spin polarisation processes in the low magnetic field regime, allowing access to in-plane and out-of-plane dispersions simultaneously. This method could allow for the study of nuclear spin polarisation processes extended into the low B-field regime.

Chapter 6

Hyperfine-Assisted Coherent Population Trapping of an Electron Spin

One of the most important considerations for the experimental realisation of quantum information processing is the interaction between the qubit and its environment. Coupling to an uncontrolled and fluctuating environment leads to loss of information stored within the qubit. However, we also need to control and measure the qubit, which requires a finite coupling to the outside world, in our case through a bosonic reservoir (the field collected with our microscope). In practice it is hard, but feasible, to isolate the qubit from selected parts of its environment. One can directly engineer a qubit such that its coupling to a subset of its environment is minimised [109], or one can use pulse schemes which isolate the qubit from a given spectral region of environmental noise [25, 110]. Alternatively, the environment can be addressed and controlled directly, in order to either limit its fluctuations [31, 111] or change its spectral properties such that it no longer affects the qubit [112, 113]. Much research effort has, in parallel, focused on developing the environment of a qubit as a resource, which can potentially allow for dissipation-driven quantum computation [114–117] and coupling of distant qubits [118, 119]

In the previous chapter, we have demonstrated that, in the limit of low magnetic field, the hyperfine coupling with the mesoscopic nuclear spin bath provides a quasi-static quantisation axis. In addition, the random orientation of the effective magnetic field provides access to spin-flip Raman transitions. In this chapter, we use this hyperfine-generated Λ-scheme to optically create electron spin superpositions via two-colour resonant excitation, through coherent population trapping (CPT). We further show that control of the optical phase, along with laser powers, allows for arbitrary coherent spin state preparation in the basis dictated by the Overhauser field.

The results shown in this chapter are adapted from Ref. [96], and were taken in collaboration with other members of the QD team, particularly Carsten Schulte, Claire Le Gall, and Clemens Matthiesen. Jake M Taylor performed the theoretical analysis of two-colour excitation of the trion system, and his input was central in devising the experiments and understanding its results. Other members of the lab also deserve acknowledgement for tolerating our use of all the lab wavemeters for sustained periods of time.

6.1 Theory of Coherent Population Trapping

In the first part of this section, we will outline the basic concept of CPT with a three-level system and how this effect is typically measured. Of course, the trion system under study here is a four level system with random selection rules, and the theoretical methods involved for two-colour excitation of such a system will be discussed briefly in the second part of the section.

6.1.1 Two-colour Excitation of an Ideal Three-Level System

The original and simplest system studied for CPT [120] is a three-level system, arranged in a Λ-configuration, as shown in Fig. 6.1. Two relatively long-lived ground states are connected to a single excited state through two electric dipole transitions. Two lasers each excite a separate optical transition near-resonantly, and are assumed not to address the other transition. Experimentally, this can easily be achieved by using transitions with orthogonal polarisations, or with a large enough ground state splitting such that the detuned excitation can safely be ignored.

Here we work in the following basis:

$$|1\rangle = \begin{pmatrix} 1 \\ 0 \\ 0 \end{pmatrix} ; |2\rangle = \begin{pmatrix} 0 \\ 1 \\ 0 \end{pmatrix} ; |3\rangle = \begin{pmatrix} 0 \\ 0 \\ 1 \end{pmatrix} \tag{6.1}$$

The Hamiltonian describing the level scheme shown in 6.1 corresponds to the following:

$$\hat{H} = \hbar \begin{pmatrix} \frac{\omega_{\mathrm{GS}}}{2} & 0 & \frac{\Omega_a}{2} e^{i\omega_a t} \\ 0 & -\frac{\omega_{\mathrm{GS}}}{2} & \frac{\Omega_b}{2} e^{i(\omega_b t + \phi)} \\ \frac{\Omega_a}{2} e^{-i\omega_a t} & \frac{\Omega_b}{2} e^{-i(\omega_b t + \phi)} & \omega_{\mathrm{X}} \end{pmatrix} \tag{6.2}$$

where $\hbar\omega_{\mathrm{GS}}$ is the ground state energy splitting, $\hbar\omega_X$ is the excited state energy, ϕ is a relative phase between the fields driving transitions a and b of frequencies ω_a and ω_b respectively. In

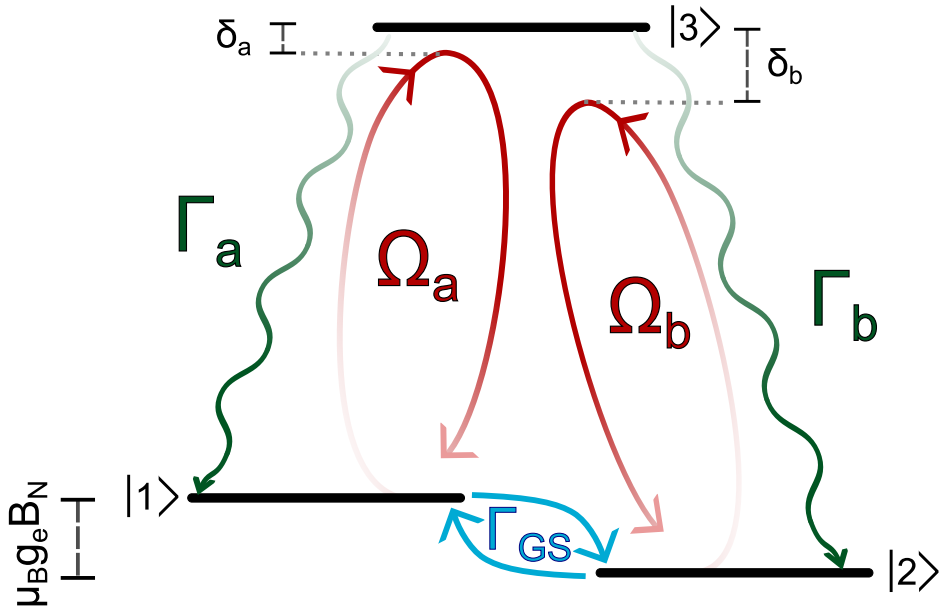

Fig. 6.1 Illustration of a three-level system interacting with two near-resonant electric fields, each addressing a dipole-allowed optical transition. $\Omega_{a,b}$ is the Rabi frequency of transition a,b. $\Gamma_{a,b}$ are incoherent decay rates describing the spontaneous emission from the excited state to states $|1\rangle$ and $|2\rangle$. The total radiative decay rate from state $|3\rangle$ is then $\Gamma = \Gamma_a + \Gamma_b$. Γ_{GS} is the incoherent relaxation rate between ground states. In this approximation of the trion system, the ground state splitting is given by the OH field magnitude B_N.

order to see that such a two-colour excitation scheme leads to the existence of states which do not couple to the excited state, we will first ignore all relaxation mechanisms. A pure state of the system, written in the basis of bare states is then:

$$|\Psi\rangle = \begin{pmatrix} A \\ B \\ C \end{pmatrix} \tag{6.3}$$

Its dynamics, neglecting irreversible dynamics caused by coupling to the environment, are given by the time-dependent Schrodinger equation leading to three coupled differential equations for each component of the state. Working in the interaction picture ($A = \tilde{A}e^{i\frac{\omega_{GS}}{2}t}$,$B = \tilde{B}e^{-i\frac{\omega_{GS}}{2}t}$,$C = \tilde{C}e^{-i\omega_X t}$), we obtain:

$$\begin{aligned}
\dot{\tilde{A}} &= -i\frac{\Omega_a}{2}e^{i\delta_a t}\tilde{C} \\
\dot{\tilde{B}} &= -i\frac{\Omega_b}{2}e^{i\phi}e^{i\delta_b t}\tilde{C} \\
\dot{\tilde{C}} &= -\frac{i}{2}\left(\Omega_a e^{-i\delta_a t}\tilde{A} + \Omega_b e^{-i\delta_b t}\tilde{B}e^{-i\phi}\right)
\end{aligned} \tag{6.4}$$

where $\delta_{a,b}$ is the detuning of laser a,b from the transition $|1\rangle \rightarrow |3\rangle, |2\rangle \rightarrow |3\rangle$. Considering the third equation at the two-photon resonance condition (TPR) $\delta_a - \delta_b = 0$, it is clear that for a certain combination of $\tilde{A}$ and $\tilde{B}$, the excited state population will no longer be time dependent. That is, for an initial ground state superposition fulfilling the condition $\Omega_a\tilde{A} + \Omega_b\tilde{B}e^{-i\phi} = 0$, there will be no optical excitation. This state is called the dark state in such a system and can be written:

$$|\Psi\rangle = \frac{\Omega_b|1\rangle - \Omega_a e^{i\phi}|2\rangle}{\sqrt{\Omega_a^2 + \Omega_b^2}} \tag{6.5}$$

Spontaneous emission and ground state decay, which we have neglected in the above, will change the situation slightly. However, in general there will still be a ground state superposition which will be much longer lived than its orthogonal state. In other words, we can rewrite the system such that an effective driving field only addresses one ground state, in which case we have fast optical pumping into the dark state. In the dressed ground state manifold, we effectively create an imbalance between spin decay rates: in one direction it is linked to the optical pumping rate and in the other to the ground state decoherence. Thus, for a system with long coherence times, we can initialise the state on a timescale of order

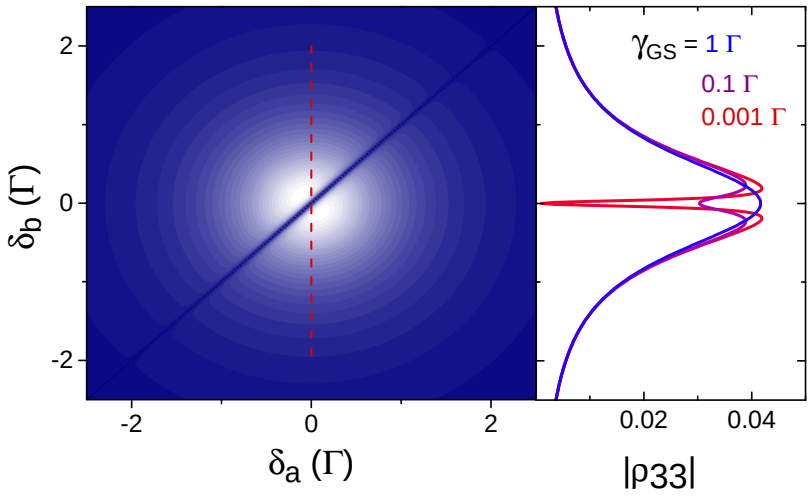

Fig. 6.2 Calculated excited state population for two-colour excitation of the three-level system, as a function of the laser detunings from resonance. The lasers each have a driving power of $s = 0.1$, and negligible ground state relaxation and dephasing is assumed. The right panel shows a linecut of the left panel along the red dashed line, for different ground state pure dephasing rates, as shown in the legend.

Γ with high fidelity. The lifetime of the created dark state depends critically on the ground state decoherence, as it is a coherent superposition state.

Typically, the presence of CPT is observed experimentally as a sharp spectral feature, namely a drop in absorption when the lasers satisfy the TPR condition. To model a realistic three-level system, with excited and ground state relaxation and pure dephasing, we numerically solve the Bloch equations in the steady-state. The calculated excited state population as a function of pump and probe detunings is shown in Fig. 6.2, in the case of low-power excitation of $s = 0.1$ for both lasers. The creation of a dark state can clearly be seen as a sharp drop in absorption along the diagonal, where the TPR condition is fulfilled. Furthermore, the visibility of the dip and its width depend sensitively on the ground state coherence, and for a pure dephasing rate equal to the radiative decay rate, the dip disappears. In the dressed ground state manifold, the effective spin relaxation rates in both directions become commensurate, and no net spin polarisation is observed.

However, the predicted two-colour spectrum depends critically on driving power. The situation becomes more complex when the pump Rabi frequency is larger than the radiative decay rate, in which case the two-level system addressed by the pump is dressed. The absorption spectrum of the probe will then exhibit a splitting proportional to the pump Rabi frequency. This effect, known as the Autler-Townes splitting, has been observed

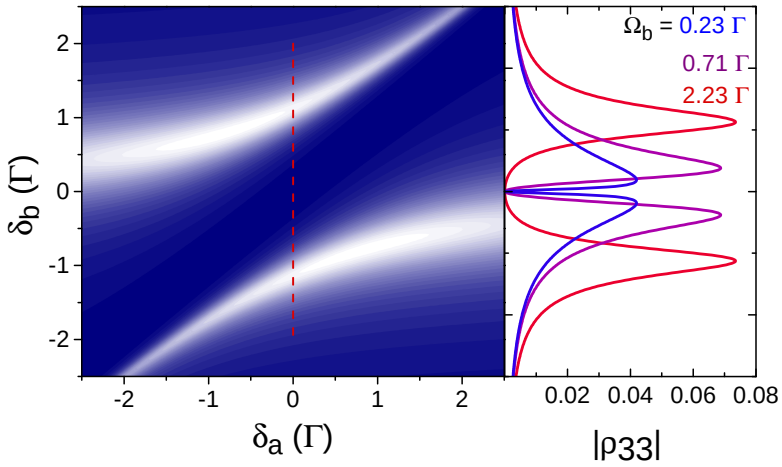

Fig. 6.3 Calculated excited state population for two-colour excitation of the three-level system, as a function of the laser detunings from resonance. The laser addressing transition a has a driving power of $s = 10$, and the laser addressing transition b has a driving power of $s = 0.1$. Negligible ground state relaxation and dephasing is assumed. The right panel shows a linecut of the left panel along the red dashed line, for different Rabi frequencies describing transition b, as shown in the legend.

previously for the neutral exciton [121, 122] and the charged trion [68] transitions of a QD. The calculated absorption spectrum for a pump power of $s = 10$ is shown in Fig. 6.3. When the pump is on resonance with transition a, the probe absorption spectrum shows a splitting, with still zero absorption at zero detuning. The zero-detuning dip in this case is caused both by CPT and the onset of Autler-Townes splitting. An unambiguous demonstration of CPT therefore requires driving powers well below saturation, where the Autler-Townes splitting is smaller than the radiative linewidth.

6.1.2 Extension to the Hyperfine-split Trion System

The trion system under consideration is more complex than the simple three-level model of the previous section. Here we will follow the four-level model discussed in chapter 5 and briefly outline the added complications to the theoretical modeling of CPT in such a system. Firstly, there is a heavy-hole spin in the excited state, leading to two near-degenerate states. Secondly, the spin splittings are determined by a randomly evolving OH field and will generally be smaller than the excited state linewidth. Thirdly, fluctuations in the OH field orientation lead to random optical selection rules. We therefore have a double Λ-

system where each excited state is in general coupled to both ground states. We also cannot selectively excite any one branch of the trion system as we do not have spectral or polarisation selectivity in a time-averaged measurement. All these effects mean the theoretical treatment of two-colour excitation in this system is not as simple as the previous section suggests. It is not even clear, a priori, that CPT can occur in this system considering the presence of a second excited state [123].

Adding a second linearly polarised excitation laser into the system is not as trivial as the aforementioned three level model. As the OH field evolves randomly, the optical selection rules in general do not coincide with the laser polarisations, therefore we obtain terms in the Hamiltonian which oscillate with multiple frequencies. Thus, one of the main difficulties in analysing this system is the fact that we do not have a rotating frame which allows for the cancellation of these terms. The theoretical analysis of CPT in the trion system was performed by Jake M Taylor, and we will therefore only briefly discuss the main results here. The full analysis is given in the supplementary information of Ref. [96]. By treating the driving fields as perturbations, the eigenvalues of the ground state effective Hamiltonian can be calculated. Their imaginary parts correspond to decay rates of the ground state spin eigenstates, i.e. bright and dark state decay rates. For equal and low laser powers, in the absence of an external field, these can be written as follows, after removing an overall real term to both eigenvalues:

$$\varepsilon_{\pm} \approx -i\gamma/2 \pm \sqrt{(B-\delta)^2/4 - \gamma^2 \sin^2(\theta)/4} \tag{6.6}$$

where δ is the angular frequency difference between the two lasers, θ is the angle the OH field makes with the optical axis, B is the ground state splitting in angular frequency due to the OH field magnitude, and γ is related to the optically-induced spin flip rate:

$$\gamma = \frac{\Omega_a^2 \Gamma}{\delta_a^2 + \Gamma^2} \tag{6.7}$$

where δ_a is the detuning of laser a from transition $|1\rangle \rightarrow |3\rangle$. A long-lived dark state therefore exists for $\gamma^2 \sin^2(\theta) > (B-\delta)^2$ as one eigenstate consequently has a longer lifetime than the other. Furthermore, this dark state is a superposition state in the basis defined by the OH field orientation.

In order to compare the measurements with theory, the detuning dependent absorption is calculated by integrating the time-dependent Liouville equation numerically. In general, the solutions will oscillate at the difference frequency of the lasers, so the mean absorption

over several periods is taken as the pseudo steady state. An average over 150 nuclear spin configurations is then taken to simulate random fluctuations of the OH field.

6.2 Experimental Methods

All the measurements discussed in this chapter deal with two-colour excitation of a Λ-scheme. This entails some practical complications over the standard resonance fluorescence schemes used in previous chapters. Specifically, we require two narrow-band resonant lasers to excite the two branches of the Λ-system and we simultaneously need to detect the QD fluorescence with a high signal-to-noise ratio. In addition, we want the two lasers to be linearly orthogonal to each other, such that they address different optical transitions and to avoid interference effects. For this, we combine the lasers at a polarising beam-splitter before coupling into the polarisation-maintaining (PM) excitation fibre. The fibre has two stress members within the cladding in order to break the circular symmetry and induce birefringence within the fibre. Consequently, there are two preferential input polarisations between which the cross-talk is small allowing for high polarisation extinction ratio. A half-wave plate is used before the fibre in order to match the axis of the PM fibre. We measure the polarisation extinction ratio at the microscope head to be typically ≈ 1000. We use two separate external-cavity diode lasers, each frequency- and power-stabilised with PID feedback control to $\pm 2MHz$ and $\pm 1\%$ respectively. The long-time mutual coherence between the two lasers is limited by the frequency stabilisation scheme and is around 5 MHz for long measurements [124]. This value is our frequency resolution in two-colour absorption spectroscopy.

The detection of resonance fluorescence using cross-polarisation of the detection path is unfeasible with this excitation scheme, as the laser leakage will dominate over the QD signal. Additionally, the detuning between the lasers will be typically on the order of the electron spin splitting, which, as seen in the previous chapter, is around 200 MHz. Separating the two lasers spectrally would therefore require a complex setup, such as a high finesse cavity or stabilised interferometer. Instead, we detect the QD fluorescence with two different methods: a slightly modified differential reflection technique, and the phonon-sideband detection discussed in chapter 4.

For differential reflection with two-colour excitation, we again modulate the gate voltage at a frequency of order 1 kHz and demodulate the signal obtained on a photodiode. However, one of the two laser inputs is suppressed by using a linear polariser in the detection path. The degree of polarisation suppression is typically much worse than with single-laser excitation, as we do not have a linear polariser in the excitation path and therefore rely on the polarisation extinction ratio of the PM fibre. This detection method is useful as it allows us to measure

the response to one laser independently of the other. We can therefore perform 'pump-probe' experiments which are a standard technique used to demonstrate CPT in systems with optically resolved ground states [68, 125, 126]. Considering the Λ-system shown in Fig. 6.1, this would give a DR contrast which is proportional to one of the optical coherences, i.e. $\propto \frac{|\rho_{13}|}{\sqrt{s_{\text{probe}}}}$ if the laser addressing transition $|2\rangle \rightarrow |3\rangle$ is suppressed. However, if the pump signal is not completely suppressed, this technique projects both signals onto the same polarisation and can lead to interference effects. Such effects can lead to spectrally sharp drops in signal which is also the telltale sign of CPT. Using differential reflection can therefore lead to ambiguous results, as well as being a relatively slow measurement.
The second technique used is the phonon-sideband detection described in chapter 4. This method allows us to measure the excited state population with arbitrary flexibility in excitation frequency and polarisation and is therefore ideally suited to the measurement of CPT with sub-linewidth spin splitting. Another advantage of this technique over differential reflection is that it gives access to the QD photons with no laser background and therefore allows for high-bandwidth correlation measurements.

6.3 Hyperfine-assisted Coherent Population Trapping

In this section, we show two-colour absorption spectroscopy measurements at low magnetic fields. As discussed previously, two different mechanisms will lead to a similar effect, namely a drop in absorption in a certain spectral region fulfilling the TPR condition. Figure 6.4 shows two-colour differential reflection measurements taken at combined laser power approximately equal to the saturation point (panels **A** and **B**) and well above it (panels **C** and **D**). The high power data shows that the pump laser dresses part of the trion system, which the probe sees as a splitting larger than the radiative linewidth in the absorption spectrum. This is the Autler-Townes splitting, arising from the coherent light-matter interaction. Observant readers may also note a sharp peak at equal laser frequencies, absent from the theoretical prediction. This is caused by imperfect laser suppression, and the pump laser leakage is projected onto the probe polarisation. The sharp feature is thus a heterodyne signal when the detuning corresponds to the gate modulation frequency. Lowering the laser powers reduces the Autler-Townes splitting until it is sub-linewidth, and a dip is still observed at the TPR. This dip is a result of CPT, combined with the onset of an Autler-Townes splitting. This measurement highlights the importance of working in the low-power regime, to obtain a signal unambiguously related to CPT alone.

Figure 6.5 shows two-colour measurements for equal laser powers corresponding each to $s = 0.1$, detected with the phonon sideband. In this case we expect the Autler-Townes

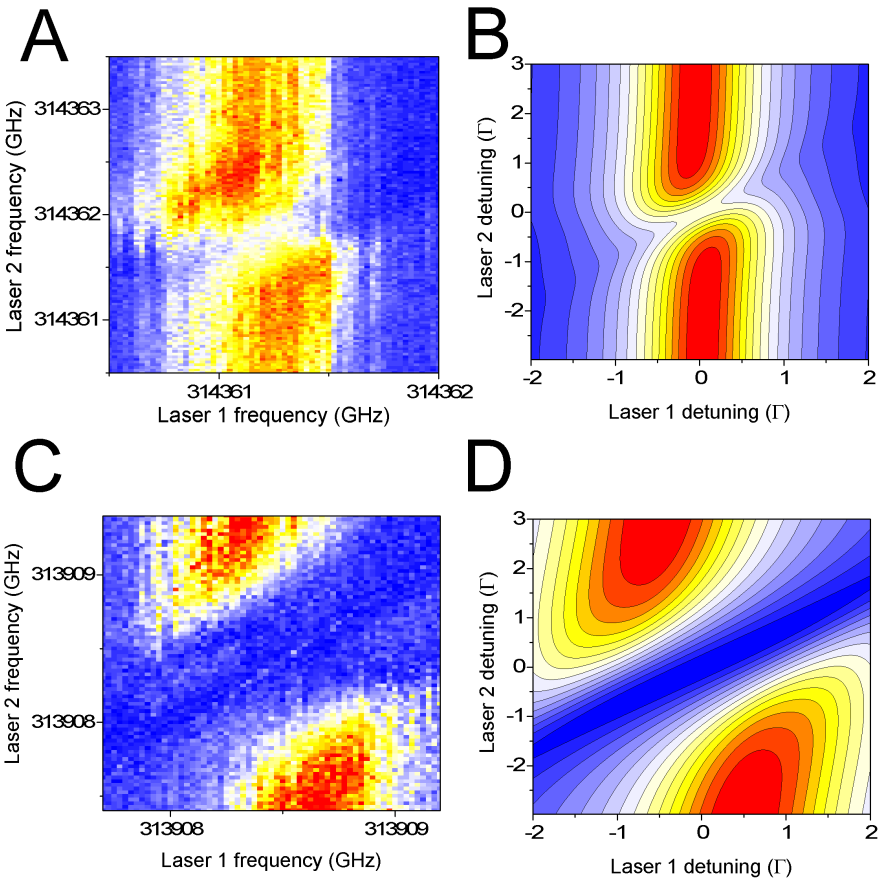

Fig. 6.4 **A.** Measurement of QD absorption with two-colour resonant excitation detected in differential reflection. Laser 2 (pump) is suppressed by a cross-polarisation technique. Laser 1 and 2 drive the QD below saturation, at $s \approx 0.3$ and $s \approx 0.9$. **B.** Simulation of $|\rho_{23}|$ as a function of laser detuning for parameters corresponding to **A** assuming a three level system with fixed spin splitting. **C.** Similar measurement to **A**, but with laser 1 and 2 driving at higher powers of $s \approx 15$ and $s \approx 0.6$. **D.** Simulation of $|\rho_{23}|$ for parameters corresponding to panel **C**, assuming a three level system with fixed spin splitting.

splitting due to either laser to be $\approx 0.22\Gamma$ meaning that its effect on the absorption at the TPR will be smaller than the CPT contribution. At zero-magnetic field, we observe an increase of QD fluorescence when both lasers are close to resonance, with a spectrally sharp drop in signal around the TPR. The noise in such measurements is mainly caused by slow spectral wandering of the central frequency of the transition. This can be confirmed by comparing the noise properties for symmetrically detuned lasers and equally detuned lasers. The noise in the former region (upper left and lower right edge of the central peak) is reduced compared with the latter region (upper right and lower left), consistent with a noise source leading to a random fluctuations in the central frequency. Panel B shows a four level simulation for experimental parameters corresponding to panel A. A small degree of nuclear spin polarisation is added empirically as an added contribution to the electron spin splitting. A four-level numerical simulation assuming a mean Zeeman splitting of 400 MHz gives a best fit to the data. In both the data and the simulation, a decrease in fluorescence along the diagonal corresponding to the TPR indicates preparation of the electron spin in a coherent dark state. When an external magnetic field is applied (panels **C** and **D**) the situation changes considerably. Four peaks are observed, corresponding to the different permutations of two lasers addressing two optical transitions. Notably, the upper-left and lower-right peaks, corresponding to the two lasers addressing different transitions, are more intense than the other two, corresponding to both lasers addressing the same transition. This is due to optical pumping of the spin in the latter, which is prevented by optical repumping when the lasers address different transitions. Furthermore, no sharp decrease of fluorescence is seen on these peaks, showing that the Raman transitions are suppressed and the fraction of the OH field distribution giving rise to CPT is reduced.

Figure 6.6 shows the measured QD fluorescence as a function of two-photon detuning $(\delta_1 - \delta_2)/2$ for the condition $\delta_1 + \delta_2 = 0$. This corresponds to a diagonal linecut of the measurements shown in Fig. 6.5, along the dashed green line. Panels A and B show the measured absorption at 0 mT and 18.4 mT respectively. The 0 mT curve is an average of two separate linecuts. A narrow CPT dip is clearly visible in the absence of an applied field, at the TPR. Two simulations are shown as a solid blue curve and a dashed green curve, obtained with the four-level and three-level models respectively. In the case of the four-level model, the measured OH dispersion is used along with a pure dephasing rate of $2\pi \times 1$ MHz, and the best fit is obtained for a mean spin splitting of 400 MHz. For the three level model, a fixed ground state splitting is assumed and a dephasing rate of $2\pi \times 2.6$ MHz gives a best fit. There is good qualitative agreement between the models, indicating that the interpretation of the trion as a Λ-system is valid. The low visibility of the CPT feature is a result of its intermittent nature: only a fraction of the OH field distribution provides the necessary Λ-scheme for CPT.

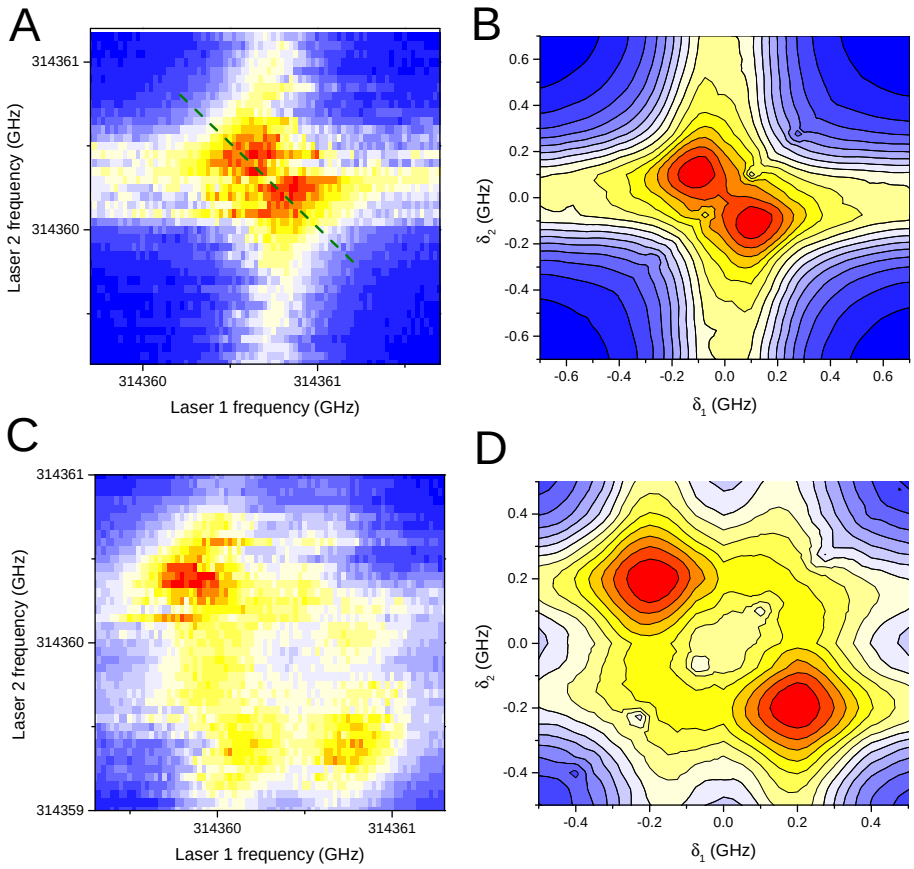

Fig. 6.5 **A.** Measurement of QD absorption with two-colour resonant excitation with phonon sideband detection. Laser 1 and 2 drive the QD below saturation, both at $s \approx 0.1$. **B.** Simulation of QD fluorescence as a function of laser detunings for parameters corresponding to **A** for a four-level model with a mean ground-state splitting of 400 MHz. **C.** Similar measurement to **A**, but with an applied magnetic field of 52 mT. **D.** Simulation of QD fluorescence for parameters corresponding to panel **C**, assuming a four-level model with a mean ground-state splitting of 800 MHz.

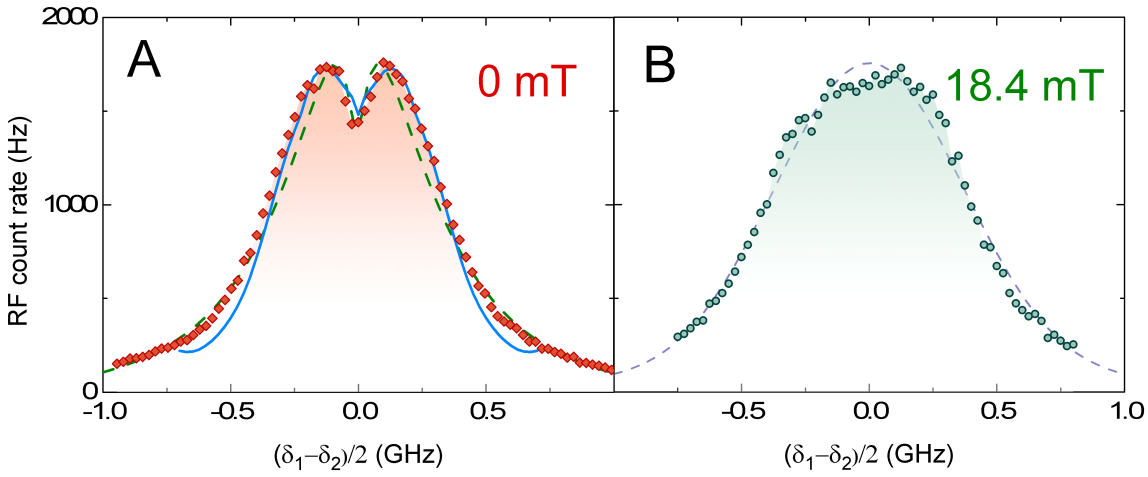

Fig. 6.6 **A.** Measured QD fluorescence (red diamonds) as a function of two-photon detuning for the condition $\delta_1 + \delta_2 = 0$. The blue solid curve shows a simulation for the four level model with a mean ground state splitting of 400 MHz and a pure spin dephasing rate of $\gamma_{GS} = 2\pi \times 1$MHz. The effect of electric field is added as a Gaussian distribution of central frequencies of $\approx 150MHz$. The green dashed curve is a simulation for a three level system with a pure spin dephasing rate of $\gamma_{GS} = 2\pi \times 26$MHz, and a similar Gaussian central frequency distribution. **B.** QD fluorescence as a function of two-photon detuning with the application of a Faraday-geometry magnetic field of approximately the same magnitude as the OH field. The dashed curve is a fit to a Voigt lineshape.

Therefore, stable coherent dark states are generated intermittently and sustained for a finite period of time, dictated by the slow dynamics of the nuclei. This is in contrast to systems showing low-visibility CPT due to fast pure dephasing of the ground state on the same order of magnitude as the radiative decay rate [125]. With an applied field comparable to the OH field dispersion, the CPT dip vanishes as we recover a two-level response. The absorption is additionally broadened as the magnetic field increases the mean Zeeman splitting. However, a single-peak Voigt profile fits the data well, suggesting that coherent effects such as CPT no longer play an important role.

In Fig. 6.6, the effect of CPT is clear from the lineshape when scanning across the TPR. Similarly to the data shown in chapter 5, we expect the CPT visibility to depend on the applied magnetic field, due to its effect on the optical selection rules. However, one has to be careful in the method used to measure the CPT visibility in measurements such as Fig. 6.6. We measure the CPT visibility from the loss of QD absorption at the TPR when the second laser is switched on, compared with a purely linear power dependence. For this, we compare the count rate at the center of the dip at the TPR (corresponding to $\omega_1 \approx \omega_2$) with the count rate measured with one of the lasers far detuned. The raw data are shown in panel A of Fig.

6.7. A non-monotonic behaviour is seen, with a minimum around 15mT. This loss of signal arises from three separate mechanisms: the onset of saturation of the transitions even at low powers, incoherent spin pumping, and CPT. We therefore subtract the first two contributions in order to extract the corrected CPT visibility (shown in panel B of Fig. 6.7). At 0 T, the detuning from either transition is comparable to the linewidth, and spin pumping does not contribute to the absorption sub-linearity, as the optically induced pumping/repumping rates are far greater than the spin relaxation rate. When a field is applied which starts to split the lines ($B_{\text{ext}} > 20$ mT), the lasers will preferentially address one spin state when $\omega_1 \approx \omega_2$ and $\delta_a \approx 0$. Therefore, an imbalance is created between optically-induced pumping and repumping rates. The latter becomes comparable to the spin relaxation rate when the Zeeman splitting is larger than the radiative linewith, while the pumping rate is still ≈ 26 MHz (see Fig. 5.3 and 5.4). An increase in power therefore forces the electron to spend more time in the spin state for which the laser is detuned, leading to an added sub-linearity in the power dependence. We model this with rate equations to describe the electron spin populations. This model therefore does not take into account any coherent effect such as CPT. We quantify the sub-linearity through the loss defined as:

$$Loss = 1 - \frac{P_1 \cdot I(P_2)}{P_2 \cdot I(P_1)} \tag{6.8}$$

where P_1 and P_2 are the single- and two-laser combined powers, $I(P_2)$ is the photon detection rate at an excitation power of P_2. In our measurement we use equal laser powers, hence $P_2 = 2 \cdot P_1$. A loss of 0 indicates a perfectly linear power dependence, and a loss of 0.5 means that doubling the combined laser power does not increase the QD absorption. The average signal for a given power and detuning from both transitions is given by:

$$I(P) = \frac{T_1(P) \cdot S(1, \Delta_1, P) + T_2(P) \cdot S(2, \Delta_2, P)}{T_1(P) + T_2(P)} \tag{6.9}$$

where $T_1(P)$ is the average time spent in spin state i, and $S(i, \Delta_i, P)$ is the photon detection rate when the electron is in spin state i (before the spin is pumped into the other state) with the lasers equally detuned from the corresponding vertical transition (green arrows in Fig. 5.1) by Δ_i. Defining $\Gamma_i(\Delta_i)$ as the rate at which the spin in state i is pumped (both optically and through spin relaxation) to the other spin state, the average fraction of time spent in state i is then:

$$T_i(\Delta_i) = \frac{1}{\Gamma_i(\Delta_i)} = \frac{1}{\mathscr{L}[\Delta_i]\Gamma_{\text{OP}} + \Gamma_{\text{GS}}} \tag{6.10}$$

Here $\mathscr{L}[\Delta]$ is a Lorentzian profile normalised to $\mathscr{L}[0] = 1$, Γ_{OP} is the optical spin pumping rate at zero detuning, and Γ_{GS} is the non-optical spin relaxation rate which is assumed to be detuning independent and magnetic field independent over the range measured.
Here, both the photon emission rates and the time spent in either spin state depend on the applied laser power. We assume that both transitions saturate in the same way as a simple two-level system, i.e. when doubling the laser power, with s being the saturation parameter:

$$S(1,\Delta_i,P=2s) = \frac{\frac{2s}{2s+1}}{\frac{s}{s+1}} S(1,\Delta_i,P=s) \tag{6.11}$$

We also assume that the optically induced pumping rates, as they are proportional to the excited state population, follow the same power dependence and do not depend on B-field on the scale of tens of mT. We justify this assumption by noting that the decay timescales for 0 T and 76 mT are the same for equal laser powers (c.f. Figs. 5.4 and 5.3).
After integrating over the OH field distribution, and using the parameter for Γ_{OP} obtained from Fig. 5.4, we are left with one free parameter: Γ_{GS}. Fig. 6.7 shows simulations for different spin relaxation rates alongside the raw data. These values are consistent with the spin relaxation rate observed for a different QD on the same sample. The best fit for this dot gives a ground state relaxation rate of 4.7 kHz. We then subtract the corresponding simulation from the raw data to obtain the corrected CPT visibility shown in panel B of Fig. 6.7. This shows an exponential decay on a scale smaller than the OH field dispersion, qualitatively consistent with the suppression of the Raman transitions through the application of a Faraday-geometry magnetic field seen in Fig. 5.13. However, both decays are highly sensitive on the degree of dynamic nuclear spin polarisation, which could vary significantly between a single-laser measurement with fixed detuning and a two-colour measurement with scanning lasers. Therefore, we do not necessarily expect the same decay scale for both measurements.

Finally, the dependence of this feature on electron spin coherence is probed straightforwardly by comparing measurements taken at the center of the charging plateau and at at the plateau edge, where cotunneling rates are enhanced, thereby significantly reducing spin coherence. Figure 6.8 shows two-colour differential reflection measurements, where we use low-power pump and probe laser excitation ($s = 0.05$ for each laser). The probe is kept on resonance and the suppressed pump is scanned across the resonance. The contrast measured is proportional to $\frac{|\rho 13|}{\sqrt{s_{probe}}}$ and a drop in contrast indicates a sub-linearity of the response (c.f Fig. 3.4). In the center of the charging plateau, the contrast drops to $\approx 83\%$ of the single-laser value at the TPR condition, whereas in the cotunneling regime it drops to $\approx 96\%$, corresponding to the expected saturation behaviour for these powers. For the

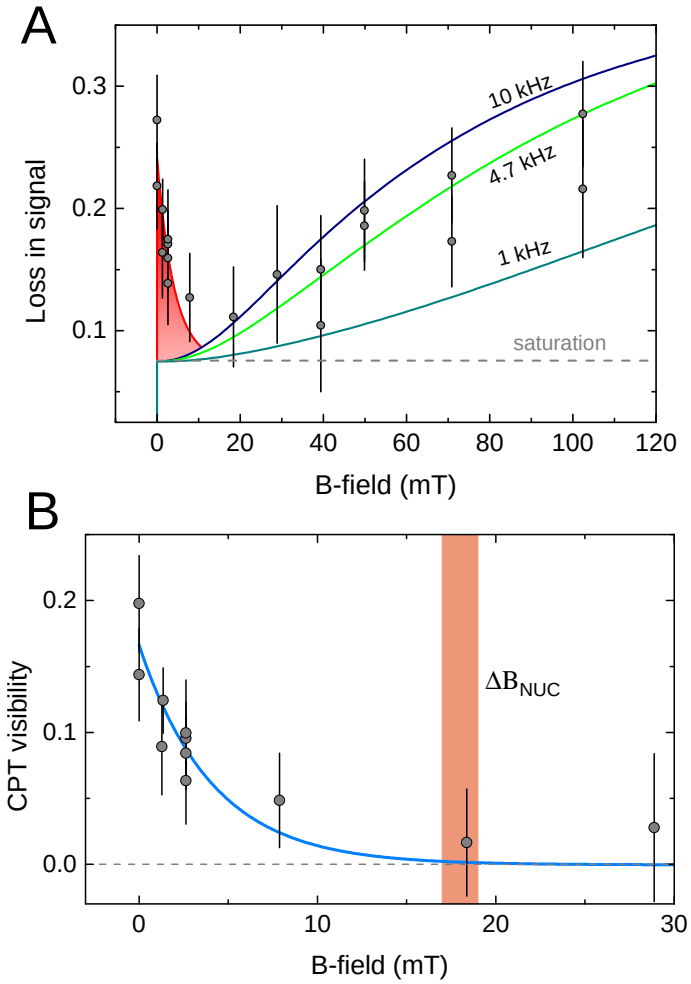

Fig. 6.7 **A.** Sub-linearity in QD fluorescence (grey circles) measured at equal laser frequencies. The blue, light green and dark green curves are simulations taking into account incoherent spin pumping and saturation for different values of spin relaxation rate shown as labelled. The dashed grey line shows the B-field-independent contribution from saturation alone. The red area is an exponential fit and represents the loss in signal not accounted for by saturation and spin pumping, corresponding to CPT. **B.** Decay of the CPT visibility obtained by subtracting the light green curve in panel **A** from the data. The blue curve shows an exponential fit, and the measured OH field dispersion to within $\pm 1\sigma$ is shown as an orange area. The error bars are calculated by propagation of the min-max values of count rates obtain at the TPR, and the standard error in best fit amplitudes of fits to single-laser lineshapes.

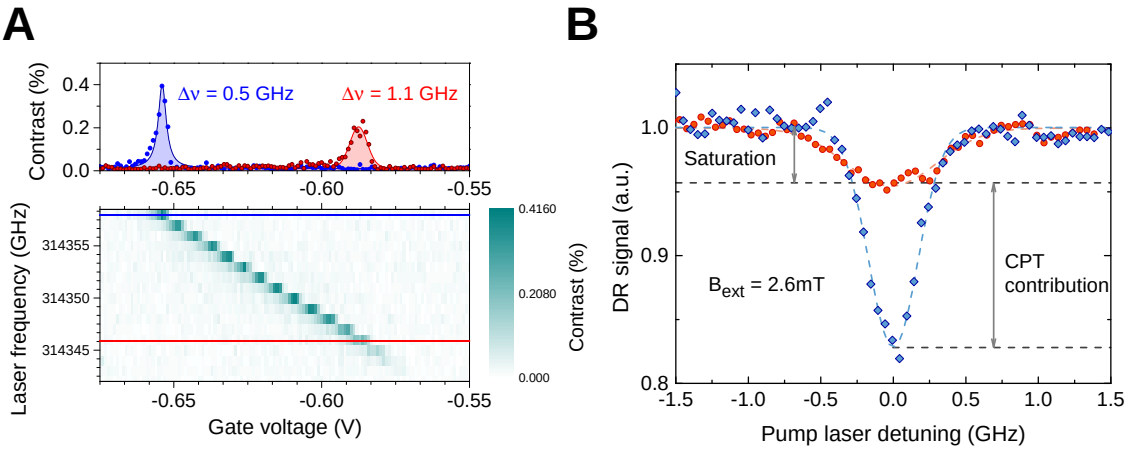

Fig. 6.8 **A.** Single-laser differential reflection measurement for different applied gate voltages near the cotunneling region. The left panel shows two scans taken far from (blue circles) and close to (red circles) the cotunneling region, at laser frequencies corresponding to the blue and red lines in the bottom panel. The solid curves are Voigt fits with best fit FWHM as displayed. **B.** Two-colour differential reflection measurement as a function of pump laser detuning for the two gate voltage positions shown in panel **A**. Both pump and probe laser are set to $s = 0.05$, and the pump reflection is suppressed. The curves are normalised to the mean value far away from pump resonance. The upper dashed grey line shows the expected loss in signal arising from saturation alone at these driving powers.

magnetic field used, we wouldn't expect optical spin pumping to contribute significantly to the sub-linearity. Therefore, this measurement indicates that the extra term leading to a sub-linearity is linked to the electron spin coherence, consistent with hyperfine-enabled CPT.

6.4 Spin Control via Phase Modulation

In the previous section, we have shown that the hyperfine interaction allows for the steady-state preparation of electron spin superpositions of the form:

$$|\psi\rangle \propto \alpha\,|\uparrow, \hat{\mathbf{n}}(t)\rangle - \beta e^{i\phi}\,|\downarrow, \hat{\mathbf{n}}(t)\rangle \tag{6.12}$$

where the unit vector $\hat{\mathbf{n}}(t)$ is defined by the instantaneous orientation of the adiabatically evolving OH field, $\uparrow$ and $\downarrow$ are electron spin projections along $\hat{\mathbf{n}}(t)$, α and β are effective Rabi frequencies and ϕ depends on the relative phase between the lasers. This state and its orthogonal ground state span the dressed basis. It is well known that the polar angle of the dark state within the ground state Bloch sphere is given by the ratio of Rabi frequencies. This fact forms the basis of stimulated Raman adiabatic passage [127]. However, the created dark state also depends on the relative phase between the two driving fields, which determines the azimuthal angle within the Bloch sphere. Adiabatically changing the phase then coherently rotates the electron spin in the OH field basis. However, we do not have access to high fidelity spin readout with such low magnetic fields and therefore cannot demonstrate such coherent rotations. Instead, to expose the optical phase dependence of the dark state, we impose a non-adiabatic phase jump after preparing a dark state and measure its effect on the time-resolved QD fluorescence. This rapid phase manipulation leads to a new rotated dressed basis in which the electron spin gains a finite bright state component, thereby generating fluorescence. Subsequent photon emission pumps the electron spin into the new dark state.

Figure 6.9 shows the experimental setup used to evidence the phase dependence of the dark state. In order to maximise the mutual coherence of the driving fields, we use a single laser which we separate into two beams. One beam is sent through an acousto-optic modulator (AOM). We use the first order diffraction, which is frequency shifted by the AOM driving frequency (80MHz). The second beam is sent through an electro-optic modulator (EOM) which provides a phase offset proportional to the applied voltage. The EOM used has a bandwidth of ≈ 20 GHz, meaning that in practice our experimental bandwidth is limited by the voltage supply. The two beams are then combined on a polarising beam-splitter and sent to the cryostat. Voltage pulses with a rise-time of ≈ 2 ns are sent to the EOM in order to impart a rapid phase jump. In the absence of an external magnetic field, the selection

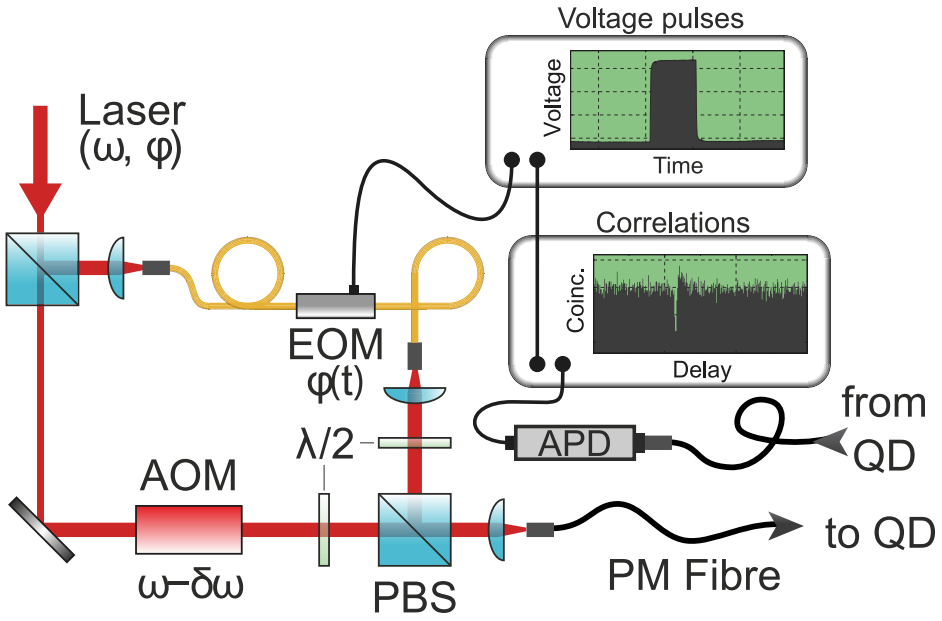

Fig. 6.9 Experimental setup used to measure time-resolved correlations between fast phase shifts and QD absorption. A single laser is split into two paths, one frequency shifted with an acousto-optic modulator (AOM), and the other phase-shifted with an electro-optic modulator (EOM). Single photon detection events are correlated with voltage pulses sent to the EOM. PBS: polarising beam-splitter; APD: avalanche photodiode; $\lambda/2$: half-wave plate.

rules evolve according to the OH field, therefore the lasers do not address a single transition selectively and a relative phase of the lasers is not necessarily mapped directly to a relative phase of the Rabi frequencies. We therefore apply a small (8.4 mT) magnetic field to split the excited states and ensure that the applied phase shift affects only one of the Rabi frequencies. The added contribution to the electron spin splitting then roughly matches the detuning between lasers, and the TPR condition is approximately met.

Figure 6.10 shows an example time-resolved fluorescence measurement, correlated with a rapid phase shift for laser powers of $s_{\mathrm{EOM}} = 0.2$ and $s_{\mathrm{AOM}} = 0.05$. In this case most of the response is due to the phase-controlled laser, and we can therefore take a comparable background measurement by blocking the frequency-shifted laser. However, the imbalance in powers leads to dark states with a finite z-projection (in the OH dictated basis), which will consequently limit the maximum bright state overlap induced by the phase pulse.
Two features can be observed in the measurement: a sharp dip correlated with the falling edge of the phase pulse, and a small increase in fluorescence thereafter. The former effect is due to the finite fall-time of the voltage pulses sent to the EOM, leading to a frequency shift (middle panel) which tunes the laser off-resonance for a finite time. After the phase pulse, we see an increase in fluorescence which decays on a timescale of order 10 ns, corresponding

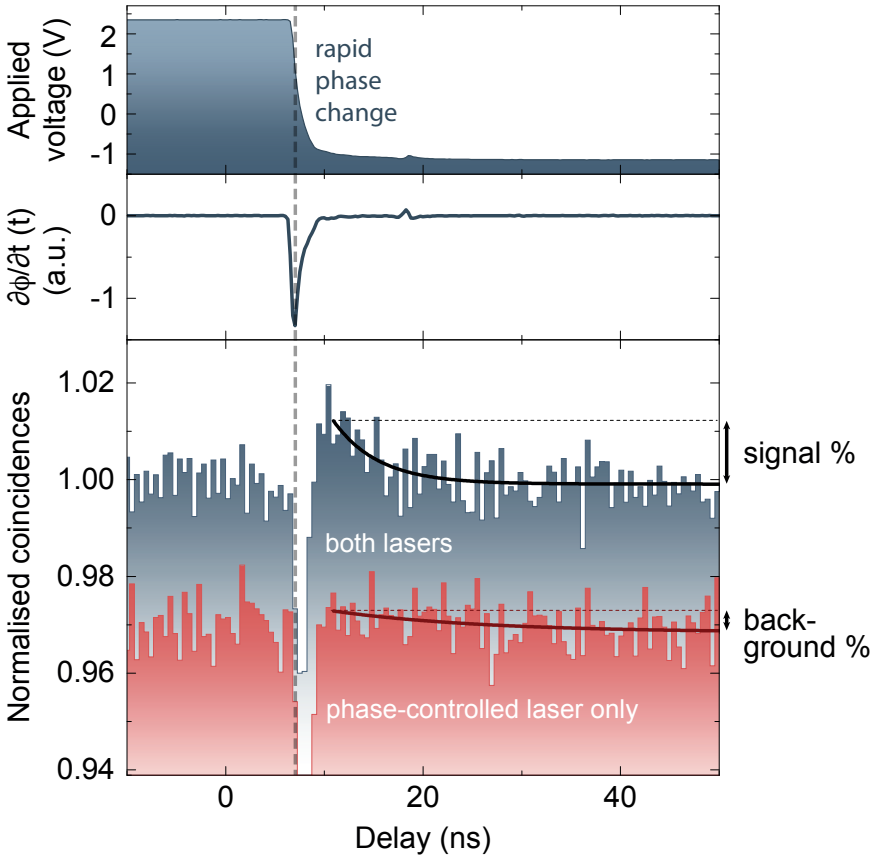

Fig. 6.10 Example time-resolved QD fluorescence measurement (lower panel) with the AOM path blocked (unblocked) shown as blue (red) columns. Both measurements are normalised to their long-time mean, but the red data are offset for clarity. The upper panel shows the measured voltage pulse sent to the EOM showing a fall time of ≈ 2 ns. The middle panel shows the derivative of the upper panel and corresponds to an instantaneous frequency shift of the driving laser, which correlates with a decrease in QD fluorescence. After the ≈ 2 ns long dip, the data in the bottom panel are fit with an exponential decay, for which the best fit amplitude quantifies the intermittent fluorescence intensity.

to a few optical cycles at this power. An increase in fluorescence on this timescale is not seen in the single-laser reference measurement, indicating that the feature is indeed related to the creation of a bright state component. A smaller increase in fluorescence decaying on a significantly longer timescale is observed in the reference measurement, related to the EOM response to the voltage pulses. We fit both curves, starting ≈ 2 ns after the dip, with exponential decays and record the best fit amplitude. We subtract the single-laser value from the two-laser measurement to quantify the intermittent fluorescence amplitude linked to the creation of a bright state component.

Figure 6.11 shows a summary of extracted best fit amplitudes for the two-laser and single-laser measurements. The single-laser measurements show a quadratic dependence on voltage pulse amplitude, suggesting an effect linearly dependent on driving power. In contrast, the two-laser measurement shows a consistently higher signal with a voltage dependence which is not a simple quadratic. Subtracting the quadratic fit to the reference measurements we obtain the background-subtracted data shown in panel C. The non-monotonic dependence on pulse amplitude is well fit with a sinusoidal behaviour, which is consistent with phase-induced rotations of the dressed basis. The maximum signal of $\approx 0.75\%$ results from a combination of low CPT visibility in a time-averaged measurement ($\approx 17\%$) which is further reduced with the application of a small magnetic field ($\approx 3-5\%$ at 8.4 mT, c.f. Fig. 6.7) and the imbalanced power ratio reducing the maximum phase-induced overlap with the bright state. Furthermore, the sharp dip caused by the finite fall-time of the EOM obscures the peak in fluorescence leading to a further decrease in signal. Panel A shows a sketch of the effect of phase pulses in this system. First the spin is initialised into the dark state, and the phase pulse leads to a rotation of the bright/dark basis (blue line) about the z-axis in the OH dictated quantisation axis. The electron spin does not follow the rotation adiabatically and therefore has a finite overlap with the new bright state. Thereafter, the QD fluoresces with an intensity proportional to this bright state component and is pumped into the new dark state within a few optical cycles. The protocol therefore allows for incoherent rotation of the prepared spin state, within the basis given by the OH field. Along with control of relative laser powers, this gives access to arbitrary spin state preparation in the nuclear basis. We note that, although arbitrary preparation of spin states can be done in the Bloch sphere given by $\hat{\mathbf{n}}(t)$, we do not know the instantaneous orientation of the OH field. However, this lack of knowledge does not lead to dephasing in a time-averaged protocol, in contrast to working in a fixed lab frame, as the OH field evolves quasi-statically.

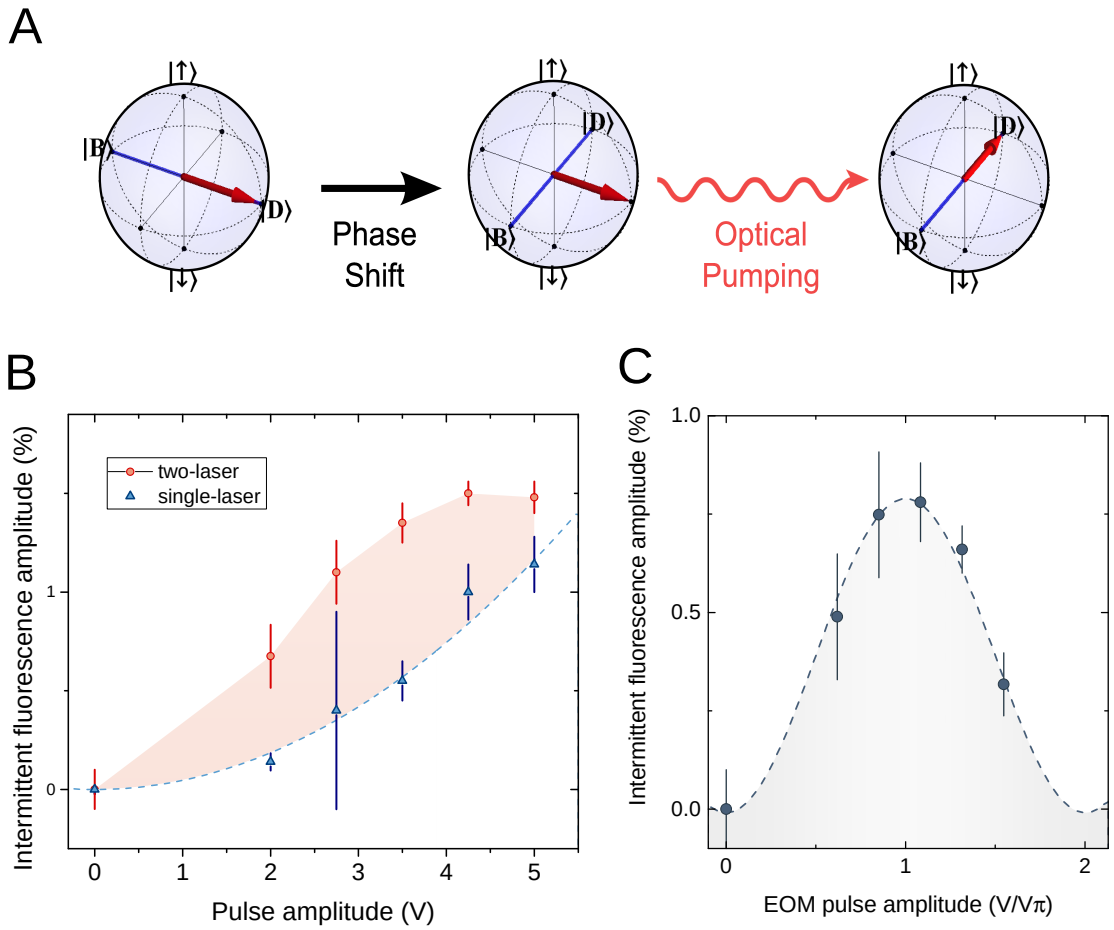

Fig. 6.11 **A.** Representation of the effect of a laser phase shift on the electron spin state (red arrow) in the Bloch sphere representing the ground state manifold. Before the phase shift, the electron spin is prepared in the dark state. The phase shift rotates the dark/bright basis (blue line) in the bare basis. The electron is then projected onto the new dark/bright basis, and the fluorescence intensity is proportional to its overlap with the new bright state. **B.** Summary of intermittent fluorescence amplitude for different Voltage pulse amplitudes. The orange circles show the data with both paths unblocked, and the blue triangles show the data with the AOM path blocked. The dashed curve is a quadratic fit to the data. **C.** Background-corrected intermittent fluorescence amplitude, obtained by subtracting the dashed curve from the orange circles in panel **B**. The x-axis is rescaled such that the sine fit has a period of 2π. The error bars represent the standard deviation in correlation rates and are limited by shot noise.

Chapter 7

Conclusion

7.1 Summary and Outlook

In this thesis, we have discussed the impact of the environment on the spin and optical properties of a solid-state atom-like system. The results presented in chapter 3 show that, in many respects, the neutral exciton transition of a QD behaves much like an ideal two-level atomic transition. Many of the predictions of resonance fluorescence from a well-isolated quantum emitter are verified in this mesoscopic solid-state emitter, namely the transition from coherent to incoherent scattering regimes along with coherent Rabi oscillations and robust photon antibunching.

Two inconsistencies with the two-level picture emerge due to interactions with the solid-state environment. Firstly, charge fluctuations in the host semiconductor matrix lead to a time-averaged random distribution of transition frequencies. Secondly, exciton-phonon coupling leads to phonon-assisted fluorescence. These effects lead to broadening of the emission spectrum and consequently to photonic distinguishability, posing a challenge in view of using QDs as spin-photon interfaces. In chapter 4 we demonstrated a technique which makes use of the phonon-assisted emission as a probe of frequency fluctuations caused by charge dynamics in the environment. This probe is then used to narrow the zero-phonon line by feedback stabilisation on the gate voltage. The inhomogeneous broadening on a sub-Hz timescale is reduced by at least a factor of 7, which should allow a significant improvement in fidelities of operations requiring photonic interference from different emitters in uncorrelated environments. Furthermore, the intensity noise characteristics in resonance fluorescence are improved by a factor of 22 with a stabilisation bandwidth of 190 Hz.

However, there are several noise sources affecting the QD transition at faster timescales [73, 77, 87]. In order to obtain transform-limited emission, a stabilisation bandwidth of ≈ 50 kHz [73] would be required. The stabilisation bandwidth of the protocol shown here

is limited both by the collection efficiency and by the gate bandwidth. Electrical gates with bandwidths up to GHz have been demonstrated [94] in samples with similar optically active QDs. The limiting factor then is photon extraction efficiency from the sample. In the sample used here, with a cubic Zirconia SIL and a DBR below the QD layer, the fraction of emission collected by the objective lens is around 6%. Fortunately, the MBE process required for the growth of optically-active QDs is readily compatible with the creation of complex heterostructures and lithography techniques. Various cavity QED structures have been demonstrated with QD emitters [78, 79, 128, 129], which can improve photon extraction efficiencies while being compatible with a gated structure [130]. Improvements in collection efficiency in a broadband structure are also possible [93], with collection efficiencies up to $\approx 99\%$ predicted with a dielectric antenna structure [91, 92].
Such an improvement in collection efficiency would certainly allow for the complete suppression of charge noise affecting the QD emission. We can speculate on whether or not nuclear spin fluctuations can also be fully suppressed with this protocol, assuming certain technical advancements. Firstly, moving from the Si APDs used here with detection efficiencies of $\approx 20\%$ to superconducting nanowire single photon detectors with detection efficiencies reaching 90% [131] would provide a four-fold improvement in stabilisation bandwidth. We can further speculate that an order of magnitude improvement in collection of the QD emission into the objective may be feasible with a dielectric antenna structure. Consequently, phonon-assisted stabilisation bandwidths of order 10 kHz may be possible. Further improvement could be obtained through a higher modulation amplitude or by sampling part of the ZPL, although both of these would lead to a loss of indistinguishable QD emission. It therefore seems that such a stabilisation scheme may be able to correct for the slowest components of nuclear spin noise, arising from nuclear spin diffusion outside the QD [28] on a timescale of ms, but the fastest timescales linked to nuclear spin precession in the Knight field ($< 100\ \mu s$) may be out of reach.

In chapter 5, we showed first and second order coherence measurements of resonance fluorescence from a negatively charged QD, in the low magnetic field regime. The second-order correlation shows bunching on a timescale of tens of ns, with a sub-linewidth detuning dependence. These observations point towards a hyperfine electron spin splitting in the absence of a magnetic field. Furthermore, the optical spin pumping timescale of tens of ns shows that the Faraday-like selection rules are broken by the hyperfine interaction, and spin-flip Raman transitions are dipole allowed. Emission spectra in the low power limit show deviations from a simple two-level picture. In addition to a resolution-limited peak at the laser frequency, we observe symmetrically detuned sidebands arising from coherent Raman

transitions in the hyperfine-split four level system. The shape and size of these sidebands relative to the elastic peak provide a direct measurement of the time-averaged OH field distribution. In the absence of a magnetic field, this distribution is isotropic and Gaussian with a dispersion of ≈ 20 mT depending on the QD. The signal-to-noise ratio obtained in these measurements gives a standard error of ± 1 mT using the OH field dispersion as a fitting parameter. Under applied magnetic fields commensurate with the OH field dispersion, we further observe indications of nuclear spin polarisation counteracting the effect of the magnetic field on the electron spin splitting, in combination with increased nuclear spin fluctuations in the direction of the applied field. Using coherent Raman spectroscopy allows the measurement of fine features such as small degrees of anisotropy as well as sub-linewidth nuclear spin polarisation. This technique therefore has applications in the further study of nuclear spin physics in the low-magnetic field regime.

On a more speculative note, a high-resolution measurement of the coherent Raman sideband could serve as a form of nuclear spin narrowing. By conditioning on the detection of a photon at a given Raman detuning, a subsequent experiment relying on the electron spin coherence can be significantly improved. Indeed, the electron spin inhomogeneous dephasing time T_2^* is inversely related to the time-averaged dispersion of the OH field distribution. The question then is: how much can we narrow the OH field distribution by conditioning on a photon detection for a given FP width? In a 'frozen' nuclear spin configuration, the width of the Raman sideband is given by a combination of the FP linewidth and the optically-induced spin relaxation. Using low driving powers is then beneficial, but also reduces the detection rate of conditioning photons. The best FP alignment obtained here gives a transmission FWHM of 10 MHz, compared to an optically-induced relaxation rate of $\approx 2\pi \times 4$ MHz for a driving power of $s = 0.1$ (corresponding to the bunching decay rate of Fig 5.4). Conditioning on a Raman photon therefore reduces the OH field FWHM from ≈ 200 MHz to ≈ 10 MHz, as shown in Fig. 7.1 A. Such a conditioning measurement would also prepare an anisotropic distribution with an orientation predominantly in-plane, therefore providing a Lambda system with well-known ground state splitting. The OH field correlation time is of order 10 μs, much longer than the dark state initialisation time of order 10 ns (c.f. decay timescale of Fig. 6.10). Therefore, such a conditioning measurement should therefore significantly increase the visibility of subsequent coherent population trapping of the electron spin. Panel B shows a comparison between three-level CPT calculations for two different ground state dephasing rates. The green curve corresponds to the best fit dephasing rate fitting the coherent population trapping data of Fig. 6.6, corresponding to an empirical dephasing rate of $2\pi \times 26$ MHz, and the orange curve is the calculation with a 20-fold reduction in dephasing rate, representing the 20-fold reduction in OH field dispersion due to the conditioning measurement.

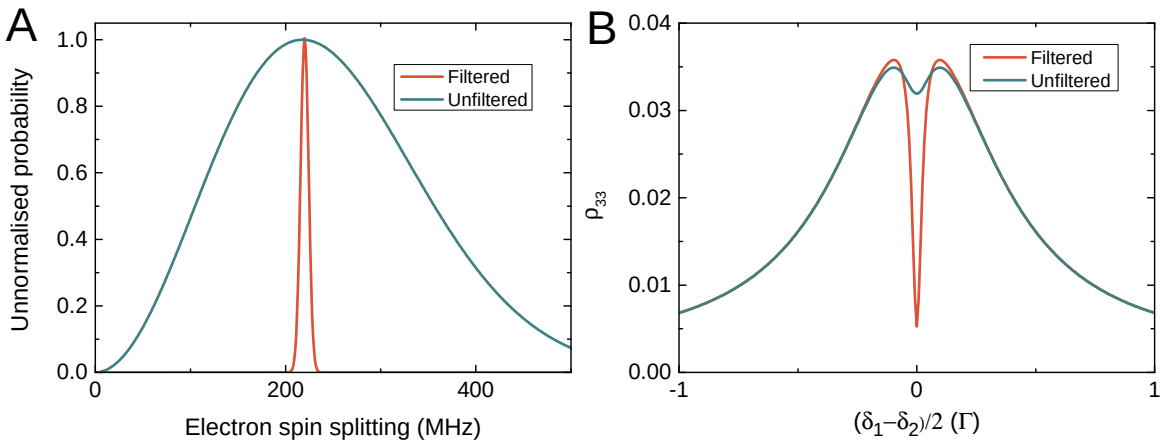

Fig. 7.1 **A.** The green curve shows the un-normalised ground state splitting distribution corresponding to the measured OH field dispersion of chapter 5. The orange curve shows the expected distribution after conditioning on the detection of a Raman photon for a FP cavity detuned by 220 MHz from the driving laser and a FP FWHM of 10 MHz. **B.** Simulated two-colour absorption spectrum as a function of two-photon detuning. The green curve is obtained with a ground state pure dephasing rate of 2.6 MHz, corresponding to the best fit of the data in chapter 6. The orange curve shows a simulation for a dephasing rate 20 times smaller, corresponding to the extent of the narrowing of the distribution in **A**.

Here we have assumed that the best fit dephasing rate of the three-level model is proportional to the OH field dispersion. The CPT visibility, and consequently the preparation fidelity, is predicted to increase significantly. As discussed in chapter 6, the three level model is incomplete for the trion system and we stress that the validity of the prediction of Fig. 7.1 is therefore limited. Indeed, this prediction ignores possible nuclear spin polarisation as well as the effect of the conditioning on the selection rules. Nevertheless, testing such a prediction would provide an interesting extension to the work shown in this thesis.

In chapter 6, we have shown that the hyperfine interaction provides a quantisation axis for the electron spin and adequate selection rules for optical spin control. Through two-colour excitation of the trion transition, we observe a sharp decrease in absorption at the two-photon resonance which is the spectroscopic signature of coherent population trapping. Furthermore, we have shown that control of the relative phase of the two driving fields allows the initialisation of the electron spin in an arbitrary superposition state in the basis dictated by the OH field. For an example of a possible extension of the work shown in chapter 6, in the following section we describe the proposal of Ref. [132] for generating long strings of entangled photons using the trion system in the low magnetic field regime.

7.2 Towards a Photonic Cluster-state Machine Gun

The DiVicenzo criteria mentioned in chapter 1 describe the necessary conditions a qubit must satisfy in order to provide an adequate building block for a quantum computer. These criteria explicitly follow the circuit model of quantum computation. Another model of quantum computation has been developed over the past decade based on using strings of photons entangled in so-called cluster states [133], or more generally graph states [48]. In this protocol, quantum computation can be achieved by measuring single photons from the cluster state, the result of which is fed forward to choose the basis for the following measurement. This protocol is called one-way quantum computation as the initial resource is destroyed throughout the process. One-way computation, including classical feed-forward, has been demonstrated experimentally [134], providing a proof-of-principle for the use of graph states. However, so far the initial states have been generated with parametric down-conversion. This technique is fundamentally probabilistic and the generated state inherits the Poisson statistics of the pump laser, therefore requiring low driving powers in order to minimise multi-photon events. Therefore, a more scalable method for photonic cluster-state generation would be highly desirable.

One such proposal [132] involves using a negatively charged QD, and its spin-photon entanglement properties [18–20] to generate large cluster states. By periodic excitation of the trion transition, multiple subsequently emitted photons can be entangled via the electron spin. Two circularly polarised transitions are allowed between $|\uparrow\rangle$ and $|\Uparrow\rangle$, or $|\downarrow\rangle$ and $|\Downarrow\rangle$ (c.f Fig. 1.3). If the electron spin is initially prepared in a superposition state, say $|\uparrow\rangle + |\downarrow\rangle$, and is subsequently excited with a linearly polarised optical pulse (broadband compared with the spin splittings), subsequent recombination leads to an entangled spin-photon state: $|\uparrow,\sigma_+\rangle + |\downarrow,\sigma_-\rangle$. Further photon scattering from this state would lead to a GHZ-type state. In order to obtain a cluster state, a unitary operation must be applied to the electron spin between scattering events. The Larmor precession of the spin in the magnetic field oriented along the y-direction can provide such an operation. For instance, if the time between exciting pulses corresponds to a quarter of the precession period, the state before the second scattering event is: $(|\uparrow\rangle + |\downarrow\rangle)|\sigma_+\rangle + (|\downarrow\rangle - |\uparrow\rangle)|\sigma_-\rangle$. After a second scattering event and another quarter period rotation, the full state becomes:

$$\begin{aligned} &|\uparrow,\sigma_+,\sigma_+\rangle + |\downarrow,\sigma_+,\sigma_+\rangle + |\downarrow,\sigma_-,\sigma_+\rangle - |\uparrow,\sigma_-,\sigma_+\rangle \\ &+ |\downarrow,\sigma_-,\sigma_-\rangle - |\uparrow,\sigma_-,\sigma_-\rangle - |\uparrow,\sigma_+,\sigma_-\rangle - |\uparrow,\sigma_+,\sigma_-\rangle \end{aligned} \tag{7.1}$$

which is a 3-qubit cluster state for a logical encoding of $|\uparrow\rangle \equiv 1$, $|\downarrow\rangle \equiv 0$, $|\sigma_+\rangle \equiv 0$, and $-|\sigma_-\rangle \equiv 1$. This procedure can ideally be repeated for a time limited by the coherence time

of the electron spin, and long strings of photons can in principle be generated. Furthermore, this protocol is relatively insensitive to inhomogeneous broadening of the transition compared with a 'quantum internet' architecture composed of different QDs. The electron spin can then be disentangled from the photonic string with a measurement in the computational basis. Relying on Larmor precession for the intermediate operations leads to a complication: the finite lifetime of the excited state (in which the Larmor precession is different from the ground states) leads to errors in the created cluster state. Therefore, a Larmor precession period slower than the excited state lifetime is required, or equivalently, the electron spin splitting has to be sub-linewidth. This is where the work shown in this thesis relates to this proposal. In chapter 6, we have demonstrated a method for the preparation of an electron spin superposition state in the low-magnetic field regime, thus satisfying the requirement for a sub-linewidth spin splitting. As discussed in the previous section, the fidelity of the dark state initialisation may be significantly improved by conditioning on the detection of a Raman photon. Furthermore, the uncertainty in Larmor precession is no longer determined by the full extent of the OH field distribution but by the FP resolution. This leaves us with the final electron spin readout. To achieve this, a high-power σ_+-polarised detuned laser pulse could be used to modify the hyperfine level structure to recover Faraday-like selection rules through the AC Stark effect. The effective Faraday geometry would then allow a measurement of the electron spin in the computational basis. The electron spin splitting due to the OH field is of order 100 MHz, compared with AC Stark shifts of several tens of GHz which have been used for ultrafast spin control [135]. Therefore, the created level structure can be made to resemble the Faraday geometry to a good degree.

Demonstrating such a protocol will not be trivial, and we expect some rather daunting technical difficulties to arise. First and foremost, an alternative to the cross-polarisation technique used throughout the thesis will be needed, as the qubits are encoded in the photon polarisation. Using a time-window may allow the suppression of the laser background to some extent, but further technical improvements in excitation efficiency will probably be needed to achieve a reasonable signal-to-background ratio. Secondly, the conditioning scheme requires sampling part of the emission and is therefore a significant source of photon loss while the limited transmission efficiency of the FP will lead to long waiting times for the conditioning photon.

References

[1] A. Tartakovskii, *Quantum Dots: Optics, Electron Transport and Future Applications*. Quantum Dots: Optics, Electron Transport, and Future Applications, Cambridge University Press, 2012.

[2] O. Schmidt, *Lateral Alignment of Epitaxial Quantum Dots*. NanoScience and Technology, Deutsches MAB-Nationalkomitee beim Bundesministerium für Umwelt, Naturschutz und Reaktorsicherheit, 2007.

[3] J. M. Luttinger, "Quantum theory of cyclotron resonance in semiconductors: General theory," *Phys. Rev.*, vol. 102, pp. 1030–1041, May 1956.

[4] M. Bayer, G. Ortner, O. Stern, A. Kuther, A. A. Gorbunov, A. Forchel, P. Hawrylak, S. Fafard, K. Hinzer, T. L. Reinecke, S. N. Walck, J. P. Reithmaier, F. Klopf, and F. Schäfer, "Fine structure of neutral and charged excitons in self-assembled In(Ga)As/(Al)GaAs quantum dots," *Phys. Rev. B*, vol. 65, p. 195315, May 2002.

[5] R. J. Warburton, C. Schulhauser, D. Haft, C. Schäflein, K. Karrai, J. M. Garcia, W. Schoenfeld, and P. M. Petroff, "Giant permanent dipole moments of excitons in semiconductor nanostructures," *Phys. Rev. B*, vol. 65, p. 113303, Feb 2002.

[6] M. Atatüre, J. Dreiser, A. Badolato, A. Högele, K. Karrai, and A. Imamoglu, "Quantum-dot spin-state preparation with near-unity fidelity," *Science*, vol. 312, no. 5773, pp. 551–553, 2006.

[7] D. Press, T. D. Ladd, B. Zhang, and Y. Yamamoto, "Complete quantum control of a single quantum dot spin using ultrafast optical pulses," *Nature*, vol. 456, pp. 218–221, Nov. 2008.

[8] D. P. DiVicenzo, "The physical implementation of quantum computation," *arxiv.org/pdf/quant-ph/0002077*, 2000.

[9] M. Kroutvar, Y. Ducommun, D. Heiss, M. Bichler, D. Schuh, G. Abstreiter, and J. J. Finley, "Optically programmable electron spin memory using semiconductor quantum dots," *Nature*, vol. 432, pp. 81–84, Nov. 2004.

[10] C.-Y. Lu, Y. Zhao, A. N. Vamivakas, C. Matthiesen, S. Fält, A. Badolato, and M. Atatüre, "Direct measurement of spin dynamics in InAs/GaAs quantum dots

using time-resolved resonance fluorescence," *Phys. Rev. B*, vol. 81, p. 035332, Jan 2010.

[11] X. Xu, Y. Wu, B. Sun, Q. Huang, J. Cheng, D. G. Steel, A. S. Bracker, D. Gammon, C. Emary, and L. J. Sham, "Fast spin state initialization in a singly charged InAs-GaAs quantum dot by optical cooling," *Phys. Rev. Lett.*, vol. 99, p. 097401, Aug 2007.

[12] E. D. Kim, K. Truex, X. Xu, B. Sun, D. G. Steel, A. S. Bracker, D. Gammon, and L. J. Sham, "Fast spin rotations by optically controlled geometric phases in a charge-tunable InAs quantum dot," *Phys. Rev. Lett.*, vol. 104, p. 167401, Apr 2010.

[13] J. Preskill, "Reliable quantum computers," *Proceedings of the Royal Society of London A: Mathematical, Physical and Engineering Sciences*, vol. 454, no. 1969, pp. 385–410, 1998.

[14] A. Bechtold, D. Rauch, T. Simmet, P.-L. Ardelt, A. Regler, K. Müller, and J. J. Finley, "Hyperfine mediated electron spin relaxation in a single InGaAs quantum dot at low magnetic fields," *arXiv:1410.4316v1*, 2014.

[15] A. N. Vamivakas, C.-Y. Lu, C. Matthiesen, Y. Zhao, S. Falt, A. Badolato, and M. Atatüre, "Observation of spin-dependent quantum jumps via quantum dot resonance fluorescence," *Nature*, vol. 467, pp. 297–300, Sept. 2010.

[16] J. Berezovsky, M. H. Mikkelsen, O. Gywat, N. G. Stoltz, L. A. Coldren, and D. D. Awschalom, "Nondestructive optical measurements of a single electron spin in a quantum dot," *Science*, vol. 314, no. 5807, pp. 1916–1920, 2006.

[17] S. Puri, P. L. McMahon, and Y. Yamamoto, "Single-shot quantum nondemolition measurement of a quantum-dot electron spin using cavity exciton-polaritons," *Phys. Rev. B*, vol. 90, p. 155421, Oct 2014.

[18] W. B. Gao, P. Fallahi, E. Togan, J. Miguel-Sanchez, and A. Imamoglu, "Observation of entanglement between a quantum dot spin and a single photon," *Nature*, vol. 491, pp. 426–430, Nov. 2012.

[19] K. De Greve, L. Yu, P. L. McMahon, J. S. Pelc, C. M. Natarajan, N. Y. Kim, E. Abe, S. Maier, C. Schneider, M. Kamp, S. Hofling, R. H. Hadfield, A. Forchel, M. M. Fejer, and Y. Yamamoto, "Quantum-dot spin-photon entanglement via frequency downconversion to telecom wavelength," *Nature*, vol. 491, pp. 421–425, Nov. 2012.

[20] J. R. Schaibley, A. P. Burgers, G. A. McCracken, L.-M. Duan, P. R. Berman, D. G. Steel, A. S. Bracker, D. Gammon, and L. J. Sham, "Demonstration of quantum entanglement between a single electron spin confined to an InAs quantum dot and a photon," *Phys. Rev. Lett.*, vol. 110, p. 167401, Apr 2013.

[21] H. J. Kimble, "The quantum internet," *Nature (London)*, vol. 453, pp. 1023–1030, 2008.

[22] A. W. Overhauser, "Polarization of nuclei in metals," *Phys. Rev.*, vol. 92, pp. 411–415, Oct 1953.

[23] G. Lampel, "Nuclear dynamic polarization by optical electronic saturation and optical pumping in semiconductors," *Phys. Rev. Lett.*, vol. 20, pp. 491–493, Mar 1968.

[24] I. A. Merkulov, A. L. Efros, and M. Rosen, "Electron spin relaxation by nuclei in semiconductor quantum dots," *Phys. Rev. B*, vol. 65, p. 205309, Apr 2002.

[25] D. Press, K. De Greve, P. L. McMahon, T. D. Ladd, B. Friess, C. Schneider, M. Kamp, S. Hofling, A. Forchel, and Y. Yamamoto, "Ultrafast optical spin echo in a single quantum dot," *Nat Photon*, vol. 4, pp. 367–370, June 2010.

[26] A. Högele, M. Kroner, C. Latta, M. Claassen, I. Carusotto, C. Bulutay, and A. Imamoglu, "Dynamic nuclear spin polarization in the resonant laser excitation of an InGaAs quantum dot," *Phys. Rev. Lett.*, vol. 108, p. 197403, May 2012.

[27] B. Urbaszek, X. Marie, T. Amand, O. Krebs, P. Voisin, P. Maletinsky, A. Högele, and A. Imamoglu, "Nuclear spin physics in quantum dots: An optical investigation," *Rev. Mod. Phys.*, vol. 85, pp. 79–133, Jan 2013.

[28] E. Chekhovich, M. Hopkinson, M. Skolnick, and A. Tartakovskii, "Suppression of nuclear spin bath fluctuations in self-assembled quantum dots induced by inhomogeneous strain," *Nat Commun*, vol. 6, p. 6348, Feb. 2015.

[29] P. Maletinsky, A. Badolato, and A. Imamoglu, "Dynamics of quantum dot nuclear spin polarization controlled by a single electron," *Phys. Rev. Lett.*, vol. 99, p. 056804, Aug 2007.

[30] O. Krebs, B. Eble, A. Lemaître, P. Voisin, B. Urbaszek, T. Amand, and X. Marie, "Hyperfine interaction in InAs/GaAs self-assembled quantum dots: dynamical nuclear polarization versus spin relaxation," *Comptes Rendus Physique*, vol. 9, pp. 874–884, Oct. 2008.

[31] C. Latta, A. Hogele, Y. Zhao, A. N. Vamivakas, P. Maletinsky, M. Kroner, J. Dreiser, I. Carusotto, A. Badolato, D. Schuh, W. Wegscheider, M. Atature, and A. Imamoglu, "Confluence of resonant laser excitation and bidirectional quantum-dot nuclear-spin polarization," *Nat Phys*, vol. 5, pp. 758–763, Oct. 2009.

[32] C.-W. Huang and X. Hu, "Theoretical study of nuclear spin polarization and depolarization in self-assembled quantum dots," *Phys. Rev. B*, vol. 81, p. 205304, May 2010.

[33] W. Yang and L. J. Sham, "Collective nuclear stabilization in single quantum dots by noncollinear hyperfine interaction," *Phys. Rev. B*, vol. 85, p. 235319, Jun 2012.

[34] E. A. Chekhovich, M. N. Makhonin, A. I. Tartakovskii, A. Yacoby, H. Bluhm, K. C. Nowack, and L. M. K. Vandersypen, "Nuclear spin effects in semiconductor quantum dots," *Nat Mater*, vol. 12, pp. 494–504, June 2013.

[35] M. Munsch, G. Wüst, A. V. Kuhlmann, F. Xue, A. Ludwig, D. Reuter, A. D. Wieck, M. Poggio, and R. J. Warburton, "Manipulation of the nuclear spin ensemble in a quantum dot with chirped magnetic resonance pulses," *Nat Nano*, vol. 9, pp. 671–675, Sept. 2014.

[36] W. Gao, P. Fallahi, E. Togan, A. Delteil, Y. Chin, J. Miguel-Sanchez, and A. Imamoglu, "Quantum teleportation from a propagating photon to a solid-state spin qubit," *Nature Communications*, vol. 4, p. 2744, 2013.

[37] C. Matthiesen, M. Geller, C. H. H. Schulte, C. L. Gall, J. Hansom, Z. Li, M. Hugues, E. Clarke, and M. Atatüre, "Phase-locked indistinguishable photons with synthesized waveforms from a solid-state source," *Nature Communications*, vol. 4, p. 1600, 2013.

[38] K. Konthasinghe, M. Peiris, Y. Yu, M. F. Li, J. F. He, L. J. Wang, H. Q. Ni, Z. C. Niu, C. K. Shih, and A. Muller, "Field-field and photon-photon correlations of light scattered by two remote two-level InAs quantum dots on the same substrate," *Phys. Rev. Lett.*, vol. 109, p. 267402, Dec 2012.

[39] P. Lodahl, S. Mahmoodian, and S. Stobbe, "Interfacing single photons and single quantum dots with photonic nanostructures," *arXiv preprint*, vol. arXiv:1312.1079v1, 2013.

[40] N. Akopian, R. Trotta, E. Zallo, S. Kumar, P. Atkinson, A. Rastelli, O. G. Schmidt, and V. Zwiller, "An artificial atom locked to natural atoms," *arXiv preprint*, vol. arXiv:1302.2005v1, 2013.

[41] V. M. Acosta, C. Santori, A. Faraon, Z. Huang, K.-M. C. Fu, A. Stacey, D. A. Simpson, K. Ganesan, S. Tomljenovic-Hanic, A. D. Greentree, S. Prawer, and R. G. Beausoleil, "Dynamic stabilization of the optical resonances of single nitrogen-vacancy centers in diamond," *Phys. Rev. Lett.*, vol. 108, p. 206401, May 2012.

[42] J. H. Prechtel, A. V. Kuhlmann, J. Houel, L. Greuter, A. Ludwig, D. Reuter, A. D. Wieck, and R. J. Warburton, "Frequency-stabilized source of single photons from a solid-state qubit," *Phys. Rev. X*, vol. 3, p. 041006, Oct 2013.

[43] L. Besombes, K. Kheng, L. Marsal, and H. Mariette, "Acoustic phonon broadening mechanism in single quantum dot emission," *Phys. Rev. B*, vol. 63, p. 155307, Mar 2001.

[44] I. Favero, G. Cassabois, R. Ferreira, D. Darson, C. Voisin, J. Tignon, C. Delalande, G. Bastard, P. Roussignol, and J. M. Gérard, "Acoustic phonon sidebands in the emission line of single InAs/GaAs quantum dots," *Phys. Rev. B*, vol. 68, p. 233301, Dec 2003.

[45] H. Bernien, L. Childress, L. Robledo, M. Markham, D. Twitchen, and R. Hanson, "Two-photon quantum interference from separate nitrogen vacancy centers in diamond," *Phys. Rev. Lett.*, vol. 108, p. 043604, Jan 2012.

[46] E. Neu, D. Steinmetz, J. Riedrich-Möller, S. Gsell, M. Fischer, M. Schreck, and C. Becher, "Single photon emission from silicon-vacancy colour centres in chemical vapour deposition nano-diamonds on iridium," *New Journal of Physics*, vol. 13, no. 2, p. 025012, 2011.

[47] S. Buckley, K. Rivoire, and J. Vuckovic, "Engineered quantum dot single-photon sources," *Reports on Progress in Physics*, vol. 75, no. 12, p. 126503, 2012.

[48] P. Kok, W. J. Munro, K. Nemoto, T. C. Ralph, J. P. Dowling, and G. J. Milburn, "Linear optical quantum computing with photonic qubits," *Rev. Mod. Phys.*, vol. 79, pp. 135–174, Jan 2007.

[49] E. Knill, R. Laflamme, and G. J. Milburn, "A scheme for efficient quantum computation with linear optics," *Nature (London)*, vol. 409, pp. 46–52, 2001.

[50] B. Fröhlich, J. F. Dynes, M. Lucamarini, A. W. Sharpe, Z. Yuan, and A. J. Shields, "A quantum access network," *Nature (London)*, vol. 501, pp. 69–72, 2013.

[51] C. H. H. Schulte, J. Hansom, A. E. Jones, C. Matthiesen, C. L. Gall, and M. Atatüre, "Quadrature squeezed photons from a two-level system," *In preparation*, 2015.

[52] H. J. Carmichael, *Statistical Methods in Quantum Optics 1*. Springer, 1999.

[53] R. Loudon, *The Quantum Theory of Light (3rd edition)*. Oxford Science Publications, 2000.

[54] M. Scully and S. Zubairy, *Quantum Optics*. Cambridge University Press, 1997.

[55] P. Meystre and M. Sargent, *Elements of Quantum Optics*. SpringerLink: Springer e-Books, Springer, 2007.

[56] B. R. Mollow, "Power spectrum of light scattered by two-level systems," *Phys. Rev.*, vol. 188, pp. 1969–1975, Dec 1969.

[57] M. Hillery, R. O'Connell, M. Scully, and E. Wigner, "Distribution functions in physics: Fundamentals," *Physics Reports*, vol. 106, no. 3, pp. 121 – 167, 1984.

[58] H.-W. Lee, "Theory and application of the quantum phase-space distribution functions," *Physics Reports*, vol. 259, no. 3, pp. 147 – 211, 1995.

[59] E. Wigner, "On the quantum correction for thermodynamic equilibrium," *Phys. Rev.*, vol. 40, pp. 749–759, Jun 1932.

[60] W. P. Schleich, *Quantum Optics in Phase Space*. Wiley-VCH, 2001.

[61] W. B. Case, "Wigner functions and Weyl transforms for pedestrians," *American Journal of Physics*, vol. 76, no. 10, pp. 937–946, 2008.

[62] A. I. Lvovsky, H. Hansen, T. Aichele, O. Benson, J. Mlynek, and S. Schiller, "Quantum state reconstruction of the single-photon fock state," *Phys. Rev. Lett.*, vol. 87, p. 050402, Jul 2001.

[63] A. Ourjoumtsev, R. Tualle-Brouri, and P. Grangier, "Quantum homodyne tomography of a two-photon fock state," *Phys. Rev. Lett.*, vol. 96, p. 213601, Jun 2006.

[64] M. Stobińska, M. Sondermann, and G. Leuchs, "Prospect for detecting squeezed states of light created by a single atom in free space," *Optics Communications*, vol. 283, no. 5, pp. 737 – 740, 2010. Quo vadis Quantum Optics?

[65] H. J. Kimble, M. Dagenais, and L. Mandel, "Photon antibunching in resonance fluorescence," *Phys. Rev. Lett.*, vol. 39, pp. 691–695, Sep 1977.

[66] R. Short and L. Mandel, "Observation of sub-poissonian photon statistics," *Phys. Rev. Lett.*, vol. 51, pp. 384–387, Aug 1983.

[67] D. F. Walls and P. Zoller, "Reduced quantum fluctuations in resonance fluorescence," *Phys. Rev. Lett.*, vol. 47, pp. 709–711, Sep 1981.

[68] X. Xu, B. Sun, P. R. Berman, D. G. Steel, A. S. Bracker, D. Gammon, and L. J. Sham, "Coherent population trapping of an electron spin in a single negatively charged quantum dot," *Nat Phys*, vol. 4, pp. 692–695, Sept. 2008.

[69] S. M. Mansfield and G. S. Kino, "Solid immersion microscope," *Applied Physics Letters*, vol. 57, no. 24, pp. 2615–2616, 1990.

[70] S. B. Ippolito, B. B. Goldberg, and M. S. Ünlü, "High spatial resolution subsurface microscopy," *Applied Physics Letters*, vol. 78, no. 26, pp. 4071–4073, 2001.

[71] L. Novotny and B. Hecht, *Principles of Nano-Optics*. Cambridge University Press, 2006.

[72] B. Alèn, F. Bickel, K. Karrai, R. J. Warburton, and P. M. Petroff, "Stark-shift modulation absorption spectroscopy of single quantum dots," *Applied Physics Letters*, vol. 83, no. 11, pp. 2235–2237, 2003.

[73] A. V. Kuhlmann, J. Houel, A. Ludwig, L. Greuter, D. Reuter, A. D. Wieck, M. Poggio, and R. J. Warburton, "Charge noise and spin noise in a semiconductor quantum device," *Nature Physics*, vol. 9, pp. 570–575, 2013.

[74] C. Matthiesen, A. N. Vamivakas, and M. Atatüre, "Subnatural linewidth single photons from a quantum dot," *Phys. Rev. Lett.*, vol. 108, p. 093602, Feb 2012.

[75] P. Borri, W. Langbein, U. Woggon, V. Stavarache, D. Reuter, and A. D. Wieck, "Exciton dephasing via phonon interactions in inas quantum dots: Dependence on quantum confinement," *Phys. Rev. B*, vol. 71, p. 115328, Mar 2005.

[76] W. Vogel and D. Welsch, *Quantum Optics*. Wiley, 2006.

[77] M. J. Stanley, C. Matthiesen, J. Hansom, C. Le Gall, C. H. H. Schulte, E. Clarke, and M. Atatüre, "Dynamics of a mesoscopic nuclear spin ensemble interacting with an optically driven electron spin," *Phys. Rev. B*, vol. 90, p. 195305, Nov 2014.

[78] M. Pelton, C. Santori, J. Vuckovic, B. Zhang, G. S. Solomon, J. Plant, and Y. Yamamoto, "Efficient source of single photons: A single quantum dot in a micropost microcavity," *Phys. Rev. Lett.*, vol. 89, p. 233602, Nov 2002.

[79] P. Lodahl, A. Floris van Driel, I. S. Nikolaev, A. Irman, K. Overgaag, D. Vanmaekelbergh, and W. L. Vos, "Controlling the dynamics of spontaneous emission from quantum dots by photonic crystals," *Nature*, vol. 430, pp. 654–657, Aug. 2004.

[80] A. Dousse, J. Suffczynski, A. Beveratos, O. Krebs, A. Lemaitre, I. Sagnes, J. Bloch, P. Voisin, and P. Senellart, "Ultrabright source of entangled photon pairs," *Nature*, vol. 466, pp. 217–220, July 2010.

[81] Y.-M. He, Y. He, Y.-J. Wei, D. Wu, M. Atatüre, C. Schneider, S. Höfling, M. Kamp, C.-Y. Lu, and J.-W. Pan, "On-demand semiconductor single-photon source with near-unity indistinguishability," *Nature Nanotechnology*, vol. 8, pp. 213–217, 2013.

[82] O. Gazzano, S. M. de Vasconcellos, C. Arnold, A. Nowak, E. Galopin, I. Sagnes, L. Lanco, A. Lemaïtre, and P. Senellart, "Bright solid-state sources of indistinguishable single photons," *Nature Communications*, vol. 4, p. 1425, 2013.

[83] J. Hansom, C. H. H. Schulte, C. Matthiesen, M. J. Stanley, and M. Atatüre, "Frequency stabilization of the zero-phonon line of a quantum dot via phonon-assisted active feedback," *Applied Physics Letters*, vol. 105, no. 17, p. 172107, 2014.

[84] C. Matthiesen, M. J. Stanley, M. Hugues, E. Clarke, and M. Atatüre, "Full counting statistics of quantum dot resonance fluorescence," *Scientific Reports*, vol. 4, p. 4911, 2014.

[85] S. Kogan, *Electronic Noise and Fluctuations in Solids*. Cambridge University Press, 1996.

[86] J. Houel, A. V. Kuhlmann, L. Greuter, F. Xue, M. Poggio, B. D. Gerardot, P. A. Dalgarno, A. Badolato, P. M. Petroff, A. Ludwig, D. Reuter, A. D. Wieck, and R. J. Warburton, "Probing single-charge fluctuations at a GaAs/AlAs interface using laser spectroscopy on a nearby ingaas quantum dot," *Phys. Rev. Lett.*, vol. 108, p. 107401, Mar 2012.

[87] M. Davanco, C. S. Hellberg, S. Ates, A. Badolato, and K. Srinivasan, "Multiple time scale blinking in InAs quantum dot single-photon sources," *Phys. Rev. B*, vol. 89, p. 161303, Apr 2014.

[88] U. Bockelmann and G. Bastard, "Phonon scattering and energy relaxation in two-, one-, and zero-dimensional electron gases," *Phys. Rev. B*, vol. 42, pp. 8947–8951, Nov 1990.

[89] B. Krummheuer, V. M. Axt, and T. Kuhn, "Theory of pure dephasing and the resulting absorption line shape in semiconductor quantum dots," *Phys. Rev. B*, vol. 65, p. 195313, May 2002.

[90] P. Borri, W. Langbein, S. Schneider, U. Woggon, R. L. Sellin, D. Ouyang, and D. Bimberg, "Ultralong dephasing time in InGaAs quantum dots," *Phys. Rev. Lett.*, vol. 87, p. 157401, Sep 2001.

[91] K. G. Lee, X. W. Chen, H. Eghlidi, P. Kukura, R. Lettow, A. Renn, V. Sandoghdar, and S. Götzinger, "A planar dielectric antenna for directional single-photon emission and near-unity collection efficiency," *Nature Photonics*, vol. 5, pp. 166–169, 2011.

[92] X.-L. Chu, T. J. K. Brenner, X.-W. Chen, Y. Ghosh, J. A. Hollingsworth, V. Sandoghdar, and S. Götzinger, "Experimental realization of an optical antenna designed for collecting 99% of photons from a quantum emitter," *Optica*, vol. 1, pp. 203–208, Oct 2014.

[93] Y. Ma, P. E. Kremer, and B. D. Gerardot, "Efficient photon extraction from a quantum dot in a broad-band planar cavity antenna," *Journal of Applied Physics*, vol. 115, no. 2, p. 023106, 2014.

[94] A. J. Bennett, D. C. Unitt, P. See, A. J. Shields, P. Atkinson, K. Cooper, and D. A. Ritchie, "Electrical control of the uncertainty in the time of single photon emission events," *Phys. Rev. B*, vol. 72, p. 033316, Jul 2005.

[95] F. Hargart, C. A. Kessler, T. Schwarzbäck, E. Koroknay, S. Weidenfeld, M. Jetter, and P. Michler, "Electrically driven quantum dot single-photon source at 2 GHz excitation repetition rate with ultra-low emission time jitter," *Applied Physics Letters*, vol. 102, no. 1, p. 011126, 2013.

[96] J. Hansom, C. H. H. Schulte, C. Le Gall, C. Matthiesen, E. Clarke, M. Hugues, J. M. Taylor, and M. Atatüre, "Environment-assisted quantum control of a solid-state spin via coherent dark states," *Nat Phys*, vol. 10, pp. 725–730, Oct. 2014.

[97] J. Fischer, M. Trif, W. Coish, and D. Loss, "Spin interactions, relaxation and decoherence in quantum dots," *Solid State Communications*, vol. 149, pp. 1443–1450, Sept. 2009.

[98] A. Abragam, *The Principles of Nuclear Magnetism*. International series of monographs on physics, Clarendon Press, 1961.

[99] W. A. Coish and J. Baugh, "Nuclear spins in nanostructures," *phys. stat. sol. (b)*, vol. 246, no. 10, pp. 2203–2215, 2009.

[100] E. A. Chekhovich, M. M. Glazov, A. B. Krysa, M. Hopkinson, P. Senellart, A. Lemaitre, M. S. Skolnick, and A. I. Tartakovskii, "Element-sensitive measurement of the hole-nuclear spin interaction in quantum dots," *Nat Phys*, vol. 9, pp. 74–78, Feb. 2013.

[101] B. Eble, C. Testelin, P. Desfonds, F. Bernardot, A. Balocchi, T. Amand, A. Miard, A. Lemaître, X. Marie, and M. Chamarro, "Hole-nuclear spin interaction in quantum dots," *Phys. Rev. Lett.*, vol. 102, p. 146601, Apr 2009.

[102] P. Fallahi, S. T. Y ılmaz, and A. Imamoğlu, "Measurement of a heavy-hole hyperfine interaction in InGaAs quantum dots using resonance fluorescence," *Phys. Rev. Lett.*, vol. 105, p. 257402, Dec 2010.

[103] M. Bayer, O. Stern, A. Kuther, and A. Forchel, "Spectroscopic study of dark excitons in $In_xGa_{1-x}As$ self-assembled quantum dots by a magnetic-field-induced symmetry breaking," *Phys. Rev. B*, vol. 61, pp. 7273–7276, Mar 2000.

[104] C. E. Pryor and M. E. Flatté, "Landé g factors and orbital momentum quenching in semiconductor quantum dots," *Phys. Rev. Lett.*, vol. 96, p. 026804, Jan 2006.

[105] E. B. Flagg, A. Muller, J. W. Robertson, S. Founta, D. G. Deppe, M. Xiao, W. Ma, G. J. Salamo, and C. K. Shih, "Resonantly driven coherent oscillations in a solid-state quantum emitter," *Nat Phys*, vol. 5, pp. 203–207, Mar. 2009.

[106] J. Dreiser, M. Atatüre, C. Galland, T. Müller, A. Badolato, and A. Imamoglu, "Optical investigations of quantum dot spin dynamics as a function of external electric and magnetic fields," *Phys. Rev. B*, vol. 77, p. 075317, Feb 2008.

[107] C. W. Lai, P. Maletinsky, A. Badolato, and A. Imamoglu, "Knight-field-enabled nuclear spin polarization in single quantum dots," *Phys. Rev. Lett.*, vol. 96, p. 167403, Apr 2006.

[108] E. A. Chekhovich, M. N. Makhonin, K. V. Kavokin, A. B. Krysa, M. S. Skolnick, and A. I. Tartakovskii, "Pumping of nuclear spins by optical excitation of spin-forbidden transitions in a quantum dot," *Phys. Rev. Lett.*, vol. 104, p. 066804, Feb 2010.

[109] K. M. Weiss, J. M. Elzerman, Y. L. Delley, J. Miguel-Sanchez, and A. Imamoğlu, "Coherent two-electron spin qubits in an optically active pair of coupled InGaAs quantum dots," *Phys. Rev. Lett.*, vol. 109, p. 107401, Sep 2012.

[110] H. Bluhm, S. Foletti, I. Neder, M. Rudner, D. Mahalu, V. Umansky, and A. Yacoby, "Dephasing time of GaAs electron-spin qubits coupled to a nuclear bath exceeding 200μs," *Nat Phys*, vol. 7, pp. 109–113, Feb. 2011.

[111] X. Xu, W. Yao, B. Sun, D. G. Steel, A. S. Bracker, D. Gammon, and L. J. Sham, "Optically controlled locking of the nuclear field via coherent dark-state spectroscopy," *Nature*, vol. 459, pp. 1105–1109, June 2009.

[112] G. de Lange, T. van der Sar, M. Blok, Z.-H. Wang, V. Dobrovitski, and R. Hanson, "Controlling the quantum dynamics of a mesoscopic spin bath in diamond," *Sci. Rep.*, vol. 2, p. 382, Apr. 2012.

[113] H. S. Knowles, D. M. Kara, and M. Atatüre, "Observing bulk diamond spin coherence in high-purity nanodiamonds," *Nat Mater*, vol. 13, pp. 21–25, Jan. 2014.

[114] M. B. Plenio, S. F. Huelga, A. Beige, and P. L. Knight, "Cavity-loss-induced generation of entangled atoms," *Phys. Rev. A*, vol. 59, pp. 2468–2475, Mar 1999.

[115] S. Diehl, A. Micheli, A. Kantian, B. Kraus, H. P. Buchler, and P. Zoller, "Quantum states and phases in driven open quantum systems with cold atoms," *Nat Phys*, vol. 4, pp. 878–883, Nov. 2008.

[116] F. Verstraete, M. M. Wolf, and J. Ignacio Cirac, "Quantum computation and quantum-state engineering driven by dissipation," *Nat Phys*, vol. 5, pp. 633–636, Sept. 2009.

[117] Y. Lin, J. P. Gaebler, F. Reiter, T. R. Tan, R. Bowler, A. S. Sorensen, D. Leibfried, and D. J. Wineland, "Dissipative production of a maximally entangled steady state of two quantum bits," *Nature*, vol. 504, pp. 415–418, Dec. 2013.

[118] S. Bose, "Quantum communication through an unmodulated spin chain," *Phys. Rev. Lett.*, vol. 91, p. 207901, Nov 2003.

[119] T. Fogarty, E. Kajari, B. G. Taketani, A. Wolf, T. Busch, and G. Morigi, "Entangling two defects via a surrounding crystal," *Phys. Rev. A*, vol. 87, p. 050304, May 2013.

[120] H. R. Gray, R. M. Whitley, and C. R. Stroud, "Coherent trapping of atomic populations," *Opt. Lett.*, vol. 3, pp. 218–220, Dec 1978.

[121] H. Kamada, H. Gotoh, J. Temmyo, T. Takagahara, and H. Ando, "Exciton Rabi oscillation in a single quantum dot," *Phys. Rev. Lett.*, vol. 87, p. 246401, Nov 2001.

[122] X. Xu, B. Sun, P. R. Berman, D. G. Steel, A. S. Bracker, D. Gammon, and L. J. Sham, "Coherent optical spectroscopy of a strongly driven quantum dot," *Science*, vol. 317, no. 5840, pp. 929–932, 2007.

[123] C. G. Yale, B. B. Buckley, D. J. Christle, G. Burkard, F. J. Heremans, L. C. Bassett, and D. D. Awschalom, "All-optical control of a solid-state spin using coherent dark states," *Proceedings of the National Academy of Sciences of the United States of America*, vol. 110, pp. 7595–7600, Apr. 2013.

[124] B. Pingault, J. N. Becker, H. Schulte, Carsten H. C. Arend, C. Hepp, T. Godde, A. I. Tartakovskii, M. Markham, C. Becher, and M. Atatüre, "All-optical formation of coherent dark states of silicon-vacancy spins in diamond," *Phys. Rev. Lett.*, vol. 113, p. 263601, Dec 2014.

[125] K.-M. C. Fu, C. Santori, C. Stanley, M. C. Holland, and Y. Yamamoto, "Coherent population trapping of electron spins in a high-purity *n*-type GaAs semiconductor," *Phys. Rev. Lett.*, vol. 95, p. 187405, Oct 2005.

[126] C. Santori, P. Tamarat, P. Neumann, J. Wrachtrup, D. Fattal, R. G. Beausoleil, J. Rabeau, P. Olivero, A. D. Greentree, S. Prawer, F. Jelezko, and P. Hemmer, "Coherent population trapping of single spins in diamond under optical excitation," *Phys. Rev. Lett.*, vol. 97, p. 247401, Dec 2006.

[127] K. Bergmann, H. Theuer, and B. W. Shore, "Coherent population transfer among quantum states of atoms and molecules," *Rev. Mod. Phys.*, vol. 70, pp. 1003–1025, Jul 1998.

[128] E. Peter, P. Senellart, D. Martrou, A. Lemaître, J. Hours, J. M. Gérard, and J. Bloch, "Exciton-photon strong-coupling regime for a single quantum dot embedded in a microcavity," *Phys. Rev. Lett.*, vol. 95, p. 067401, Aug 2005.

[129] K. Srinivasan and O. Painter, "Linear and nonlinear optical spectroscopy of a strongly coupled microdisk-quantum dot system," *Nature*, vol. 450, pp. 862–865, Dec. 2007.

[130] A. K. Nowak, S. L. Portalupi, V. Giesz, O. Gazzano, C. Dal Savio, P.-F. Braun, K. Karrai, C. Arnold, L. Lanco, I. Sagnes, A. Lemaître, and P. Senellart, "Deterministic and electrically tunable bright single-photon source," *Nat Commun*, vol. 5, p. 3240, Feb. 2014.

[131] F. Marsili, V. B. Verma, J. A. Stern, S. Harrington, A. E. Lita, T. Gerrits, I. Vayshenker, B. Baek, M. D. Shaw, R. P. Mirin, and S. W. Nam, "Detecting single infrared photons with 93 % system efficiency," *Nat Photon*, vol. 7, pp. 210–214, Mar. 2013.

[132] N. H. Lindner and T. Rudolph, "Proposal for pulsed on-demand sources of photonic cluster state strings," *Phys. Rev. Lett.*, vol. 103, p. 113602, Sep 2009.

[133] R. Raussendorf and H. J. Briegel, "A one-way quantum computer," *Phys. Rev. Lett.*, vol. 86, pp. 5188–5191, May 2001.

[134] R. Prevedel, P. Walther, F. Tiefenbacher, P. Bohi, R. Kaltenbaek, T. Jennewein, and A. Zeilinger, "High-speed linear optics quantum computing using active feed-forward," *Nature*, vol. 445, pp. 65–69, Jan. 2007.

[135] J. Berezovsky, M. H. Mikkelsen, N. G. Stoltz, L. A. Coldren, and D. D. Awschalom, "Picosecond coherent optical manipulation of a single electron spin in a quantum dot," *Science*, vol. 320, no. 5874, pp. 349–352, 2008.